# Master thesis and internship[BR]- Master's thesis : Comparison of steady and unsteady viscous-inviscid coupling strategies in BLASTER[BR]- Internship

**Auteur :** Thomée, Corentin
**Promoteur(s) :** Terrapon, Vincent
**Faculté :** Faculté des Sciences appliquées
**Diplôme :** Master en ingénieur civil en aérospatiale, à finalité spécialisée en "aerospace engineering"
**Année académique :** 2023-2024
**URI/URL :** http://hdl.handle.net/2268.2/20440

Université de Liège - Faculté des Sciences Appliquées

# Comparison of steady and unsteady viscous-inviscid coupling strategies in BLASTER

Travail de fin d'études réalisé en vue de l'obtention du grade de master
"Ingénieur Civil en Aérospatiale" par

Corentin Thomée

Promoteur: Prof. Vincent E. Terrapon

Année académique 2023-2024

# Abstract

Modern aircraft design relies on the usage of computational fluid dynamics for the prediction of aerodynamic performance. High fidelity methods such as the Reynolds-Averaged Navier-Stokes (RANS) equations are too computationally expensive for early design stages such that a simpler method known as viscous-inviscid interaction can be used instead. The inviscid flow is calculated and is corrected by the viscous flow in the boundary layer. The coupling between the two regions is complex and prone to numerical issues.

The present work aims to compare steady and unsteady coupling strategies to solve for steady-state problems within the BLASTER solver. The existing inviscid solver is replaced by an incompressible panel method in its steady and unsteady forms. The viscous solver is also adapted to allow for unsteady simulations; the pseudo time marching algorithm and transition treatment in BLASTER are modified accordingly. The missing elements for a complete unsteady model are identified and discussed.

The steady and unsteady coupling strategies are compared based on speed, accuracy and stability for different test cases in various flow regimes of interest. The unsteady coupling shows better stability and faster convergence especially for high incidence flows with separation. This advantage is diminished as the incidence decreases and the flow becomes simpler. For all cases, both strategies yield similar results with little to no difference. The low-Reynolds number flow proves to be challenging for the solver, and its divergence is not resolved by the unsteady coupling strategy.

The method is also tested on true unsteady pitching cases. Understanding the limitations of the model, simple conditions can be predicted with good accuracy compared to RANS simulations. Nonetheless, the solver lacks the ability to predict fast motion, and suffers from issues when refining the time step.

# Acknowledgements

I would first like to thank my advisor, Prof. Vincent Terrapon, for his guidance and support throughout this project. He really made me feel like I was part of the team and not just a student. The feedback he provided was invaluable and helped me to improve my work.

I would like to thank my supervisor, Paul Dechamps for his help and interest in my thesis. He was always available to sit down and discuss the project, and his feedback was always constructive. His extensive knowledge of the subject was a great asset, especially when I stumbled into difficulties that he had already encountered in the past.

Finally, I would like to thank my friends and especially my family for their support and encouragement throughout my studies. I could not have made it this far without them.

# Nomenclature

### Abbreviations

| | |
|---|---|
| CFL | Courant–Friedrichs–Lewy number |
| $\mathcal{S}$ | Steady coupling strategy |
| $\mathcal{U}$ | Unsteady coupling strategy |
| HSPM | Hess and Smith panel method |
| UPM | Unsteady panel method |
| RANS | Reynolds-averaged Navier-Stokes |
| VII | Viscous-inviscid interaction |

### Subscripts

| | |
|---|---|
| $\cdot_\infty$ | Quantity in the freestream |
| $\cdot_e$ | Inviscid quantity |

### Symbols

| | |
|---|---|
| $\alpha$ | Freestream angle of attack |
| $\alpha_a$ | Pitching motion amplitude |
| $\alpha_m$ | Pitching motion mean angle of attack |
| $\beta_{i,j}$ | Angle formed by points of panel j and midpoint of panel i |
| $\Delta\tau$ | Inner time step in the time integration |
| $\Delta t$ | Time step |
| $\Delta \boldsymbol{U}$ | Solution increment for time integration |
| $\Delta$ | Shed vortex panel length |
| $\delta$ | Boundary layer thickness |
| $\delta^*$ | Displacement thickness |
| $\delta^{**}$ | Density thickness |
| $\delta^R$ | Second density thickness |
| $\boldsymbol{\varepsilon}$ | Small perturbation |
| $\gamma$ | Vortex strength |

| | |
|---|---|
| $\Gamma$ | Circulation |
| $\gamma_a$ | Ratio of specific heats |
| $\mu$ | Dynamic viscosity |
| $\nu$ | Fluid kinematic viscosity |
| $\omega$ | Pitching motion angular frequency |
| $\Omega$ | Airfoil pitching angular velocity |
| $\omega_r$ | Rotational |
| $\Phi$ | Wagner's function |
| $\phi$ | Potential function |
| $\psi$ | Airfoil pitching accumulated angle |
| $\rho$ | Fluid density |
| $\sigma$ | Source strength |
| $\boldsymbol{\sigma_k}^u$ | Solution vector for the UPM method |
| $\boldsymbol{\tau}$ | Viscous shear stress |
| $\tau_w$ | Wall shear stress |
| $\theta$ | Momentum thickness |
| $\theta^*$ | Kinetic energy thickness |
| $\theta_i$ | Angle of panel i |
| $\Theta$ | Shed vortex panel angle |
| $\xi, \eta$ | Coordinates in the boundary layer system |
| $\boldsymbol{A}$ | Time derivative factors for time integration |
| $a$ | Advection velocity |
| $(A, B, C)^{n/t/x/y}$ | HSPM or UPM influence coefficients |
| $\boldsymbol{A}^n$ | Matrix of normal panel influence coefficients |
| $\boldsymbol{A}^s$ | Matrix to inverse for the HSPM method |
| $A_s$ | Detached flow transition correction term |
| $\boldsymbol{B}$ | Space derivative factors for time integration |

| | |
|---|---|
| $b$ | Half-chord of the airfoil |
| $\boldsymbol{b}^s$ | Right-hand side vector for the HSPM method |
| $\boldsymbol{b}^u$ | Vortex contribution to the right-hand side vector for the UPM method |
| $\boldsymbol{C}$ | Free terms for time integration |
| $c$ | Chord of the airfoil |
| $C(k)$ | Theodorsen's function |
| $\boldsymbol{c}^u$ | Free contribution to the right-hand side vector for the UPM method |
| $C_\tau$ | Shear stress coefficient |
| $C_{\tau_{EQ}}$ | Equilibrium shear stress coefficient |
| $c_d$ | Drag coefficient |
| $c_f$ | Skin friction coefficient |
| $C_p$ | Pressure coefficient |
| $c_s$ | Speed of sound |
| $c_{d,f}$ | Friction drag coefficient |
| $c_{d,p}$ | Pressure drag coefficient |
| $c_{ds}$ | Dissipation coefficient |
| $E$ | Energy |
| $\boldsymbol{e}_x, \boldsymbol{e}_y$ | Unit vectors in the x and y directions |
| $\boldsymbol{F}$ | Spatial operator for time integration |
| $\boldsymbol{f}$ | Fluid body forces |
| $H$ | Boundary layer shape factor |
| $h$ | Cell size |
| $H^*$ | Kinetic energy shape parameter |
| $H^{**}$ | Density shape parameter |
| $H_k$ | Kinematic shape parameter |
| $k$ | Pitching motion reduced frequency |
| $l$ | Perimeter of the airfoil |

| | |
|---|---|
| $L_{pot}$ | Distance from leading edge for potential integration |
| $M$ | Mach number |
| $\tilde{N}$ | Amplification ratio of the Tollmien-Schlichting waves |
| $N$ | Number of panels |
| $N_{pot}$ | Number of elements along the potential integration path |
| $\boldsymbol{q}$ | Heat flux |
| $\|\|\boldsymbol{R}\|\|$ | Residual |
| $R_d$ | Wake correction dissipation ratio |
| $r_p, \theta_p$ | Polar coordinates |
| Re | Reynolds number |
| $\boldsymbol{s_1}^u$ | Vortex contribution to the solution vector for the UPM method |
| $\boldsymbol{s_2}^u$ | Free contribution to the solution vector for the UPM method |
| $t$ | Time |
| $\boldsymbol{t}_i, \boldsymbol{n}_i$ | Normal and tangential vectors to panel i |
| $T_u$ | Turbulence intensity |
| $\boldsymbol{U}$ | Vector of unknown for time integration |
| $\boldsymbol{u} = \big(u, v\big)$ | Fluid velocity |
| $U_p, V_p$ | Airfoil pitching velocity components |
| $U_s$ | Equivalent normalized wall slip velocity |
| $V^t, V^n$ | Normal and tangential velocity components to a panel |
| $V^{bl}$ | Blowing velocity |
| $\boldsymbol{V}_{\text{stream}}$ | Effective freestream velocity on a moving airfoil |
| $x, y$ | Cartesian coordinates |
| $\boldsymbol{x}^s$ | Vector of unknowns for the HSPM method |
| $x_f$ | Pivot point for airfoil pitching |
| $x_{tr}$ | Turbulent transition location |

# List of Figures

# List of Tables

# Contents

# 1 Introduction

## 1.1 Context

In aircraft design, there is a constant search for efficiency gains. Modern methods rely on optimization techniques which require many evaluations of the performance of different geometries. It is thus essential to have access to fast and reliable means to estimate performance. The Reynolds-Averaged Navier-Stokes (RANS) equations, although orders of magnitude cheaper than the complete Navier-Stokes equations, remain too expensive for early design stages.

A method known as viscous-inviscid interaction (VII) can considerably simplify this problem. An observation made by Prandtl [44] allows the division of the full flow into two regions. He noticed that viscous effects only matter in a thin region around a body called the boundary layer. Outside this region, viscosity can be neglected, and the flow behaves as if it were inviscid. This is illustrated in Figure 1.1.

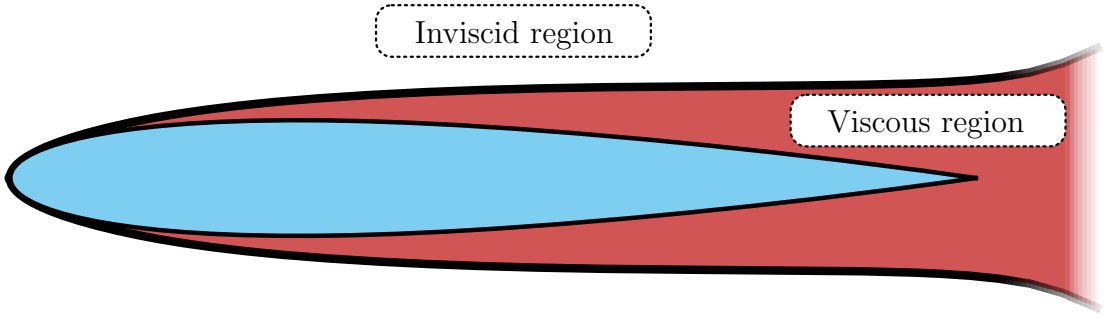


Figure 1.1: Inviscid and viscous regions around an airfoil (the boundary layer is exaggerated for visibility).

The inviscid and viscous regions each have their own physics and equations and are brought together through a coupling method. This coupling is a complex topic and can lead to numerical issues, most notably the Goldstein singularity at separation [26]. The present work aims to provide a comparison between a steady and an unsteady coupling methods for the solution of steady-state VII problems within the BLASTER [18] software.

Depending on the sought accuracy level and available computational resources, different inviscid and viscous models can be considered for VII.

The most accurate and costly inviscid solver is the Euler equations, which only assume the lack of viscosity. They have been used in the VII context by Drela [20], Whitfield *et al.* [63] or Moro *et al.* [39] for instance. Further assuming irrotationality results in the full-potential equation, providing a good balance between accuracy and cost, allowing for transonic computations at a lower cost than the Euler equations. This approach was chosen by Dechamps in BLASTER [18], as well as by the commercial software TRANAIR [31, 5]. For incompressible flows, Laplace's equation can be solved, typically with cheap panel methods; this was done by Drela in XFOIL [21] and in many other work [25, 43, 47, 12, 45].

The viscous region is typically solved using an integral boundary layer method where the flow is integrated along the normal direction to the body to reduce the number of space dimensions by one.

This model is completed by the closure relations of Nishida and Drela [42]. The method can be used in a steady [21, 46, 62, 63] or an unsteady [67, 47, 43, 25, 18] manner depending on the application.

The VII coupling can be done through a variety of methods, depending on the assumed hierarchy between the inviscid and viscous regions. The simplest method is the *direct* coupling, where the two regions are solved separately and exchange information at each iteration. This method suffers from the Goldstein [26] singularity at separation, which is problematic. The *inverse* coupling method [9] allows getting rid of the Goldstein singularity by inverting the problem. It however requires adaptations in the solvers to handle the new boundary conditions, and exhibits slow convergence. The *fully-simultaneous* coupling method [20, 23] solves the inviscid and viscous regions together. This method is robust, but is complex to implement and computationally expensive. The *quasi-simultaneous* coupling method [58] solves the regions separately, but provides an estimation of the inviscid region inside the viscous solver through an interaction law. This method allows for good convergence while being versatile. It is the method used in BLASTER; as it does not require special modifications inside the inviscid solver, it makes it simple to integrate existing solvers in the VII framework.

When using the quasi-simultaneous method for steady-state problems, both the inviscid and viscous solvers are often run to their steady solutions before communicating. Recently, an unsteady method was described by Ozdemir *et al.* [43]. Instead of reaching a steady solution at each iteration, the solvers only run for a single time step. This method was not directly compared to the classical steady method; the present work aims to fill this gap based on various test cases. The steady and unsteady methods are schematized in Figure 1.2.

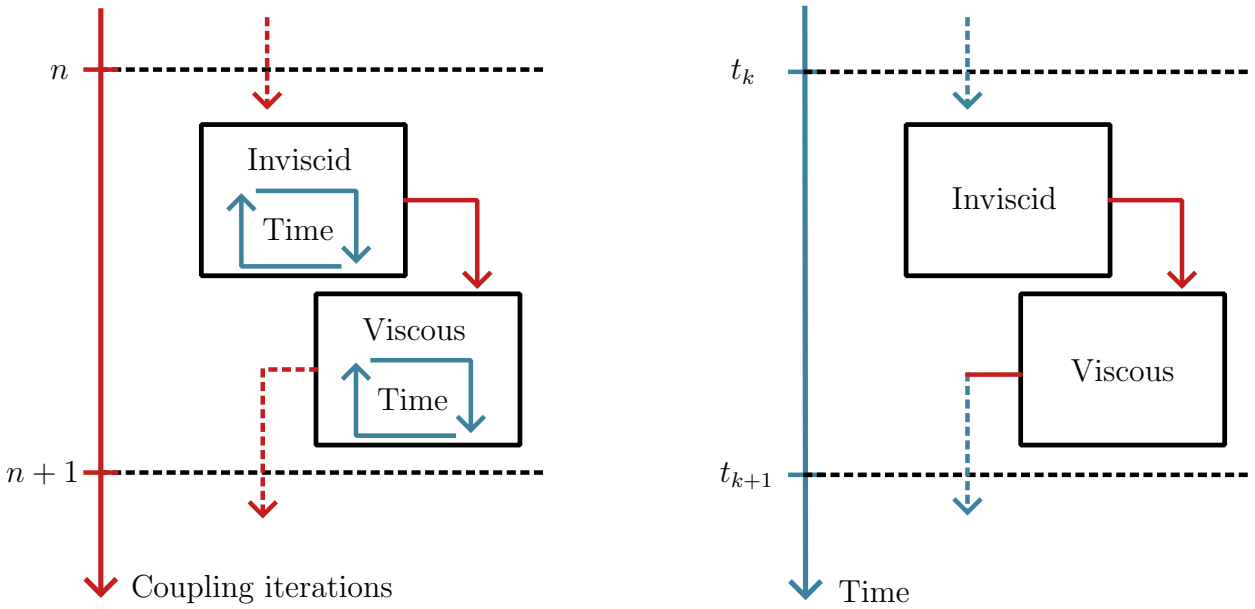


Figure 1.2: Representation of the "steady" (left) and "unsteady" (right) VII coupling strategies.

The implementation and comparison of the two coupling methods are done within the BLASTER software developed at the University of Liège by Dechamps [18], as an extension of the work of Bilocq [6]. This software couples the full-potential solver DARTFLO [16] with an integral boundary layer solver through quasi-simultaneous coupling. Dechamps solved the viscous region to its steady

solution through a pseudo-time marching loop, improving stability compared to a purely steady approach.

The objective of the present work being the comparison of coupling strategies rather than the modeling of complex flows, the physics of the problem is simplified as much as possible. The flow is considered two-dimensional and incompressible. The inviscid region also assumes irrotational flow, allowing the use of a cheap panel method. The steady version of this method by Hess and Smith [30] (HSPM) and its unsteady version by Basu and Hancock [4] (UPM) are implemented in the present work and integrated within BLASTER. These allow for the fast solution of the inviscid region in the steady and unsteady cases respectively.

In order to implement the unsteady coupling method, the existing viscous solver in BLASTER requires a few adaptations. The time marching loop is modified to perform a single time step, and the laminar to turbulent transition handling is changed.

The comparison is done on a variety of test cases. The behavior of the steady and unsteady methods is analyzed based on stability, speed and accuracy in different flow conditions including attached and mildly separated flows.

Additionally, the implementation of the unsteady panel method and the unsteady interaction method allows for the first steps towards a true unsteady VII model. This topic was already studied by various authors [25, 55, 47, 29, 67, 14]; the present work mainly highlights the missing elements in the current model for unsteady flows and presents possible improvements. The closure model, interaction law and transition handling are discussed in this context. A few unsteady test cases present the current capabilities and limitations of the model.

This report first presents the theory and implementation behind the HSPM and UPM methods used to solve the inviscid region in section 2. The viscous region is then covered in section 3, with reminders of the equations and numerics behind the BLASTER code. The modifications made to the code to allow for unsteady interaction are also detailed. The topic of VII is discussed in section 4, with the presentation of the different interaction methods and the specificities of unsteady interaction. Finally, section 5 presents various inviscid and viscous test cases. The inviscid cases are used to validate the HSPM and UPM methods. The steady viscous cases allow the comparison of the steady and unsteady interaction methods in a variety of flow conditions. Unsteady viscous cases are also presented as an extension of the model.

## 1.2 Main contributions of the present work

- Implementation of the Hess and Smith (HSPM) and unsteady (UPM) panel methods to solve the inviscid region.
- Adaptation of the time marching algorithm to allow for unsteady interaction. Modification of the time loop to perform a single time step, and changes in the turbulent transition handling.
- Comparison of the steady and unsteady interaction methods on various test cases, based on stability, speed and accuracy.

- Investigation of the possibility of solving unsteady flows with the viscous-inviscid interaction method. Identification of the shortcomings of the present method and proposition of improvements.

# 2 Inviscid region

For any flow, the Navier-Stokes equations are written

$$\text{Continuity:} \quad \frac{\partial \rho}{\partial t} + \nabla \cdot (\rho \boldsymbol{u}) = 0. \tag{2.1a}$$

$$\text{Momentum:} \quad \frac{\partial}{\partial t}(\rho \boldsymbol{u}) + \nabla \cdot (\rho \boldsymbol{u}\boldsymbol{u}) = -\nabla p + \rho \boldsymbol{f} + \nabla \cdot \boldsymbol{\tau}. \tag{2.1b}$$

$$\text{Energy:} \quad \frac{\partial}{\partial t}(\rho E) + \nabla \cdot (\rho E \boldsymbol{u}) = \rho \boldsymbol{f} \cdot \boldsymbol{u} + \nabla \cdot (\boldsymbol{u} \cdot \boldsymbol{\tau}) - \nabla \cdot \boldsymbol{q}, \tag{2.1c}$$

where $\rho$ is the density, $\boldsymbol{u} = (u, v, w)$ the velocity, $\boldsymbol{f}$ are the body forces, $E$ is the energy, $\boldsymbol{q}$ is the heat flux and $\boldsymbol{\tau}$ is the shear stress. For a Newtonian fluid such as air or water, the shear stress can be written as

$$\boldsymbol{\tau} = \mu \left[ \left( \nabla \boldsymbol{u} + \nabla \boldsymbol{u}^T \right) - \frac{2}{3} (\nabla \cdot \boldsymbol{u}) \boldsymbol{I} \right], \tag{2.2}$$

where $\mu$ is the dynamic viscosity of the fluid.

The first assumptions about the flow, made for both viscous and inviscid regions, are two-dimensionality and lack of heat transfer. For inviscid flows, the viscosity $\mu$ vanishes. As mentioned before, the present work additionally assumes the flow to be incompressible and irrotational. This allows the derivation of Laplace's equation, which is linear and thus allows for the superposition of elementary solutions; a property that is exploited to build inexpensive panel methods. Compared to the full Euler equations, this approach leads to less accurate solutions but comes at a much lower computational cost.

This section first goes into the derivation of the governing equations for the inviscid region. The panel methods implemented in the present work are then presented in detail, starting with the steady case (HSPM), followed by its unsteady extension (UPM). Alternatives to these methods are also discussed.

## 2.1 Theory

### 2.1.1 Laplace's equation

Under the incompressibility assumption *i.e.* $\rho = \text{cst}$, the continuity part of the Navier-Stokes equations (2.1a) simplifies to

$$\nabla \cdot \boldsymbol{u} = 0. \tag{2.3}$$

Furthermore, for irrotational flows, the potential function $\phi$ may be introduced such that

$$\boldsymbol{u} = \nabla \phi. \tag{2.4}$$

Indeed, irrotational flows are characterized by a rotational $\boldsymbol{\omega_r} = \nabla \times \boldsymbol{u} = 0$, which is satisfied by expressing the velocity field as the gradient of a scalar function.
Substituting $\boldsymbol{u}$ from (2.4) into (2.3) yields ***Laplace's equation***

$$\nabla^2 \phi = 0. \tag{2.5}$$

Due to its linearity, Laplace's equation allows for the superposition of elementary solutions. In this work, three of these solutions are used as building blocks to characterize the flow over an airfoil:

- The freestream of velocity $V_\infty$ at an angle $\alpha$: $\phi(x, y) = V_\infty (x \cos\alpha + y \sin\alpha)$,
- The source of strength $\sigma$: $\phi(r_p, \theta_p) = \dfrac{\sigma}{2\pi} \ln r_p$,
- The vortex of strength $\gamma$: $\phi(r_p, \theta_p) = \dfrac{\gamma}{2\pi} \theta_p$,

where $(x, y)$ are Cartesian coordinates and $(r_p, \theta_p)$ are polar coordinates from the center of the source or vortex. More details on these solutions can be found in Anderson [2].

These elementary solutions are schematically represented in Figure 2.1.

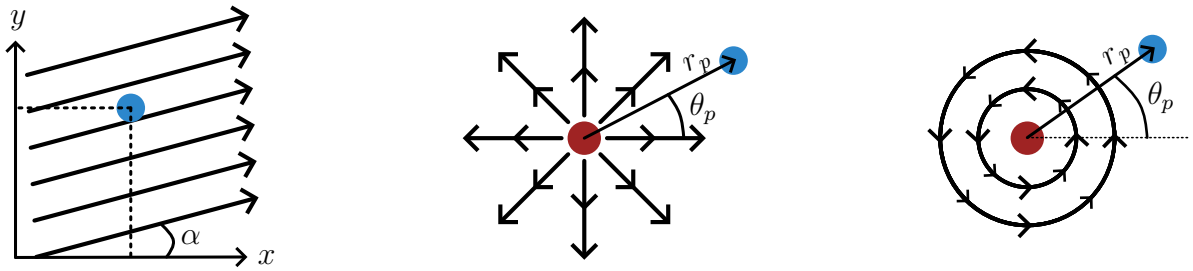


(a) Freestream. (b) Source. (c) Vortex.

Figure 2.1: Elementary solutions of Laplace's equation.

### 2.1.2 Kutta condition

One major limitation of Laplace's equation for potential flow is that it admits an infinity of solutions. For the flow around a body, these solutions differ by the amount of circulation of the body, or in other words its lift. This is rather inconvenient for aerodynamic purposes. Fortunately, the Kutta [34] condition has been formulated to alleviate this issue. For sharp airfoils, it states that the physical solution requires the flow to leave smoothly at the trailing edge.

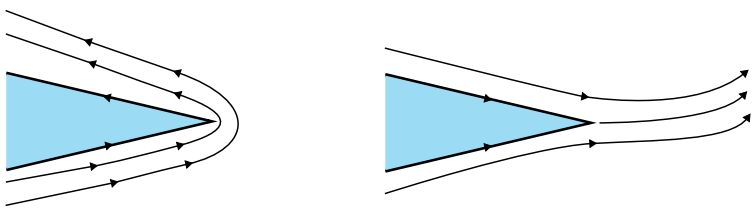

Figure 2.2: Nonphysical (left) and physical (right) solutions to Laplace's equation.

Concretely, this condition comes down to imposing equal pressures on the upper and lower side of the trailing edge.

It should be noted that despite the application of the Kutta condition, the potential flow inherently lacks the ability to predict pressure drag, which is a consequence of viscous effects; this is known as the d'Alembert [17] paradox.

### 2.1.3 Bernoulli's equation

While the combination of Laplace's equation and Kutta condition is sufficient to describe the velocity field around an airfoil, the momentum equation is still essential. Indeed, it allows to determine the pressure distribution around the body, gathering information about the aerodynamic coefficients.

Under the assumptions of inviscid flow, irrotationality and incompressibility, the momentum equation (2.1b) simplifies to

$$\nabla\left(\rho\frac{\partial\phi}{\partial t}\right)+\nabla\left(\rho\frac{||\boldsymbol{u}||^2}{2}\right)+\nabla p=0. \tag{2.6}$$

Integrating this result gives birth to **Bernoulli's equation**

$$\frac{\partial\phi}{\partial t}+\frac{||\boldsymbol{u}||^2}{2}+\frac{p}{\rho}=C(t), \tag{2.7}$$

where $C(t)$ is a time-varying constant. More details on the derivation of Bernoulli's equation can be found in Anderson [2].

Evaluating equation (2.7) both at some location $s$ and in the freestream, one obtains the following expression for the pressure coefficient

$$C_{p,s}\equiv\frac{p_s-p_\infty}{\frac{1}{2}\rho V_\infty^2}=1-\frac{||\boldsymbol{u_s}||^2}{V_\infty^2}+\frac{2}{V_\infty^2}\left(\frac{\partial\phi_\infty}{\partial t}-\frac{\partial\phi_s}{\partial t}\right). \tag{2.8}$$

## 2.2 Implementation

Laplace's equation can be solved with different methods of varying accuracy levels and computational costs. The panel method used in this work has the advantage of having a relatively low cost as well as ease of creating a mesh. The steady form of this method (HSPM) and its unsteady extension (UPM) both have been implemented.

### 2.2.1 Steady form (HSPM)

This method was developed by Hess and Smith [30]. Their method needed to be simple due to low available computational power. This makes it a great candidate for the present VII algorithm,

where the inviscid solver may be called many times.

The airfoil is first discretized by a series of $N+1$ points $(x_i, y_i)$ in a closed loop. These points, or nodes, are numbered following the *Selig* order. This means that the numbering starts at the trailing edge, to the leading edge through the upper side, then back to the trailing edge through the lower side. $N$ straight panels are formed between adjacent nodes. For each panel, calculations are done on its *control point* $(x_{m,i}, y_{m,i})$, corresponding to its midpoint. The airfoil discretization is shown in Figure 2.3, where circles represent nodes, and crosses are control points.

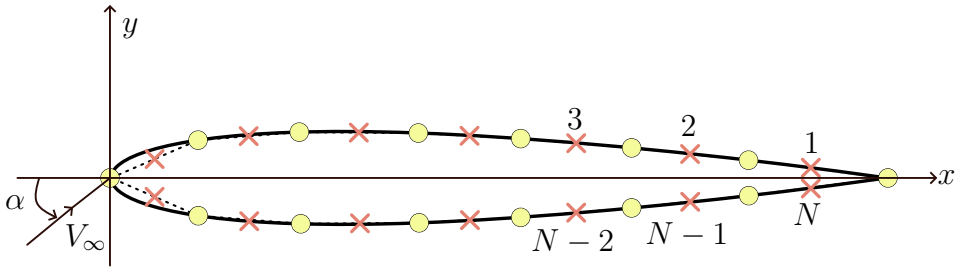


Figure 2.3: Representation of the airfoil panels for the HSPM method. Circles are nodes and crosses are control points. The three first and last elements numbers are displayed. The freestream velocity $V_\infty$ at an angle $\alpha$ is also shown. Adapted from [12].

For each panel, constant source and vortex strengths are imposed to describe the flow. While each panel possesses its own source strength $\sigma_i$, the vortex strength $\gamma$ is shared for all panels, resulting in a total of $N+1$ unknowns to determine.
$N$ equations are obtained from the boundary conditions on the airfoil surface. When the inviscid solver runs alone, these are the non-penetration conditions on the surface. The final equation to close the system is the Kutta condition at the trailing edge.

The induced speed on any panel $i$ by panel $j$ can be expressed using the *influence coefficients* $A^n_{ij}$, $A^t_{ij}$, $B^n_{ij}$ and $B^t_{ij}$, corresponding to the normal $(^n)$ and tangential $(^t)$ contributions of the source $(A)$ and vortex $(B)$ singularities of unit strength. These coefficients are written as [52]

$$
\begin{aligned}
A^n_{i,j} &= \begin{cases} \dfrac{1}{2\pi}\left[\sin(\theta_i-\theta_j)\ln\dfrac{r_{i,j}}{r_{i,j+1}} + \cos(\theta_i-\theta_j)\,\beta_{i,j}\right] & i \neq j, \\ \dfrac{1}{2} & i = j, \end{cases} \\
A^t_{i,j} &= \begin{cases} \dfrac{1}{2\pi}\left[\sin(\theta_i-\theta_j)\,\beta_{i,j} - \cos(\theta_i-\theta_j)\ln\dfrac{r_{i,j}}{r_{i,j+1}}\right] & i \neq j, \\ 0 & i = j, \end{cases} \\
B^n_{i,j} &= -A^t_{i,j}, \\
B^t_{i,j} &= A^n_{i,j},
\end{aligned}
\tag{2.9}
$$

where $\theta_i$ is the angle of panel $i$, $r_{i,j}$ is the distance between nodes $i$ and $j$, and $\beta_{i,j}$ is the angle formed between node $j$, the midpoint of panel $i$, and node $j+1$. This is shown schematically in Figure 2.4.

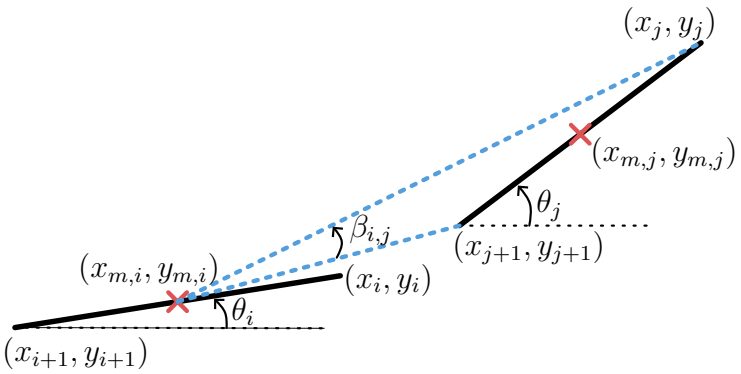


Figure 2.4: Representation of the angles between two panels for the HSPM method. $\theta_i$ and $\theta_j$ are the angles from the horizontal of panels $i$ and $j$, and $\beta_{i,j}$ is the angle formed between node $j$, the midpoint of panel $i$, and node $j+1$.

With these influence coefficients, the tangential and normal components of velocity on the $i^{\text{th}}$ panel can be written as the sum of freestream, sources and vortices as

$$\begin{aligned} V_i^t &= V_\infty \cos(\alpha - \theta_i) + \sum_{j=1}^{N} \sigma_j A_{i,j}^t + \gamma \sum_{j=1}^{N} B_{i,j}^t, \\ V_i^n &= V_\infty \sin(\alpha - \theta_i) + \sum_{j=1}^{N} \sigma_j A_{i,j}^n + \gamma \sum_{j=1}^{N} B_{i,j}^n. \end{aligned} \tag{2.10}$$

The non-penetration boundary condition is valid for any panel, such that

$$V_\infty \sin(\alpha - \theta_i) + \sum_{j=1}^{N} \sigma_j A_{i,j}^n + \gamma \sum_{j=1}^{N} B_{i,j}^n = 0 \qquad \forall i \in [1, N]. \tag{2.11}$$

In this method, the Kutta condition comes to imposing the equality of the velocity magnitudes on the upper and lower side of the trailing edge *i.e.* panels 1 and $N$. Since these are oriented in the opposite direction, this condition can be written as

$$\begin{aligned} V_1^t \equiv V_\infty \cos(\alpha - \theta_1) + \sum_{j=1}^{N} \sigma_j A_{1,j}^t + \gamma \sum_{j=1}^{N} B_{1,j}^t \\ = \\ -V_\infty \cos(\alpha - \theta_N) - \sum_{j=1}^{N} \sigma_j A_{N,j}^t - \gamma \sum_{j=1}^{N} B_{N,j}^t \equiv -V_N^t \end{aligned} \tag{2.12}$$

The system of equations (2.11) and (2.12) is solved by writing it in the form [12]

$$\boldsymbol{A}^s \boldsymbol{x}^s = \boldsymbol{b}^s, \tag{2.13}$$

where

$$
\begin{aligned}
\boldsymbol{x}^s &= \begin{pmatrix} \boldsymbol{\sigma} & \gamma \end{pmatrix} \\
A^s_{i,j} &= A^n_{i,j} && i,j \in 1,\dots,N \\
A^s_{i,N+1} &= \sum_{j=1}^{N} B^N_{i,j} && i \in 1,\dots,N \\
A^s_{N+1,j} &= A^t_{1,j} + A^t_{N,j} && j \in 1,\dots,N \\
A^s_{N+1,N+1} &= \sum_{j=1}^{N} \left(B^t_{1,j} + B^t_{N,j}\right) \\
b^s_i &= -V_\infty \sin\left(\alpha - \theta_i\right) && i \in 1,\dots,N \\
b^s_{N+1} &= -V_\infty \cos\left(\alpha - \theta_1\right) - V_\infty \cos\left(\alpha - \theta_N\right).
\end{aligned}
\tag{2.14}
$$

Equation (2.13) is solved for $\boldsymbol{\sigma}$ and $\gamma$ by using the LU decomposition of the $\boldsymbol{A}^s$ matrix. Knowing the solutions for $\sigma_i$ and $\gamma$, tangential velocities $V^t_i$ can be obtained from equation (2.10) to compute the pressure coefficients. In steady flow, Bernoulli's equation (2.8) simplifies to

$$
C_{p,i} = 1 - \left(\frac{V_i}{V_\infty}\right)^2. \tag{2.15}
$$

The aerodynamic coefficients are then simply obtained by integrating $C_p$ on the panels.

### 2.2.2 Unsteady form (UPM)

In order to be able to model unsteady flow features, Basu and Hancock [4] developed an extension of the Hess and Smith panel method, based on the conservation of circulation. The present work implements this method closely following Teng [52], with some slight modifications by Young [68].

Due to the fact that this method allows movements of the airfoil, a local coordinate system $(x, y)$ has to be defined. It is fixed on the leading edge of the airfoil, following its rigid motion. All speeds are defined in this system. Due to this change of reference, the effect of freestream cannot be expressed as $V_\infty(\cos\alpha, \sin\alpha)$ anymore. Indeed, if the airfoil pitches at rate $\Omega$ around a pivot at $(x_f, 0)$ and plunges at speed $(U_p, V_p)$ in the local system, the effective freestream velocity at point $(x, y)$ becomes

$$
\boldsymbol{V}_{\text{stream}} = \left[V_\infty \cos\left(\alpha - \psi\right) + U_p + \Omega y\right] \boldsymbol{e}_x + \left[V_\infty \sin\left(\alpha - \psi\right) + V_p - \Omega\left(x - x_f\right)\right] \boldsymbol{e}_y, \tag{2.16}
$$

where $\psi$ is the accumulated rotation angle since the beginning of the motion, corresponding to a change of the angle of attack. These newly introduced notations are illustrated in Figure 2.5.

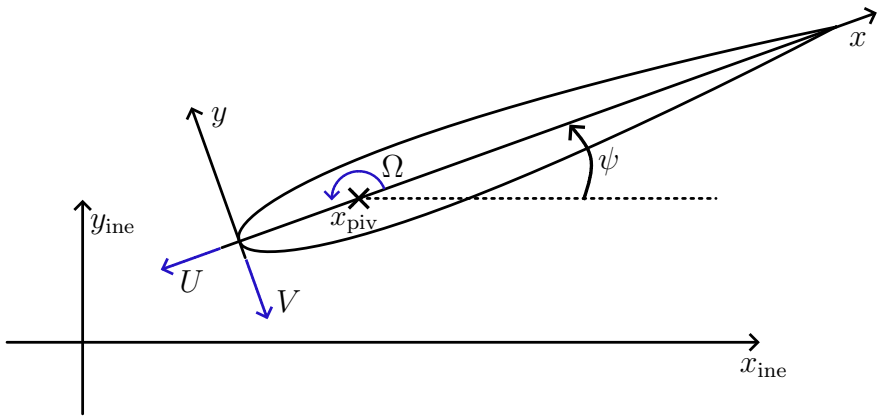


Figure 2.5: Illustration of the local coordinate system and airfoil movement for the UPM method. The translational velocity $(U, V)$ and angular velocity $\Omega$ are shown, as well as the accumulated rotation angle $\psi$.

In this model, the airfoil sheds a vortex at each time step $t_k$, creating a wake behind it. The extended geometry and discretization of the problem in local axes is shown in Figure 2.6.

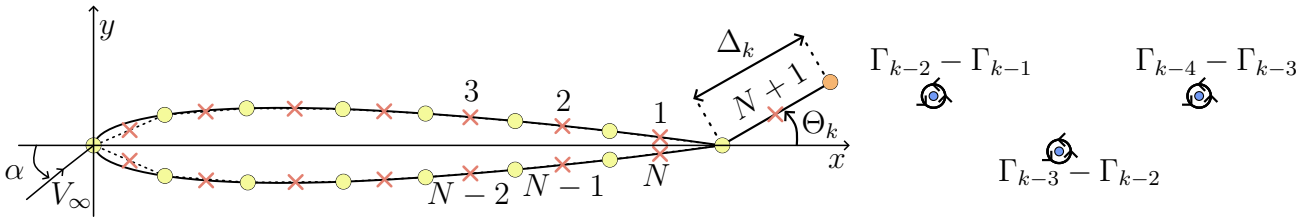


Figure 2.6: Representation of the airfoil panels, shed vortex panel and core vortices for the UPM method. Yellow circles are nodes, and crosses are control points. The blue circles are free vortices. The three first and last elements of the airfoil as well as the shed vortex panel are numbered. The freestream velocity $V_\infty$ at an angle $\alpha$ is also shown. Adapted from [12].

Due to Helmholtz's theorem, the total circulation $\Gamma$ around the airfoil and its wake is conserved. This means that any circulation change on the body needs to be exactly compensated by vortex shedding. In this model, a new vortex panel (called the *shed vortex* panel) is added at the trailing edge. This panel adds three new unknowns to the system being its size $\Delta_k$, its orientation $\Theta_k$ and its strength $\gamma_{w,k}$. The Helmholtz theorem allows expressing the vortex strength $\gamma_{w,k}$ as a function of the circulation around the airfoil at the previous and current time steps:

$$\gamma_k + \Delta_k \gamma_{w,k} = \Gamma_{k-1} \rightarrow \gamma_{w,k} = \frac{\Gamma_{k-1} - \Gamma_k}{\Delta_k} = \frac{l\,(\gamma_{k-1} - \gamma_k)}{\Delta_k}, \tag{2.17}$$

where $l$ is the perimeter of the airfoil.

Two additional equations are thus still needed for closure. Basu and Hancock [4] proposed two simple physical relations for this purpose. First, the shed vortex panel is oriented such that it is tangential to the local flow velocity at its midpoint. Then, its size is equal to the product of the magnitude of this velocity and the time step. The new influence coefficients $\left(B^t_{i,N+1}\right)_k$ and

$\left(B^n_{i,N+1}\right)_k$ are computed by equation (2.4) to describe the effect of this panel on the airfoil.

At each time step, the previous shed vortex panel is converted into a free vortex that is convected downstream. As a result, the vortex $m$ has a strength $(\Gamma_{m-1} - \Gamma_m)$. In order to obtain the effect of such a vortex on the panels speeds, new influence coefficients $C^n$ and $C^t$ are introduced. The influence of vortex $m$ on panel $i$ is thus modeled by

$$\begin{aligned}(C^n_{i,m})_k &= \frac{-\cos\left[\theta_i - (\theta_{i,m})_k\right]}{2\pi\,(r_{i,m})_k},\\ (C^t_{i,m})_k &= \frac{-\sin\left[\theta_i - (\theta_{i,m})_k\right]}{2\pi\,(r_{i,m})_k},\end{aligned} \tag{2.18}$$

where $(r_{i,m})_k$ is the distance between vortex $m$ and the center of panel $i$, and $(\theta_{i,m})_k$ is the angle between the horizontal and the segment containing the two points, as shown in Figure 2.7. These influence coefficients can also be used for the impact of one vortex on another one along $x$ and $y$, by setting $\theta_i = 0$.

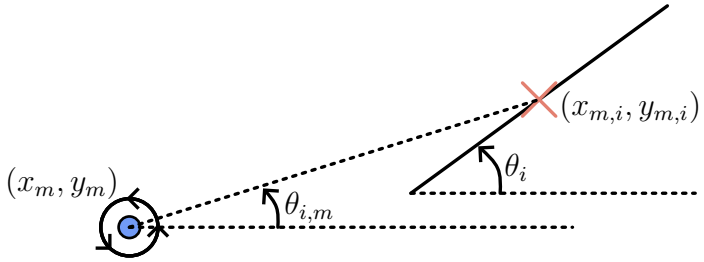


Figure 2.7: Representation of the angles between a vortex and a panel for the UPM method. The blue circle is the vortex $m$, while the cross is the control point of panel $i$. $\theta_i$ is the angle of panel $i$ from the horizontal, and $\theta_{i,m}$ is the angle between the horizontal and the segment containing the vortex and the control point.

Numerically, the presence of these moving singularities might pose some issues. Indeed, two core vortices could find themselves very close to each other after being convected. In this case, high nonphysical velocities would be induced between both vortices. Young [68] suggested the usage of finite viscous core vortices to avoid this issue. Concretely, each vortex is given a minimal influence radius. If two vortices are closer than this radius, their influence is limited by it. Young defined this distance as the one traveled by the vortex since the previous time step, which is also done here.

With the newly defined influence coefficients, speeds on any airfoil panel are written

$$\begin{aligned}
\left(V_i^t\right)_k =& \boldsymbol{V}_{\text{stream}} \cdot \boldsymbol{t}_i + \sum_{j=1}^{N} A_{ij}^t \left(\sigma_j\right)_k + \gamma_k \sum_{j=1}^{N} B_{ij}^t \\
&+ \gamma_{w,k} \left(B_{i,N+1}^t\right) + \sum_{m=1}^{k-1} \left(C_{i,m}^t\right)_k \left(\Gamma_{m-1} - \Gamma_m\right), \\
\left(V_i^n\right)_k =& \boldsymbol{V}_{\text{stream}} \cdot \boldsymbol{n}_i + \sum_{j=1}^{N} A_{ij}^n \left(\sigma_j\right)_k + \gamma_k \sum_{j=1}^{N} B_{ij}^n \\
&+ \gamma_{w,k} \left(B_{i,N+1}^n\right) + \sum_{m=1}^{k-1} \left(C_{i,m}^n\right)_k \left(\Gamma_{m-1} - \Gamma_m\right),
\end{aligned} \tag{2.19}$$

where $\boldsymbol{t}_i$ and $\boldsymbol{n}_i$ are the tangential and normal vectors to the panel $i$.

The velocities of the shed vortex panel $(u_{w,k}, v_{w,k})$ and the ones of the core vortices $(u_{h,k}, v_{h,k})$ can be obtained with the same formulas, by setting $\theta_i = 0$, and using the appropriate influence coefficients.

While the non-penetration conditions of the HSPM method still hold *i.e.*

$$\left(V_i^n\right)_k = 0 \qquad \forall\ i \in 1, \ldots, N, \tag{2.20}$$

the Kutta condition needs to be slightly modified with respect to its HSPM expression. Evaluating the unsteady Bernoulli's equation (2.7) on the first and last panels gives

$$\left(V_1\right)_k^2 - \left(V_N\right)_k^2 = 2\frac{\partial\left(\phi_N - \phi_1\right)}{\partial t}. \tag{2.21}$$

The potential difference $(\phi_N - \phi_1)$ is obtained by integrating speed over the airfoil

$$\phi_N - \phi_1 = \int_1^N \boldsymbol{V} \cdot d\boldsymbol{L}, \tag{2.22}$$

which is the definition of the circulation $\Gamma_k$. Using a backward finite difference for the time derivative, the Kutta condition (2.21) finally becomes

$$\left(V_1^t\right)_k^2 - \left(V_N^t\right)_k^2 = 2\frac{\Gamma_k - \Gamma_{k-1}}{\Delta t}. \tag{2.23}$$

The system of equations (2.20) and (2.23) to solve is nonlinear such that it cannot be solved as easily as in the steady case. In order to obtain a solution, fixed-point iterations are performed as they allow reaching convergence in a low number of iterations without the need to implement a Jacobian or finite-difference approximations of the gradients. At each time increment, the following steps are followed:

1. The dynamics are updated. The airfoil moves according to its prescribed motion.

2. The shed vortex and core vortices are convected downstream according to their speeds at the previous time. Since they are not attached to the airfoil, the airfoil motion between the previous and current time steps has to be subtracted in the local frame.

3. Initial guesses are chosen for both $\Theta_k$ and $\Delta_k$. Solutions of the previous time step are used here for $k > 1$.

4. Time step coefficients are computed (airfoil panels $\leftrightarrow$ core vortices, core vortices $\rightarrow$ core vortices). These do not depend on $\Theta_k$ nor $\Delta_k$, and thus do not need updating through inner iterations.

5. The new geometry of the shed vortex panel (mid- and endpoint) is computed, and inner iterations influence coefficients are updated (shed vortex $\leftrightarrow$ airfoil panels, shed vortex $\leftrightarrow$ core vortices).

6. The non-penetration condition $(V_i^n)_k = 0$ is written in the form $\boldsymbol{A^n}\boldsymbol{\sigma}_k^u = \gamma_k \boldsymbol{b}^u + \boldsymbol{c}^u$. After a few manipulations of equation (2.19), and substituting $\gamma_{w,k}$ with its expression of equation (2.17), this gives

$$\begin{aligned} b_i^u &= \left( \frac{l}{\Delta_k} \left(B_{i,N+1}^n\right)_k - \sum_{j=1}^{N} B_{ij}^n \right), \\ c_i^u &= -\boldsymbol{V}_{\text{stream}} \cdot \boldsymbol{n}_i - \left( \frac{l}{\Delta_k} \right) \gamma_{k-1} \left(B_{i,N+1}^n\right)_k - \sum_{m=1}^{k-1} \left(C_{i,m}^n\right)_k \left(\Gamma_{m-1} - \Gamma_m\right). \end{aligned} \tag{2.24}$$

   The solution of this system as a function of $\gamma_k$ can be obtained as

$$\boldsymbol{\sigma}_k^u = \gamma_k \left(\boldsymbol{A^n}\right)^{-1} \boldsymbol{b}^u + \left(\boldsymbol{A^n}\right)^{-1} \boldsymbol{c}^u = \gamma_k \boldsymbol{s_1}^u + \boldsymbol{s_2}^u, \tag{2.25}$$

   where $\boldsymbol{s_1}^u$ and $\boldsymbol{s_2}^u$ are computed from the LU decomposition of the $\boldsymbol{A^n}$ matrix.

7. The Kutta condition is solved for $\gamma_k$. By introducing the result $\boldsymbol{\sigma}_k = \boldsymbol{s_1}^u \gamma_k + \boldsymbol{s_2}^u$ into (2.19), the tangential velocity can be expressed as a function of $\gamma_k$

$$\left(V_i^t\right)_k = a\gamma_k + b. \tag{2.26}$$

   Then, equation (2.23) simply becomes a quadratic function of $\gamma_k$ to solve for analytically. Knowing $\gamma_k$, $\boldsymbol{\sigma}_k$ can be obtained as well.

8. The shed vortex velocities $(u_{w,k}, v_{w,k})$ are evaluated. $\Theta_k$ and $\Delta_k$ are updated from the following relations

$$\begin{aligned} \Theta_k &= \arctan \frac{v_{w,k}}{u_{w,k}}, \\ \Delta_k &= \Delta t \sqrt{u_{w,k}^2 + v_{w,k}^2}. \end{aligned} \tag{2.27}$$

   If $\Theta_k$ and $\Delta_k$ have converged to the prescribed tolerance or if the maximal number of iterations is reached, the inner iterations are terminated. Else, a new iteration is started from step 5.

9. The velocities at the core vortices $(u_{h,k}, v_{h,k})$ are computed for the next time step.

10. The pressure coefficients $(C_{p,i})$ are computed on the panels. In local axes, equation (2.8) is slightly modified to

$$C_{p,i} = \left(\frac{V_{\text{stream}}}{V_\infty}\right)^2 - \left(\frac{V_i}{V_\infty}\right)^2 + \frac{2}{V_\infty^2}\left(\frac{\partial \phi_\infty}{\partial t} - \frac{\partial \phi_i}{\partial t}\right). \tag{2.28}$$

The introduction of the potential $\phi$ in the pressure coefficient expression makes it significantly more complex to compute than in the steady case. Indeed, the potential is not directly available, and has to be computed by integrating the speeds from infinity to the considered panel. According to Katz and Plotkin [32], the potential at infinity can be approximated as zero.

In order to compute the potential, a line is first drawn from infinity to the leading edge. It is then discretized into a series of panels, on which the tangential velocity induced by the singularity distribution is computed. The potential at the leading edge is then computed by integrating the tangential velocity along the line. This process is continued on the airfoil surface, on the upper and lower surfaces both starting from the leading edge potential value. The time derivative of the potential at a panel is then estimated by a backward finite difference.

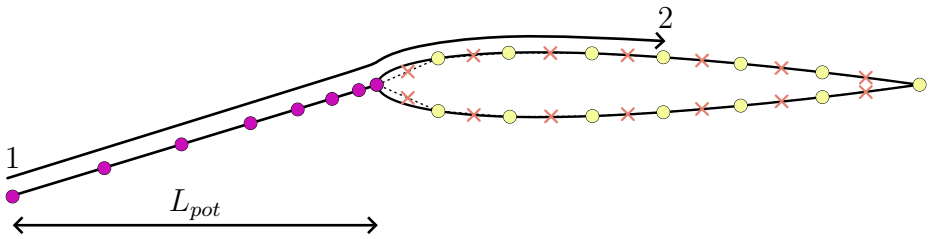


Figure 2.8: Representation of the integration path for the potential calculation (not to scale). $L_{pot}$ is the distance from the leading edge of the start of the integration. Adapted from [68].

The numerical definition of infinity, as well as the number of elements to discretize the path $N_{pot}$ are not trivial. While Teng [52] chose a distance of $L_{pot}$ of ten chords from the airfoil, Young [68] used a much higher distance of five hundred chords. A convergence analysis is performed to ensure the chosen length and the number of elements are sufficient. This is shown in Figure 2.9. The case for this analysis is the starting flow of a NACA0012 at 5° angle of attack. The potential at the leading edge after one second is calculated with different values of $L_{pot}$ for a fixed value of $N_{pot} = 1000$. As can be seen in Figure 2.9a, a distance of a hundred chords is sufficient to obtain a reasonable convergence. The same analysis is performed with different values of $N_{pot}$ and a fixed value of $L_{pot} = 100$. As shown in Figure 2.9b, 200 elements are sufficient.

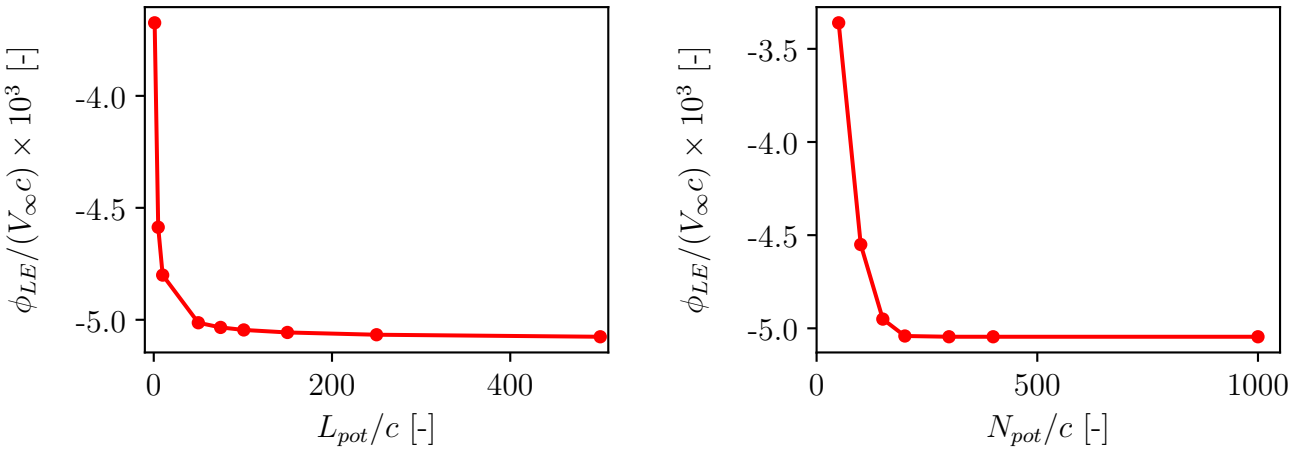


(a) Length of the domain ($N_{pot} = 1000$). (b) Number of elements on the domain ($L_{pot} = 100$).

Figure 2.9: Convergence analysis of the unsteady potential calculation with respect to the distance $L_{pot}$ and the number of elements $N_{pot}$ representing infinity.

Finally, the complete process of the UPM method is summarized in Figure 2.10.

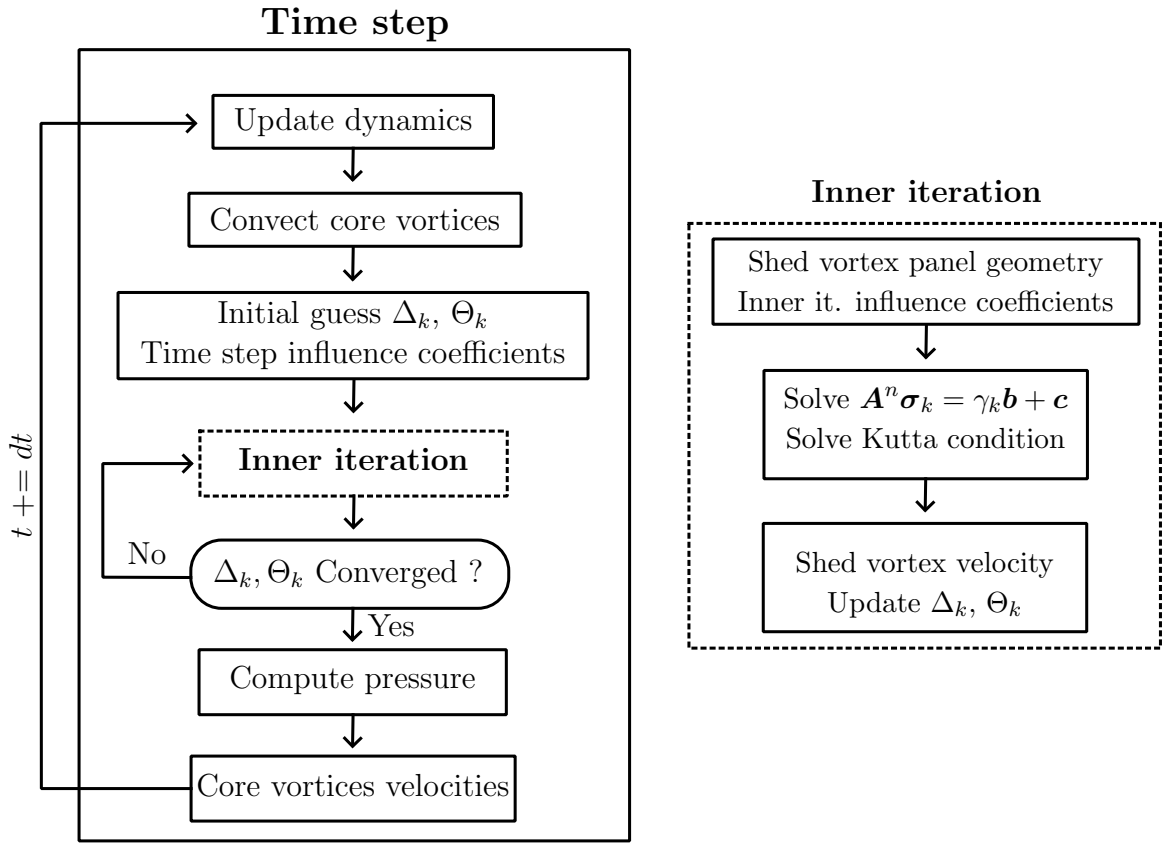


Figure 2.10: Flowchart of the different steps of the UPM method.

### 2.2.3 Discussion and alternatives

The main drawback of the UPM method presented here stems from its core concept. The cost of an iteration can be roughly estimated to be proportional to the number of influence coefficients to compute. This amounts to the order of $(N + m) \times m$ operations per time step, where $m$ is the number of core vortices. As the number of time steps increases, the cost grows quadratically, which can quickly become prohibitive and undermine the interest of a panel method.
If numerous steps are required to be computed, other methods might be more suitable. Grid-based solvers such as finite elements or finite volumes have the advantage of requiring a relatively constant cost per time step. As an added benefit, their ability to represent unsteady flow features is generally better than that of panel methods. However, their baseline cost is higher, and the meshing process can be cumbersome. Fortunately, in the present work, the number of calls to the inviscid solver is typically low compared to the number of panels such that this issue is not critical.

Even within the realm of panel methods, the HSPM and UPM are not the only options.
Drela [21], for instance, used a method that is particularly well suited for VII coupling in XFOIL. The inviscid flow is first solved by a series of vortices on the panels. Then, the effect of blowing velocity is taken into account by a distribution of sources on the panels. This allows to significantly reduce computational costs, since the complete potential flow does not need to be recomputed at each coupling iteration. This approach is unfortunately not easily extendable to unsteady flows.

The order of accuracy of such methods can also be increased by considering curved panels, or by varying the strength of the singularities linearly along the panel. The latter was the approach followed by Ozdemir *et al.* [43]. $N+1$ vortex singularities are placed on the points of the discretized airfoils. The vortex strength along the panel is then varied linearly between its two endpoints. This approach does not come with a significant increase in computational cost, but its implementation is more complex due to longer mathematical expressions for influence coefficients.

To increase the accuracy of the vortex shedding mechanism of the UPM method, a double wake model can be considered. Vaithiyanathasamy *et al.* [54] modeled the "wake" as two separate sheets of vortices; the classical one located at the trailing edge, and a new one which location can be specified. This approach shows great potential, improving results compared to the single wake model but once again comes at the cost of increased complexity.

# 3 Viscous region

The present work implements changes into Dechamps' [18] viscous solver to allow for unsteady VII coupling. This is done through the modification of the time integration scheme and the handling of transition. The simplifications made in the present model compared to a time accurate solver are also highlighted.

The viscous region exhibits much richer physics than the invscid one. Complex phenomena such as stall and separation can only be captured by a viscous solver. The extent of viscous effects is quantified by the freestream Reynolds number, defined here as

$$\mathrm{Re} = \frac{V_\infty c}{\nu}, \tag{3.1}$$

where $V_\infty$ is the freestream velocity, $c$ the chord of the body and $\nu$ the kinematic viscosity of the fluid. At low Reynolds numbers, viscous effects dominate the inertial ones, and vice versa at high Reynolds numbers.

The theory and numerics of the viscous solver are reminded in the following sections. For more details, refer to Dechamps [18]. Note that he focused on the study of transonic flows, such that compressibility could not be neglected. Where applicable, the incompressible equivalents of equations are briefly mentioned.

## 3.1 Theory

Like in inviscid flows, the assumptions of two-dimensionality and negligible thermal effects are made. Additionally, two key assumptions allow to obtain the governing equations of the boundary layer. The first one is that it is a thin region, meaning that the thickness of the boundary layer $\delta$ is much smaller than the chord of the studied body. The second assumption is that the Reynolds number is large, such that viscous effects are moderate in the boundary layer.

### 3.1.1 Boundary layer equations

In order to allow for simplifications of the Navier-Stokes equations, a coordinate system is introduced that follows the body surface. The coordinate $\xi$ is defined as the distance tangent to the body surface, growing downstream. $\eta$ is the distance normal to the body, growing away from it. The velocity components are then defined as $u = \boldsymbol{u} \cdot \boldsymbol{e}_\xi$ and $v = \boldsymbol{u} \cdot \boldsymbol{e}_\eta$. This system of coordinates is illustrated in Figure 3.1.

The boundary layer thickness $\delta$ is small compared to the size of the body, and the no-slip condition applies at the surface, while the velocity is the inviscid one $u_e$ at $\eta = \delta$. This means that velocity gradients in the $\eta$ direction are large compared to those in the $\xi$ direction. Additionally, the velocity components $v$ are much smaller than $u$.
In the system $(\xi, \eta)$, the continuity part of the Navier-Stokes equations (2.1a) becomes

$$\frac{\partial \rho}{\partial t} + \frac{\partial}{\partial \xi}(\rho u) + \frac{\partial}{\partial \eta}(\rho v) = 0. \tag{3.2}$$

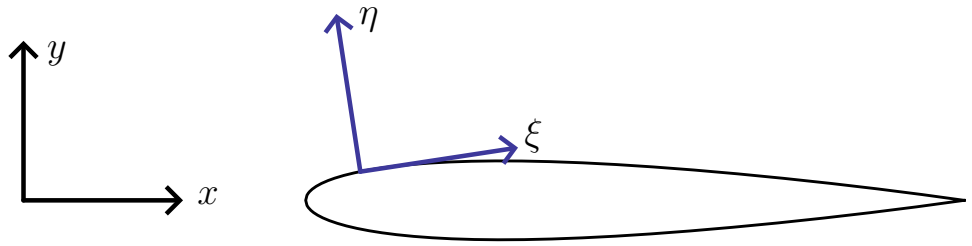


Figure 3.1: Boundary layer coordinates system. Adapted from [18].

For a Newtonian fluid, and in the absence of body forces, the momentum equation (2.1b) is written

$$\frac{\partial}{\partial t}(\rho \boldsymbol{u}) + \nabla \cdot (\rho \boldsymbol{u}\boldsymbol{u}) = -\nabla p + \mu \left( \Delta \boldsymbol{u} + \frac{1}{3} \nabla (\nabla \cdot \boldsymbol{u}) \right). \tag{3.3}$$

In the $\xi$ direction, this writes

$$\frac{\partial}{\partial t}(\rho u) + \rho u \frac{\partial u}{\partial \xi} + u \frac{\partial}{\partial \xi}(\rho u) + \rho v \frac{\partial u}{\partial \eta} + u \frac{\partial}{\partial \eta}(\rho v) = -\frac{\partial p}{\partial \xi} + \mu \left[ \frac{\partial^2 u}{\partial \xi^2} + \frac{\partial^2 u}{\partial \eta^2} + \frac{1}{3} \left( \frac{\partial^2 u}{\partial \xi^2} + \frac{\partial^2 v}{\partial \xi \partial \eta} \right) \right]. \tag{3.4}$$

The left-hand side can be simplified by developing the first term, and using the continuity equation (3.2) to obtain

$$\rho \frac{\partial u}{\partial t} + \rho u \frac{\partial u}{\partial \xi} + \rho v \frac{\partial u}{\partial \eta} = \text{RHS}. \tag{3.5}$$

On the right-hand side, the terms $\frac{\partial^2 u}{\partial \xi^2}$ and $\frac{\partial^2 v}{\partial \xi \partial \eta}$ can be neglected with respect to $\frac{\partial^2 u}{\partial \eta^2}$ since the variations in $\eta$ are more important than those in $\xi$, and the velocity $v$ is much smaller than $u$. The momentum equation then becomes

$$\rho \frac{\partial u}{\partial t} + \rho u \frac{\partial u}{\partial \xi} + \rho v \frac{\partial u}{\partial \eta} = -\frac{\partial p}{\partial \xi} + \mu \frac{\partial^2 u}{\partial \eta^2}. \tag{3.6}$$

Additionally, the pressure gradient in the $\xi$ direction can be written as a function of the inviscid velocity $u_e$. Indeed, for large Reynolds numbers, Schlichting and Gersten [48] proved that the pressure is constant through the boundary layer thickness. Thus, the pressure at a location $(\xi, \eta)$ can be written as $p(\xi, \eta) = p_e(\xi)$, where $p_e$ is the inviscid pressure at the edge of the boundary layer. The inviscid pressure gradient can directly be obtained from the momentum equation, as pointed out by Van Es [55]. Indeed, by neglecting the viscous term in the momentum equation (3.6), and by assuming that at the edge of the boundary layer the fluid is parallel to the surface (*i.e.* $v_e = 0$), the pressure gradient is

$$-\frac{\partial p_e}{\partial \xi} = \rho_e \frac{\partial u_e}{\partial t} + \rho_e u_e \frac{\partial u_e}{\partial \xi}. \tag{3.7}$$

Finally, the unsteady, compressible **Boundary Layer Equations** governing the flow in the viscous region are

$$\text{Continuity:} \quad \frac{\partial \rho}{\partial t} + \frac{\partial}{\partial \xi}(\rho u) + \frac{\partial}{\partial \eta}(\rho v) = 0, \tag{3.8a}$$

$$\text{Momentum:} \quad \rho \frac{\partial u}{\partial t} + \rho u \frac{\partial u}{\partial \xi} + \rho v \frac{\partial u}{\partial \eta} = \rho_e \frac{\partial u_e}{\partial t} + \rho_e u_e \frac{\partial u_e}{\partial \xi} + \mu \frac{\partial^2 u}{\partial \eta^2}. \tag{3.8b}$$

Within the scope of this work, these equations effectively simplify to their incompressible form (3.9), which is used for instance by Ye [67].

$$\text{Continuity:} \quad \frac{\partial u}{\partial \xi} + \frac{\partial v}{\partial \eta} = 0, \tag{3.9a}$$

$$\text{Momentum:} \quad \frac{\partial u}{\partial t} + u\frac{\partial u}{\partial \xi} + v\frac{\partial u}{\partial \eta} = \frac{\partial u_e}{\partial t} + u_e\frac{\partial u_e}{\partial \xi} + \nu\frac{\partial^2 u}{\partial \eta^2}. \tag{3.9b}$$

### 3.1.2 Integral boundary layer equations

While the evolution of the velocity in the $\xi$ direction is of great importance for VII, the details along the $\eta$ direction are less relevant for aerodynamic purposes. The boundary layer equations can thus be integrated along the boundary layer thickness reducing the number of space dimensions to only one. These integrated equations can then be combined to obtain the $n$-th moment of the boundary layer equation, following Von Kármán [60]

$$n\text{-th moment} = (n+1)\,u^n \times \int_0^\delta \text{Momentum}\ \mathrm{d}\eta - \left(u_e^{n+1} - u^{n+1}\right) \times \int_0^\delta \text{Continuity}\ \mathrm{d}\eta.$$

The 0-th and 1-st moments of the momentum equation are used by Dechamps [18], just like Ozdemir et al. [43] did. Neither considered the effect of compressibility in the unsteady terms, as they vanish when the steady state is reached. In the steady terms, small modifications used by Drela and Giles [22] are made.

In order to write out these equations concisely, a series of new integral quantities have to be defined.

- The momentum thickness $\theta = \int_0^\delta \left(\frac{\rho u}{\rho_e u_e}\right)\left[1 - \frac{u}{u_e}\right] d\eta$,
- The displacement thickness $\delta^* = \int_0^\delta \left(1 - \frac{\rho u}{\rho_e u_e}\right) d\eta$, and its associated boundary layer shape factor $H = \frac{\delta^*}{\theta}$,
- The kinetic energy thickness $\theta^* = \int_0^\delta \left(\frac{\rho u}{\rho_e u_e}\right)\left[1 - \frac{u^2}{u_e^2}\right] d\eta$, and shape parameter $H^* = \frac{\theta^*}{\theta}$,
- The density thickness $\delta^{**} = \int_0^\delta \left(\frac{u}{u_e}\right)\left[1 - \frac{\rho}{\rho_e}\right] d\eta$, and shape parameter $H^{**} = \frac{\delta^{**}}{\theta}$
- The kinematic shape parameter $H_k = \dfrac{\int_0^\delta \left(1 - \frac{u}{u_e}\right) d\eta}{\int_0^\delta \left(\frac{u}{u_e}\right)\left[1 - \frac{u}{u_e}\right] d\eta}$,
- The local skin friction coefficient $c_f = \dfrac{\tau_w}{\frac{1}{2}\rho_e u_e^2}$, where $\tau_w$ is the wall shear stress $\tau_w = \mu \left.\dfrac{\partial u}{\partial \eta}\right|_{\eta=0}$,

- The local dissipation coefficient $c_{ds} = \dfrac{1}{\rho_e u_e^3} \displaystyle\int_0^\delta \tau \frac{\partial u}{\partial \eta}\, d\eta$,

The integral boundary layer equations are then written as

$$\frac{H}{u_e}\frac{\partial \theta}{\partial t} + \frac{\theta}{u_e}\frac{\partial H}{\partial t} + \frac{\theta H}{u_e^2}\frac{\partial u_e}{\partial t} = -\frac{\partial \theta}{\partial \xi} - \left(2 + H - M_e^2\right)\frac{\theta}{u_e}\frac{\partial u_e}{\partial \xi} + \frac{c_f}{2} \tag{3.10a}$$

$$\begin{aligned}\frac{1 + H\left(1 - H^*\right)}{u_e}\frac{\partial \theta}{\partial t} + \frac{1 + \theta\left(1 - H^*\right)}{u_e}\frac{\partial H}{\partial t} + \frac{\theta\left(2 - H^* H\right)}{u_e^2}\frac{\partial u_e}{\partial t} \\ = -\theta\frac{\partial H^*}{\partial \xi} - \left(2H^{**} + H^*\left(1 - H\right)\right)\frac{\theta}{u_e}\frac{\partial u_e}{\partial \xi} + 2c_{ds} - H^*\frac{c_f}{2}.\end{aligned} \tag{3.10b}$$

This approach is called the *dissipation integral method* [53]. It is made of an unsteady form of the Von Kármán momentum equation (3.10a), and the kinetic energy shape parameter equation (3.10b). In incompressible flow, the only simplifications are the removal of the terms in $M_e$ and $H^{**}$.

Note that the dissipation integral method is not the only possibility to solve the viscous region. While some like Ye [67] use the entrainment integral method [27] which is based on the same principles as the dissipation integral method, others like Cebeci and Bradshaw [10] use a one-equation model instead. The main issue with this approach is that it is unable to model separated flows [22]. Newer models, such as the one of Drela [19] allow for a wide range of validity including separated flow and crossover profiles. This is done through the addition of new equations adding accuracy to the model at the cost of complexity.

### 3.1.3 Closure

Due to their number of unknowns, the integral boundary layer equations cannot be solved without additional information. This comes through the usage of closure relations, which are assumptions about the behavior of the boundary layer.
Dechamps [18] selected appropriate closure relations for steady computations, and pointed out that these need to be adapted for unsteady calculations, backed by the claims of Cousteix and Cebeci [15]. While this is true, there have been examples of successful unsteady computations with steady closures, such as the work of Garcia [25] or Riziotis [47]. The latter states that "[the uncorrected closures] *can only be used on the condition that relatively slow unsteady flows are considered*". As a starting point, it is thus interesting to limit the analysis to these simpler cases, neglecting unsteady terms in closure relations in order to investigate other potential shortcomings of the present model.

For compressible flow, the kinematic shape parameter is [61]

$$H_k = \frac{H - 0.29M_e^2}{1 + 0.113M_e^2}. \tag{3.11}$$

The closure relations relate $H^*, H^{**}, c_f$ and $c_{ds}$ to the shape parameter $H$, the Mach number $M_e$ and the momentum thickness Reynolds number

$$\mathrm{Re}_\theta = \frac{\rho_e u_e \theta}{\mu_e}. \tag{3.12}$$

Due to the change of physics through transition, different closure relations are considered for the laminar and turbulent regions.
Most of the closure relations are taken from the work of Drela and Giles [22], or directly from XFOIL's source code [66] (version 6.99).

- **In the laminar region**
  The kinematic energy shape parameter is [24]

$$H^* = \begin{cases} 1.528 + 0.0111\dfrac{(H_k - 4.35)^2}{H_k + 1} - 0.0278\dfrac{(H_k - 4.35)^3}{H_k + 1} \\ \qquad -0.0002\left[(H_k - 4.35)\, H_k\right]^2, & \text{if } H_k < 4.35, \\ 1.528 + 0.015\dfrac{(H_k - 4.35)^2}{H_k}, & \text{if } H_k \geq 4.35, \end{cases} \tag{3.13}$$

  and can be corrected for compressibility

$$H^* = \frac{H^* + 0.028 M_e^2}{1 + 0.014 M_e^2}. \tag{3.14}$$

  The density shape parameter is

$$H^{**} = \left(\frac{0.064}{H_k - 0.8} + 0.251\right) M_e^2. \tag{3.15}$$

  The local friction coefficient is

$$c_f = \frac{2}{\mathrm{Re}_\theta}\overline{c_f}, \tag{3.16}$$

  where

$$\overline{c_f} = \begin{cases} \dfrac{1}{2}\left[-0.07 + 0.0727\dfrac{(5.5 - H_k)^3}{H_k + 1}\right], & H_k < 5.5 \\ \dfrac{1}{2}\left[-0.07 + 0.015\left(1 - \dfrac{1}{H_k - 4.5}\right)^2\right], & H_k \geq 5.5. \end{cases} \tag{3.17}$$

  And the local dissipation coefficient is

$$c_{ds} = \frac{H^*}{2\mathrm{Re}_\theta}\overline{c_d}, \tag{3.18}$$

  where

$$\overline{c_d} = \begin{cases} 0.207 + 0.00205\,(4 - H_k)^{5.5}, & H_k < 4 \\ 0.207 - 0.0016\dfrac{(H_k - 4)^2}{1 + 0.02\,(H_k - 4)^2}, & H_k \geq 4. \end{cases} \tag{3.19}$$

- **In the turbulent region**
  The kinematic energy shape parameter is

$$H^* = \begin{cases} 1.5 + \dfrac{4}{\mathrm{Re}_\theta} + \left(0.5 - \dfrac{4}{\mathrm{Re}_\theta}\right)\left(\dfrac{H_0 - H_k}{H_0 - 1}\right)^2 \left(\dfrac{1.5}{H_k + 0.5}\right), & H_k < H_0, \\ 1.5 + \dfrac{4}{\mathrm{Re}_\theta} + (H_k - H_0)^2 \left[\dfrac{0.007 \ln \mathrm{Re}_\theta}{\left(H_k - H_0 + \dfrac{4}{\ln \mathrm{Re}_\theta}\right)^2} + \dfrac{0.015}{H_k}\right], & H_k \geq H_0, \end{cases} \tag{3.20}$$

  where

$$H_0 = \begin{cases} 3 + \dfrac{400}{\mathrm{Re}_\theta}, & \mathrm{Re}_\theta \geq 400 \\ 4, & \mathrm{Re}_\theta < 400. \end{cases} \tag{3.21}$$

  The compressibility correction is the same as for laminar flow (3.14).
  The density shape parameter is

$$H^{**} = \left(\frac{0.064}{H_k - 0.8} + 0.251\right) M_e^2. \tag{3.22}$$

  The local friction coefficient is obtained from [42]

$$F_c c_f = \frac{0.3 e^{-1.33 H_k}}{\left(\dfrac{\ln \mathrm{Re}_\theta}{2.3026}\right)^{-1.74 - 0.31 H}} + 0.00011 \left[\tanh\left(4 - \frac{H_k}{0.875}\right) - 1\right], \tag{3.23}$$

  where $F_c = \sqrt{1 + 0.2 M_e^2}$.
  The local dissipation coefficient is given by [66]

$$c_{ds} = c_{d_w} + c_{d_d} + c_{d_l}, \tag{3.24}$$

  where

$$c_{d_w} = \frac{1}{4} c_f U_s \left(1 + \tanh \frac{H_k - 1}{1 + 2.1/\ln \mathrm{Re}_\theta}\right), \tag{3.25}$$

$$c_{d_d} = (0.995 - U_s)\, C_\tau, \tag{3.26}$$

$$c_{d_l} = \frac{0.15\,(0.995 - U_s)^2}{\mathrm{Re}_\theta}, \tag{3.27}$$

  in which

$$U_s = 0.5 H^* \left(1 - \frac{4\,(H_k - 1)}{3H}\right), \tag{3.28}$$

  and the shear stress coefficient $C_\tau$ is obtained by solving the shear lag equation

$$\begin{aligned} \frac{\delta}{U_s u_e C_\tau}\frac{\partial C_\tau}{\partial t} + \frac{2\delta}{U_s u_e^2}\frac{\partial u_e}{\partial t} + \frac{\delta}{C_\tau}\frac{\partial C_\tau}{\partial \xi} &= 5.6\left(C_{\tau EQ}^{1/2} - C_\tau^{1/2}\right) \\ &+ 2\delta\left\{\frac{4}{3\delta^*}\left[\frac{c_f}{2} - \left(\frac{H_k - 1}{6.7 H_k}\right)^2\right] - \frac{1}{u_e}\frac{\partial u_e}{\partial \xi}\right\}, \end{aligned} \tag{3.29}$$

where

$$C_{\tau_{EQ}} = 0.015 H^* \frac{(H_k - 1)\, H_{k,c}^2}{(1 - U_s)\, H_k^2 H}, \qquad H_{k,c} = H_k - 1 - \frac{18}{\mathrm{Re}_\theta}. \tag{3.30}$$

In the turbulent region, this is thus one more equation that needs to be solved.

### 3.1.4 Transition

Transition from laminar to turbulent flow is a complex phenomenon that has a significant impact on the boundary layer; its accurate prediction is thus essential. Physically, the flow becomes turbulent due to the growth of Tollmien-Schlichting waves.

A simple model for transition prediction is the $e^N$ method by Smith [49] and Van Ingen [56], and implemented by Dechamps [18]. The $e^N$ method's main idea is to estimate the amplification of the Tollmien-Schlichting waves semi-empirically. For attached flows, the evolution of the amplification ratio $\tilde{N}(\xi)$ is given by

$$\frac{\partial \tilde{N}}{\partial \xi} = \frac{\mathrm{d}\tilde{N}}{\mathrm{dRe}_\theta} \frac{\mathrm{dRe}_\theta}{\mathrm{d}\xi}, \tag{3.31}$$

where the two required slopes are obtained from the following empirical relations [20]

$$\frac{\mathrm{d}\tilde{N}}{\mathrm{dRe}_\theta} = 0.028\,(H_k - 1) - 0.0345 \exp\left(-\left(\frac{3.87}{H_k - 1} - 2.52\right)^2\right), \tag{3.32}$$

$$\theta \frac{\mathrm{dRe}_\theta}{\mathrm{d}\xi} = -0.05 + \left(\frac{2.7}{H_k - 1}\right) - \left(\frac{5.5}{H_k - 1}\right)^2 + \left(\frac{3}{H_k - 1}\right)^3 + 0.1 \exp\left(\frac{-20}{H_k - 1}\right). \tag{3.33}$$

The waves only grow when a critical Reynolds number $\mathrm{Re}_{\theta_{crit}}$ is reached, given by Drela [20] as

$$\log_{10}\left(\mathrm{Re}_{\theta_{crit}}\right) = 2.492 \left(\frac{1}{H_k - 1}\right)^{0.43} + 0.7 \left(\tanh\left(\frac{14}{H_k - 1} - 9.24\right) + 1\right). \tag{3.34}$$

A numerical smoothing factor is also used by Drela

$$R_{fac} = \begin{cases} 0, & R_{norm} \leq 0 \\ 3R_{norm}^2 - 2R_{norm}^3, & 0 < R_{norm} < 1, \\ 1, & R_{norm} \geq 1, \end{cases} \tag{3.35}$$

where

$$R_{norm} = \frac{\log_{10}\left(\mathrm{Re}_\theta\right) - \log_{10}\left(\mathrm{Re}_{\theta_{crit}} + 0.08\right)}{0.16}. \tag{3.36}$$

And the attached flow amplification ratio evolution is

$$\frac{\partial \tilde{N}}{\partial \xi} = R_{fac} \frac{\mathrm{d}\tilde{N}}{\mathrm{dRe}_\theta} \frac{\mathrm{dRe}_\theta}{\mathrm{d}\xi}. \tag{3.37}$$

Under the form (3.37), detached flows ($H_k \geq 3.5$) transition cannot be predicted. A new component $A_s$ [20] is thus added to account for this

$$\theta A_s = 0.086 \tanh\left[1.2\left(\log_{10} \mathrm{Re}_\theta - 0.3 + 0.35\exp\left(-0.15\left(H_k - 5\right)\right)\right)\right] - \left(\frac{0.25}{H_k - 1}\right)^{1.5}. \tag{3.38}$$

This correcting term is added to the transition equation with a weighting factor $H_{fac}$ defined as

$$H_{fac} = \begin{cases} 0 & H_{norm} \leq 0, \\ 3H_{norm}^2 - 2H_{norm}^3, & 0 < H_{norm} < 1, \\ 1, & H_{norm} \geq 1, \end{cases} \tag{3.39}$$

where

$$H_{norm} = \frac{H_k - 3.5}{4 - 3.5}. \tag{3.40}$$

The steady amplification equation is then

$$\frac{\partial \tilde{N}}{\partial \xi} = \left(1 - H_{fac}\right) R_{fac} \frac{\mathrm{d}\tilde{N}}{\mathrm{dRe}_\theta} \frac{\mathrm{dRe}_\theta}{\mathrm{d}\xi} + H_{fac} A_s. \tag{3.41}$$

In order to perform pseudo time-stepping on the transition equation, Dechamps [18] added the equation $\partial \tilde{N}/\partial t = 0$ to the transition equation, resulting in

$$\frac{\partial \tilde{N}}{\partial t} + \frac{\partial \tilde{N}}{\partial \xi} = \left(1 - H_{fac}\right) R_{fac} \frac{\mathrm{d}\tilde{N}}{\mathrm{dRe}_\theta} \frac{\mathrm{dRe}_\theta}{\mathrm{d}\xi} + H_{fac} A_s. \tag{3.42}$$

This equation is solved for points in the laminar regime to obtain their value of $\tilde{N}$.
The flow becomes turbulent when $\tilde{N}$ reaches a critical value depending on the free-stream turbulence intensity $T_u$ following a law given by Drela and Giles [22]

$$\tilde{N}_{crit} = -8.43 - 2.4\ln\left(T_u\right). \tag{3.43}$$

Dechamps [18] uses a constant value of $\tilde{N}_{crit} = 9$, corresponding to a turbulence intensity of $T_u = 0.07\%$. This value can be adjusted depending on the application.

#### 3.1.4.1 Unsteady transition

The addition of unsteady effects into equation (3.42) adds the following term to equation (3.42)

$$\frac{\mathrm{d}\tilde{N}}{\mathrm{dRe}_\theta} \frac{\mathrm{dRe}_\theta}{\mathrm{d}t}. \tag{3.44}$$

The problem with this addition is $\mathrm{dRe}_\theta/\mathrm{d}t$. As pointed out by Ye [67], there is no empirical relation for this term. He expressed it with a first-order Taylor expansion; here it is simply discarded. To model unsteady transition, Krumbein *et al.* [33] and Windte *et al.* [65] worked on a "full" $e^N$ model. It is however complex, requiring to keep track of multiple waves, and is not considered in the present work.

### 3.1.5 Wake

In the current model [18], the wake is considered as a fully turbulent layer. The turbulent equations and closure relations used for the airfoil surface are still valid, with only small modifications. In the shear lag equation (3.29), a correction dissipation ratio $R_d = 0.9$ is added to yield

$$\begin{aligned}\frac{\delta}{U_s u_e C_\tau}\frac{\partial C_\tau}{\partial t} + \frac{2\delta}{U_s u_e^2}\frac{\partial u_e}{\partial t} + \frac{\delta}{C_\tau}\frac{\partial C_\tau}{\partial \xi} &= 5.6\left(C_{\tau_{EQ}}^{1/2} - C_\tau^{1/2} R_d\right) \\ &+ 2\delta\left\{\frac{4}{3\delta^*}\left[\frac{c_f}{2} - \left(\frac{H_k - 1}{6.7 H_k R_d}\right)^2\right] - \frac{1}{u_e}\frac{\partial u_e}{\partial \xi}\right\},\end{aligned} \tag{3.45}$$

The local skin friction coefficient $c_f$ and $c_{d_w}$ are set to zero. $H_{k,c}$ is modified to

$$H_{k,c} = H_k - 1, \tag{3.46}$$

and the local dissipation coefficient is doubled since the wake is made of two viscous layers.

### 3.1.6 Drag

In viscous flows, the drag can be split into the contributions of skin friction and pressure drag. The former can be obtained by integrating the local skin friction coefficient $c_f$ that is readily available when the boundary layer equations are solved. The latter cannot however be obtained directly from the current VII model. Indeed, the inviscid panel method is affected by the d'Alembert paradox, and thus predicts zero pressure drag. Fortunately, the total drag can be estimated based on the Squire and Young [50] formula, used by Dechamps [18]

$$c_d = 2\theta\,(u_e)^{\frac{H+5}{2}}\Big|_{\text{last wake point}}. \tag{3.47}$$

This indirectly allows to estimate the pressure drag coefficient

$$c_{d,p} = c_d - c_{d,f}. \tag{3.48}$$

## 3.2 Implementation

In the previous section, the set of equations governing the viscous region was obtained. It can be written in the form

$$\boldsymbol{A}(\boldsymbol{U})\frac{\partial \boldsymbol{U}}{\partial t} + \boldsymbol{B}(\boldsymbol{U})\frac{\partial \boldsymbol{U}}{\partial \xi} = \boldsymbol{C}(\boldsymbol{U}), \tag{3.49}$$

where $\boldsymbol{U}$ is the vector of unknowns.

In order to solve this system, both a time and a space discretization are required to get rid of the partial derivatives. Additionally, the system needs to be supplied with appropriate initial and boundary conditions.

Instead of solving the system simultaneously for all points, each point is treated separately starting from the leading edge stagnation point and going downstream. This approach is better

suited for this transitional problem.

The following sections describe the numerical methods used to solve the viscous region equations.

### 3.2.1 Space discretization

The geometry discretization along the airfoil is the same as the one of the inviscid region. This way, transfer of information between both solvers is facilitated. Rather than using control points such as in the inviscid solver, the calculations are made directly on the points. Additionally, the viscous solver divides the mesh into three regions: the top surface, the bottom surface and the wake. The top and bottom surfaces are separated by the stagnation point, near the leading edge. The wake region is made of a distribution of points along a straight line downstream of the airfoil inclined at an angle $\alpha$. The three different regions are illustrated in Figure 3.2.

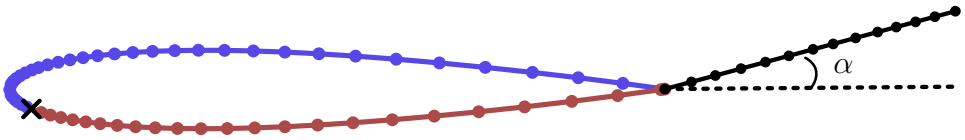


Figure 3.2: Illustration of the three viscous mesh regions.

The space discretization aims to reduce the system (3.49) to a semi-discretized system of the form

$$\frac{\partial \boldsymbol{U}}{\partial t} + \boldsymbol{F}(\boldsymbol{U}) = 0, \tag{3.50}$$

by approximating the spatial derivatives. A first order finite difference scheme was implemented by Dechamps [18] for this purpose. A higher order scheme was not used due to numerical difficulties at the transition point, where the physics changes abruptly from one cell to the other.
Physically, information is propagated downstream by the flow. Therefore, an upwind scheme is most appropriate. The partial derivative of the quantity $u$ with respect to $\xi$ can be written, by a Taylor expansion, as

$$\frac{\partial u}{\partial \xi} = \frac{u_i - u_{i-1}}{\Delta \xi_i} + \mathcal{O}(\Delta \xi_i). \tag{3.51}$$

### 3.2.2 Time integration

When performing numerical time integration, the objective is often to use large time steps to reduce computational cost. However, there are two constraints that limit the size of the allowable time step. The first one, purely numerical in nature, concerns the stability of the considered scheme. Indeed, most integration schemes have a stability condition that needs to be satisfied to ensure convergence. The second constraint is physical. To capture unsteady features, the time step needs to be sufficiently small. Dechamps [18] used a method that is well suited for time marching to steady state. Since unsteadiness is discarded, there is no concern about the physical time step, such that the algorithm can use any time step that allows for convergence. In the present work, there is a need to specifically control the prescribed step; the previous scheme is

therefore not directly applicable and requires a small adaptation that is discussed in section 3.2.2.1

In order to solve the system (3.50), the first-order Taylor expansion of the time derivative is introduced

$$\frac{\partial \boldsymbol{U}}{\partial t} = \frac{\boldsymbol{U}^{n+1} - \boldsymbol{U}^n}{\Delta t} + \mathcal{O}(\Delta t). \tag{3.52}$$

The question is now whether the spatial operator $\boldsymbol{F}(\boldsymbol{U})$ should be evaluated at the old time step $n$ or the new one $n+1$. The first option is the explicit scheme, which requires a low amount of operations per step, but suffers from strict stability conditions often heavily limiting the time step. The second option is known as the implicit scheme, which typically allows for much higher steps, but requires the solution of a non-linear system at each time step, which can be computationally expensive.

Both schemes were considered for the time accurate implementation. It was however found out that the explicit approach was not suitable for the problem. The stability condition was too restrictive, requiring a time step orders of magnitude smaller than the one needed for the implicit scheme such that the gain per iteration is lost by the increased number of required iterations. The implicit scheme is therefore chosen.

In order to solve the nonlinear system required for the implicit scheme, a Newton-like method is used. It relies on the linearization of the system at each iteration through the following Taylor expansion

$$\boldsymbol{F}(\boldsymbol{U}^{n+1}) = \boldsymbol{F}\left(\boldsymbol{U}^n + \Delta \boldsymbol{U}\right) = \boldsymbol{F}(\boldsymbol{U}^n) + \frac{\partial \boldsymbol{F}}{\partial \boldsymbol{U}} \Delta \boldsymbol{U} + \mathcal{O}(\Delta \boldsymbol{U}^2), \tag{3.53}$$

This way, the semi-discretized equation (3.50) becomes

$$\frac{\left(\boldsymbol{U}^n + \Delta \boldsymbol{U}\right) - \boldsymbol{U}^n}{\Delta t} + \boldsymbol{F}\left(\boldsymbol{U}^n\right) + \frac{\partial \boldsymbol{F}}{\partial \boldsymbol{U}} \Delta \boldsymbol{U} = 0. \tag{3.54}$$

After rearranging the terms, the following linear system is obtained

$$\Delta \boldsymbol{U} \left( \frac{\boldsymbol{I}}{\Delta t} + \frac{\partial \boldsymbol{F}}{\partial \boldsymbol{U}} \right) = -\boldsymbol{F}\left(\boldsymbol{U}^n\right). \tag{3.55}$$

The matrix $\dfrac{\partial \boldsymbol{F}}{\partial \boldsymbol{U}}$ is known as the Jacobian of the system, and can be approximated by finite differences by considering a small perturbation $\boldsymbol{\varepsilon}$ in the vector $\boldsymbol{U}$. At the first order, its components are given by

$$\frac{\partial F_i}{\partial U_j} = \frac{F_i(\boldsymbol{U} + \boldsymbol{\varepsilon^j}) - F_i(\boldsymbol{U})}{\varepsilon^j}. \tag{3.56}$$

The evolution of $\boldsymbol{U}$ through the iteration, $\Delta \boldsymbol{U}$, is then obtained by solving the linear system, which is done through its LU decomposition due to its small size.

The Newton method tends to work well under the condition that the solution $\boldsymbol{U}^n$ is close to $\boldsymbol{U}^{n+1}$. In this case, high time steps can be achieved. In other cases, smaller steps may be required to ensure convergence. Through coupling iterations with the inviscid solver, the solver is bound

to encounter such cases. The usage of a constant time step is therefore not appropriate. Indeed, small increments would be required to ensure convergence in the worst cases, while the solver could handle much larger steps in the best cases. The solution to this issue lies in the usage of adaptive time stepping within an inner loop, as implemented by Dechamps [18]. The inner loop time is noted $\tau$ to avoid any confusion with the physical time $t$. The idea is to monitor the convergence of the Newton method and adjust the time step accordingly. This adaptation is based on the residual, corresponding to the imbalance of the system after the Newton iteration. The residual is defined as

$$||\boldsymbol{R}^n|| = ||\frac{\Delta \boldsymbol{U}}{\Delta \tau} + \boldsymbol{F}(\boldsymbol{U}^{n+1})||. \tag{3.57}$$

The time step that is performed locally is computed based on the CFL number

$$\mathrm{CFL} = \frac{a\Delta\tau}{\Delta\xi}, \tag{3.58}$$

where $a = c_s + u_e$ is the advection velocity, with $c_s$ the local speed of sound.

$$c_s = \sqrt{\frac{1}{M_\infty^2} + \frac{\gamma_a - 1}{2}(1 - u_e^2)}, \tag{3.59}$$

where $\gamma_a$ is the ratio of specific heats of the fluid (1.4 for air). If the flow is incompressible, the Mach number in equation (3.59) is replaced by 0.1.

Initially, CFL = 1. The Newton solver gives an increment $\Delta\boldsymbol{U}$, which is used to update the solution. The residual is then computed, and the time step is adjusted according to the following rule

$$\mathrm{CFL}^n = \mathrm{CFL}^0 \left( \frac{||\boldsymbol{R}^0||}{||\boldsymbol{R}^{n-1}||} \right)^{0.7}. \tag{3.60}$$

#### 3.2.2.1 Time stepping for unsteady VII coupling

In order to step in time in a way that is compatible with the unsteady coupling, the solver needs to advance by the same prescribed time step $\Delta t$ for all points. As discussed earlier, the obvious option of directly advancing each point by $\Delta t$ is not suitable since this puts a higher constraint on the time step than necessary. The dual time stepping approach of Dechamps [18] with CFL adaptation is thus kept, but with the stopping criterion is modified; through inner iterations, the stepped time $\tau$ is advanced by $\Delta\tau$ until it reaches $\Delta t$.

It can happen in some cases that a point's integration fails, while the others have converged. In this case, it is given the value of the previous point. This approach is not really consistent with the unsteady philosophy, but improves the stability of the solver for time marching.

### 3.2.3 Boundary and initial conditions

The boundary conditions of the system are given at the stagnation point, which location is provided by the inviscid solver at the first iteration; it is the point of lowest velocity. At this point, the inviscid velocity is directly given by the inviscid solver

$$(u_e)_{\mathrm{visc}} = (u_e)_{\mathrm{inv}}\,. \tag{3.61}$$

Dechamps [18] expressed the values of $\theta$ and $H$ at the stagnation point by following Schlichting and Gersten [48]. The momentum thickness is given by

$$\theta_{\text{stag}} = \sqrt{\frac{0.075}{\text{Re} \left.\dfrac{\mathrm{d}\left(u_e\right)_{\text{inv}}}{\mathrm{d}\xi}\right|_{\xi=0}}}, \tag{3.62}$$

while the shape factor is given a fixed value of

$$H_{\text{stag}} = 2.23. \tag{3.63}$$

If the stagnation point is laminar, *i.e.* transition is not forced at this point, the amplification factor $\tilde{N}_{\text{stag}}$ is set to zero. If transition is forced at the stagnation point, the equations set is turbulent, and the shear stress coefficient $C_{\tau,\text{stag}}$ is zero.

The choice of appropriate initial conditions is also crucial. While their impact is lessened over time, they can have a significant influence on the convergence of the solver. A poorly chosen initial condition can bring unphysical slowly dying transient features, or even lead to a badly conditioned system prone to divergence.

At the first iteration, each point is given the solution at the previous point upstream. This way, information is already propagated downstream at the first iteration.

### 3.2.4 Transition handling

When running the viscous solver, the chance to have the transition location match with a grid point is very low. Most often, the transition will be located between two points. This raises the question of how to handle the transition.

The naive approach of not considering any special treatment for the transition is not suitable. Indeed, this often leads to oscillations in the transition location, which tends to alternate between its two closest points.

The solution to this issue, implemented by Dechamps [18] based on Drela and Giles [22], consists in calculating the actual transition location and computing the solution at the next point by a weighted average between laminar and turbulent solutions. This is more clearly explained by Figure 3.3. Between the two points $i-1$ and $i$, the flow first follows the laminar equations set, and then the turbulent one.

The point $i$ is first solved as if it were fully laminar. The transition location is interpolated between the two points according to the values of the amplification factor $\tilde{N}$ at each point. The point $i$ is then solved as if it were fully turbulent. The two solutions are then averaged, weighted by the transition location.

This method is well suited for steady state problems, but is more difficult to properly adapt when considering the boundary layer as unsteady. It would require keeping track of the laminar and turbulent solutions through time steps, which is not straightforward when transition moves. This

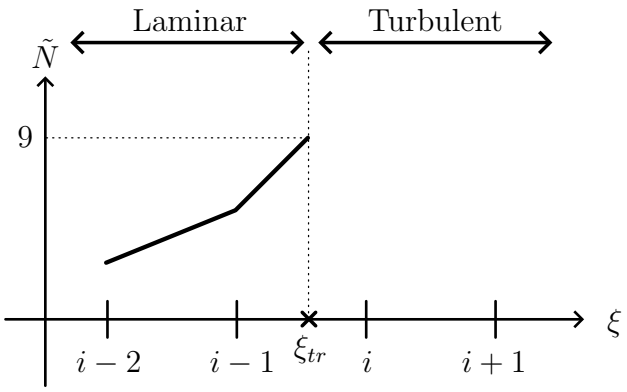


Figure 3.3: Transition laminar and turbulent regions. Adapted from [22].

also risks posing numerical issues as the flow is given a shear stress coefficient initial condition which is not physically consistent when it becomes turbulent. It was thus chosen to treat the transition like in the steady case. The turbulent solution at point $i$ is always calculated to its steady state. If the point $i$ was laminar at the previous iteration, it only steps once, and the transition is averaged. If the point was turbulent, it is reset to laminar and solved to its steady state as such then averaged with the steady turbulent solution.
This approach is quite artificial in its nature, but does work well for the present problem. However, its limitations should be kept in mind. Especially for true unsteady problems, the transition handling should be revisited.

# 4 Viscous-inviscid coupling

In the previous sections, both the viscous and inviscid problems were introduced separately. In order to obtain a solution for the complete flow, there is now a need to conciliate both regions. Due to the complex nature of the problem, both regions are strongly coupled. As a result, it is not trivial to define a fast, accurate and robust interaction scheme. In this section, the basic principles of VII are first recalled. Then, the main interaction schemes are presented and their strengths and weaknesses are highlighted.

The main focus of this work is on the actual implementation of the iterations loop between the viscous and inviscid solvers to attain convergence. The different methods are presented and discussed.

Finally, the topic of unsteady coupling is also briefly mentioned.

## 4.1 Principles

In order to communicate, the viscous and inviscid solvers need to exchange information. The transmission from the inviscid to viscous solver is done through the inviscid edge velocity $u_e$, which is required in the viscous solver. In the other direction, the viscous solver can provide the displacement thickness $\delta^*$ to the inviscid solver; to explain why, a physical argument is given here.

In the boundary layer, the tangential velocity at the wall is zero, and grows progressively as $u = u(\eta)$ to a value $u_e$ at the edge of the boundary layer, defined to be at a distance $\delta$ from the wall. The velocity deficit due to the no-slip condition is then $\Delta u(\eta) = u_e - u(\eta)$. In inviscid flow, the no-slip condition is not present, such that the velocity at the wall is already $u_e$. The displacement thickness $\delta^*$, previously introduced in section 3.1.2, corresponds to the height that contains the integrated effect of $\Delta u(\eta)$ in the inviscid flow. This is more clearly illustrated in Figure 4.1.

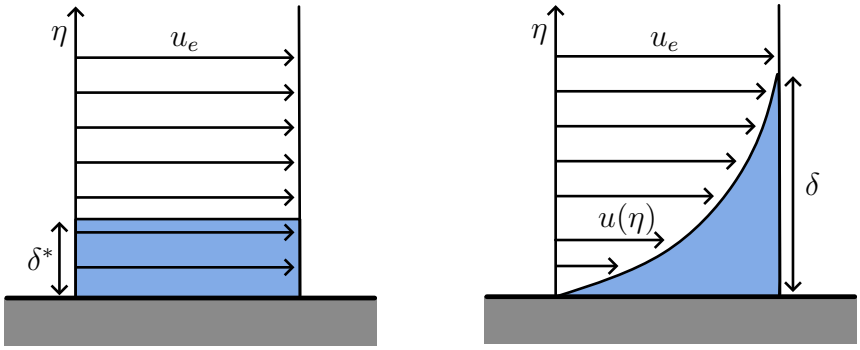


Figure 4.1: Illustration of the displacement thickness. The blue areas are equal. Adapted from [29].

The displacement thickness does in fact correspond to the displacement of the inviscid streamlines to account for the presence of the boundary layer. The airfoil geometry can thus be artificially thickened by $\delta^*$ in the inviscid solver. After solving for the invscid flow, the tangent velocity obtained at the wall is then $u_e$, which is required for the viscous solver (3.10b). Thus, the invscid solver requires the displacement thickness $\delta^*$ from the viscous solver, and the viscous solver requires the velocity at the wall $u_e$ from the inviscid solver.

The usage of the displacement thickness is however not optimal. Indeed, it requires remeshing the inviscid grid at each iteration, which can be computationally expensive. Fortunately, Lighthill [37] proposed the concept of *blowing velocity*, which allows solving for the inviscid flow on the original geometry. Lighthill's blowing velocity was derived for a steady incompressible flow, but can easily be extended to unsteady and compressible cases, as done by Bartels [3]. Starting from the y-momentum at distance $\eta$ (larger than the boundary layer thickness $\delta$) from the wall

$$\rho v = \int_0^\eta \frac{\partial (\rho v)}{\partial \eta} \, \mathrm{d}\eta, \tag{4.1}$$

where the right-hand side can be rewritten using the continuity equation (2.1a)

$$\rho v = -\int_0^\eta \left( \frac{\partial (\rho u)}{\partial \xi} + \frac{\partial \rho}{\partial t} \right) \mathrm{d}\eta. \tag{4.2}$$

Inviscid contributions are now added and removed to equation (4.2) to obtain

$$\rho v = -\int_0^\eta \left( \frac{\partial (\rho_e u_e)}{\partial \xi} + \frac{\partial \rho_e}{\partial t} \right) \mathrm{d}\eta + \int_0^\eta \frac{\partial (\rho_e u_e - \rho u)}{\partial \xi} \, \mathrm{d}\eta + \int_0^\eta \frac{\partial (\rho_e - \rho)}{\partial t} \, \mathrm{d}\eta, \tag{4.3}$$

Since $u_e$ and $\rho_e$ are constant through the boundary layer, the first term on the right-hand side of equation (4.3) is integrated to

$$-\eta \left( \frac{\partial (\rho_e u_e)}{\partial \xi} + \frac{\partial \rho_e}{\partial t} \right). \tag{4.4}$$

The second term can be written, as $\eta$ is larger than $\delta$ and $u = u_e$ outside the boundary layer,

$$\int_0^\delta \frac{\partial \left( \rho_e u_e \left[ 1 - \dfrac{\rho u}{\rho_e u_e} \right] \right)}{\partial \xi} \, \mathrm{d}\eta. \tag{4.5}$$

Again, since $u_e$ and $\rho_e$ are constant through the boundary layer thickness, equation (4.5) becomes

$$\frac{\partial}{\partial \xi} \left( \rho_e u_e \int_0^\delta \left[ 1 - \frac{\rho u}{\rho_e u_e} \right] \, \mathrm{d}\eta \right) \equiv \frac{\partial}{\partial \xi} \left( \rho_e u_e \delta^* \right). \tag{4.6}$$

Similarly, the third term of the right-hand side of equation (4.3) can be written

$$\frac{\partial}{\partial t} \left( \rho_e \int_0^\delta \left[ 1 - \frac{\rho}{\rho_e} \right] \, \mathrm{d}\eta \right) \equiv \frac{\partial}{\partial t} \left( \rho_e \delta^R \right), \tag{4.7}$$

where $\delta^R$ is the *second density thickness* that vanishes for incompressible flows.

Putting everything together, equation (4.3) becomes

$$\rho v = -\eta \left( \frac{\partial (\rho_e u_e)}{\partial \xi} + \frac{\partial \rho_e}{\partial t} \right) + \frac{\partial}{\partial \xi} \left( \rho_e u_e \delta^* \right) + \frac{\partial}{\partial t} \left( \rho_e \delta^R \right). \tag{4.8}$$

The normal velocity at the wall can be obtained, on the scale of the inviscid flow, by evaluating this expression at $\eta = 0$. The blowing velocity is then defined as

$$V^{bl} = \frac{1}{\rho_e}\frac{\partial}{\partial \xi}\left(\rho_e u_e \delta^*\right) + \frac{1}{\rho_e}\frac{\partial}{\partial t}\left(\rho_e \delta^R\right). \tag{4.9}$$

For steady or incompressible cases, the blowing velocity simplifies to

$$V^{bl} = \frac{1}{\rho_e}\frac{\partial}{\partial \xi}\left(\rho_e u_e \delta^*\right). \tag{4.10}$$

By applying this velocity at the wall instead of the non-penetration condition for the inviscid solver, the boundary layer is accounted for without the need for remeshing.

## 4.2 Adaptations to the panel method

The introduction of the blowing velocity in the inviscid solver requires a slight modification of the panel methods. The non-penetration condition is no longer true, and the blowing velocity appears as an additional term in $\boldsymbol{b}^s$ (2.13) in the HSPM method and in $\boldsymbol{c}^u$ (2.24) for the UPM method.

Unfortunately, the presently implemented panel methods coupled with the viscous solver suffer from divergence issues when the Kutta condition and the edge velocity calculations are applied at the wall. Following Cebeci *et al.* [13], these operations are thus performed at a distance $\delta^*$ from the wall. This reduces the gain obtained by the blowing velocity, as new influence coefficients need to be computed at each iteration. The locations of the calculations are illustrated in Figure 4.2.

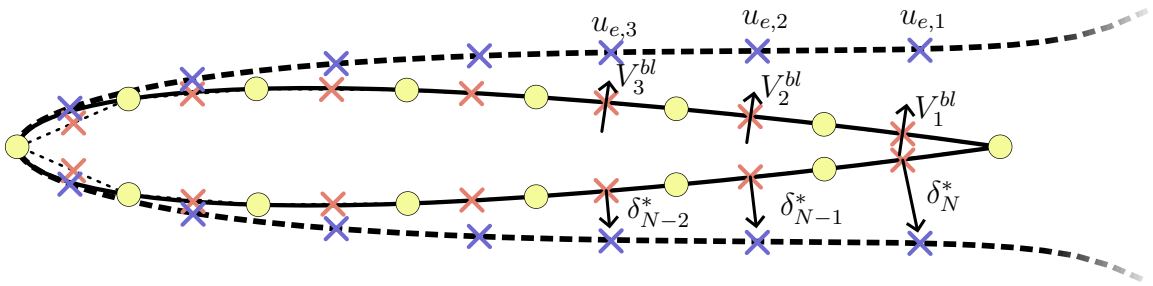


Figure 4.2: Illustration of the calculations locations for the panel methods when coupled with the viscous solver. The blowing velocities $V_i^{bl}$ are imposed on the airfoil control points (orange crosses), while the edge velocities $u_{e,i}$ and Kutta condition are calculated at a distance $\delta_i^*$ from the wall (at the blue crosses).

## 4.3 Interaction schemes

In VII, interaction schemes are different methods to share information between the viscous and inviscid solvers. The choice of an interaction scheme has great implications on the stability and convergence rate of the method.

Interaction schemes can be divided in two categories: *weak* or *strong* coupling. While weak coupling assumes a hierarchy between the two solvers, strong coupling considers both solvers together.

### 4.3.1 Functional approach

In order to describe the behavior and eventual singularities of the different interaction methods, the functional approach introduced by Brune *et al.* [7] provides convenient notations.

The inviscid and viscous operators, respectively $\mathcal{E}$ and $\mathcal{B}$, are defined such that

$$\begin{cases} u_e = \mathcal{E}(\delta^*), \\ \delta^* = \mathcal{B}^{-1}(u_e). \end{cases} \tag{4.11}$$

These operators can be schematically represented for attached, separating and separated flows as in Figure 4.3.

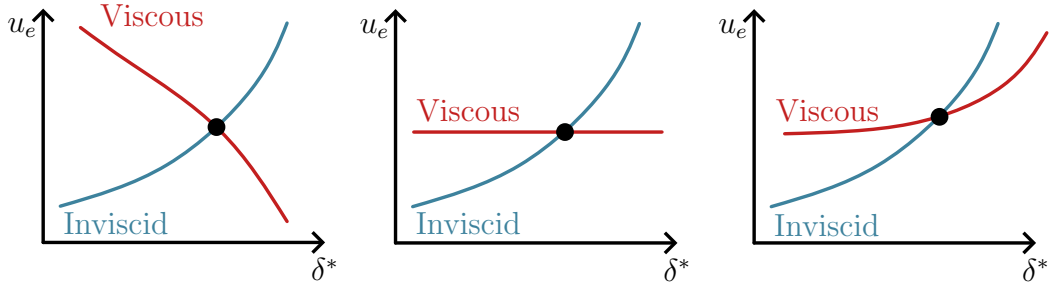


Figure 4.3: Illustration of the viscous and inviscid flow operators. Adapted from [64].

### 4.3.2 Direct coupling

The direct coupling method is the naive approach to VII. The inviscid solver first calculates $u_e$ from the previous displacement thickness, then the viscous solver calculates the new displacement thickness from $u_e$. This cycle goes on until convergence is reached. It can be written as

$$\begin{cases} u_e^n = \mathcal{E}(\delta^{*^{n-1}}), \\ \delta^{*^n} = \mathcal{B}^{-1}\left(u_e^n\right). \end{cases} \tag{4.12}$$

As discussed by Dechamps [18], this method has a singularity when $\mathcal{B}$ is singular. This issue is called the Goldstein [26] singularity, and was shown by Veldman [57] to happen at the separation point.

The Goldstein singularity is caused by the weak coupling of the direct method. The assumed hierarchy between inviscid and viscous regions is no longer valid at the separation point. This can be illustrated with the graphical representation of the flow operators as shown in Figure 4.4.

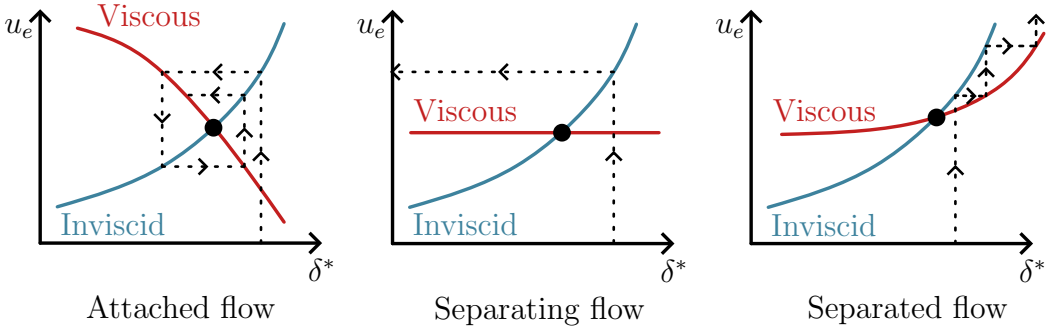


Figure 4.4: Illustration of the direct method's issues with the flow operators. Adapted from [64].

### 4.3.3 Inverse coupling

The inverse method, first introduced by Catherall and Mangler [9], allows to avoid the Goldstein singularity beyond separation by inverting the problem. The inviscid edge velocity is given as a boundary condition to the inviscid solver which then calculates the displacement thickness. $\delta^*$ is then fed to the viscous solver to improve the edge velocity estimation. This strategy is noted

$$\begin{cases} \delta^{*^n} = \mathcal{E}^{-1}(u_e^{n-1}), \\ u_e^n = \mathcal{B}\left(\delta^{*^n}\right). \end{cases} \tag{4.13}$$

Schematically, the inverse method can be represented as in Figure 4.5.

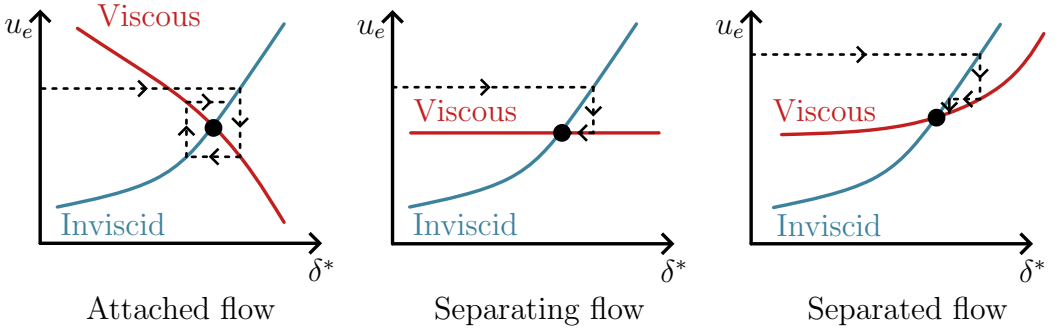


Figure 4.5: Illustration of the inverse method with the flow operators. Adapted from [64].

Even though it seems to fix all the issues of the direct method, the inverse method is not perfect either. Most obviously, it requires the inversion of the inviscid solver, which is not an easy task. Furthermore, the inverse method still assumes a hierarchy between solvers which results, as pointed out by Dechamps [18], in a slow convergence with the need for under-relaxation.

Note the existence of the *semi-inverse* method, which is a hybrid between the direct and inverse methods allowing for a strong coupling between both solvers without requiring the inversion of the inviscid operator. It is not further discussed here, but is for instance mentioned by Le Balleur [36], Carter [8] or Kwon and Pletcher [35].

### 4.3.4 Fully-simultaneous coupling

The fully-simultaneous coupling, unlike the previous methods, does not solve each region separately. Instead, the inviscid and viscous equations are solved together such that no hierarchy is assumed. It can be written

$$\begin{cases} u_e^n = \mathcal{E}(\delta^{*^n}), \\ u_e^n = \mathcal{B}(\delta^{*^n}), \end{cases} \tag{4.14}$$

or, equivalently,

$$(\mathcal{E} - \mathcal{B})\delta^{*^n} = 0. \tag{4.15}$$

As mentioned by Dechamps [18], this method makes the resultant system of equations quite complex and computationally expensive. Furthermore, the convergence of the method is not guaranteed as a singularity can still occur. Nonetheless, this approach has been taken by several authors such as Drela [20] or Epureanu *et al.* [23].

### 4.3.5 Quasi-simultaneous coupling

The quasi-simultaneous method developed by Veldman [58, 59] based on the triple-deck theory [38, 51] allows to conciliate both regions without requiring the expensive system of equations of the fully-simultaneous method.

The viscous solver is still instantaneously informed of the variations of the inviscid region, but not directly through the inviscid solver. Instead, an approximation of the inviscid solver, or *interaction law* is provided. This interaction law is best chosen as simple as possible to possible; ideally an algebraic relation to simplify the method. By denoting the interaction law operator $\mathcal{I}$, the quasi-simultaneous method can be written

$$\begin{cases} u_e^n - \mathcal{I}(\delta^{*^n}) = \mathcal{E}(\delta^{*^{n-1}}) - \mathcal{I}(\delta^{*^{n-1}}), \\ u_e^n = \mathcal{B}(\delta^{*^n}), \end{cases} \tag{4.16}$$

or, equivalently

$$(\mathcal{I} - \mathcal{B})\delta^{*^n} = (\mathcal{I} - \mathcal{E})\delta^{*^{n-1}}. \tag{4.17}$$

Note that at convergence (for steady cases), $\delta^{*^n} = \delta^{*^{n-1}}$ such that the effect of the interaction law vanishes ((4.17) simplifies to $B = E$). It is only a tool used to speed up convergence.

For the interaction law, Dechamps [18] used the following simple law proposed by Veldman [57]

$$\left(u_e - \frac{4V_\infty}{\pi h}\delta^*\right)^{\text{new}} = \left(u_e - \frac{4V_\infty}{\pi h}\delta^*\right)^{\text{old}}, \tag{4.18}$$

where $h$ is the cell size. In order to solve equation (4.18) alongside the viscous system, Dechamps took its derivative in space and time

$$\left(\frac{\partial u_e}{\partial t} - \frac{4V_\infty}{\pi h}\frac{\partial \delta^*}{\partial t}\right)^{\text{new}} = \left(\frac{\partial u_e}{\partial t} - \frac{4V_\infty}{\pi h}\frac{\partial \delta^*}{\partial t}\right)^{\text{old}}, \tag{4.19}$$

$$\left(\frac{\partial u_e}{\partial \xi} - \frac{4V_\infty}{\pi h}\frac{\partial \delta^*}{\partial \xi}\right)^{\text{new}} = \left(\frac{\partial u_e}{\partial \xi} - \frac{4V_\infty}{\pi h}\frac{\partial \delta^*}{\partial \xi}\right)^{\text{old}}, \tag{4.20}$$

where the superscripts *new* and *old* refer to the current and previous iteration, respectively.

As Dechamps ran the viscous solver until convergence at each iteration, the *old* time derivatives vanished. This is no longer the case in the present work. Adding equations (4.19) and (4.20) together, the interaction law is written

$$\left(\frac{\partial u_e}{\partial t} - \iota\frac{\partial \delta^*}{\partial t}\right)^{\text{new}} + \left(\frac{\partial u_e}{\partial \xi} - \iota\frac{\partial \delta^*}{\partial \xi}\right)^{\text{new}} = \left(\frac{\partial u_e}{\partial t} - \iota\frac{\partial \delta^*}{\partial t}\right)^{\text{old}} + \left(\frac{\partial u_e}{\partial \xi} - \iota\frac{\partial \delta^*}{\partial \xi}\right)^{\text{old}}, \tag{4.21}$$

where $\iota = \dfrac{4V_\infty}{\pi h}$.

Equation (4.21) is then solved alongside the viscous system at each iteration. In order to express the interaction law in terms of the viscous solver's variables, the displacement thickness is replaced by its definition $\delta^* = H\theta$.

The quasi-simultaneous method is schematically represented in Figure 4.6.

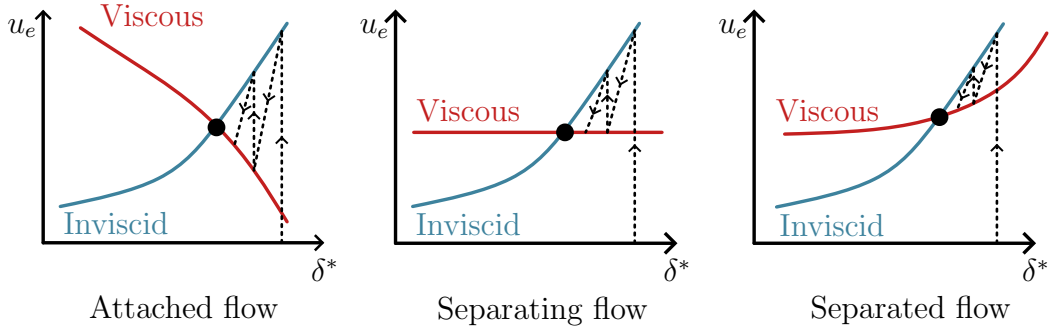


Figure 4.6: Illustration of the quasi-simultaneous coupling method. Adapted from [64].

## 4.4 Coupling for steady cases

There are different methods to iterate between inviscid and viscous solvers to obtain a steady solution. Often, a *steady* coupling (noted $\mathcal{S}$ coupling), where each solver is converged before trading information, is chosen ([18], [21], [59], ...). More recently, Ozdemir *et al.* [43] used an *unsteady* ($\mathcal{U}$) coupling where each solver only runs one time step per iteration. These two methodologies are represented in Figure 4.7.

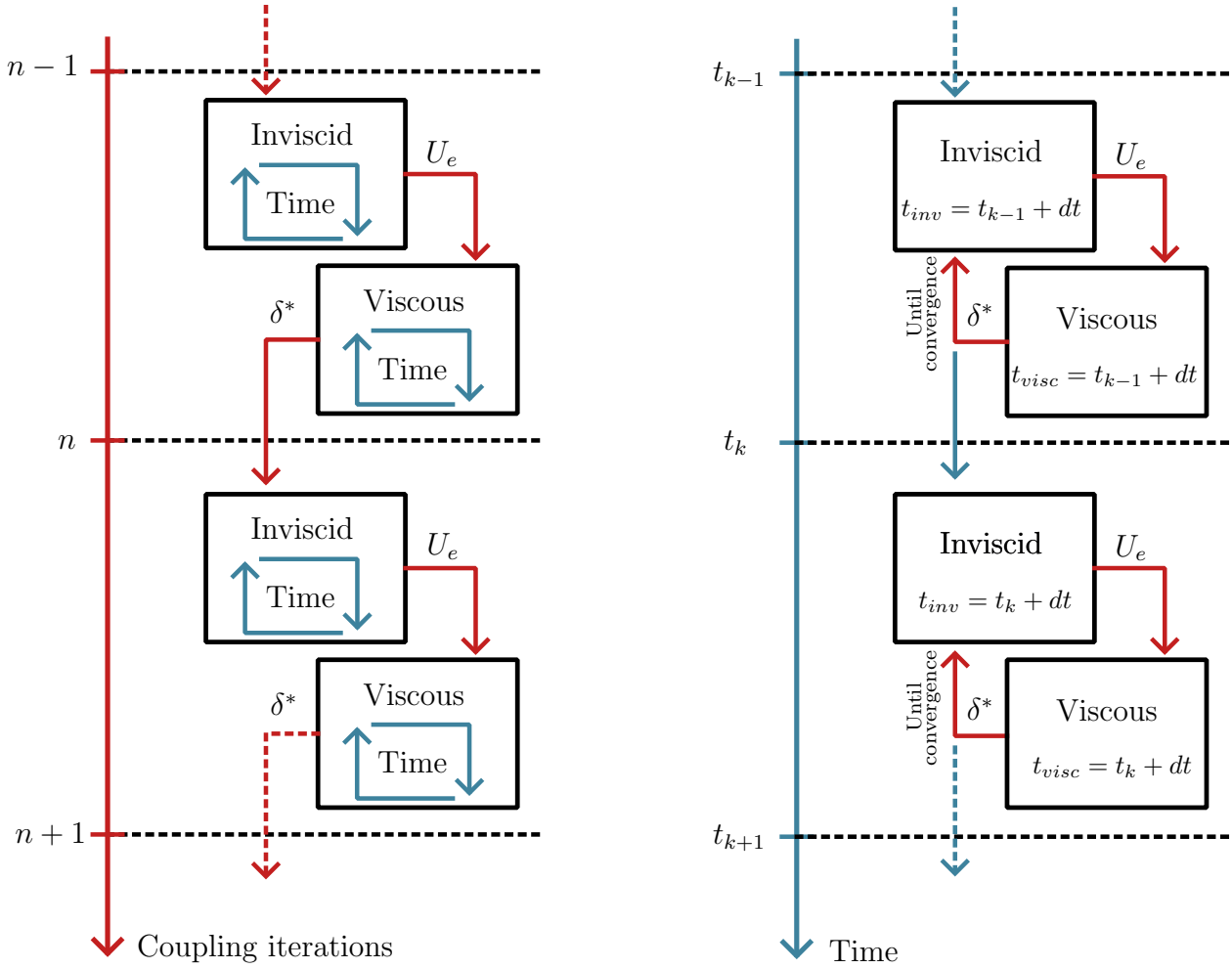


Figure 4.7: Representation of the $\mathcal{S}$ (left) and $\mathcal{U}$ (right) VII coupling strategies.

In the present work, the $\mathcal{U}$ coupling is investigated and compared to its $\mathcal{S}$ counterpart. It is however implemented differently from the one used by Ozdemir *et al.* It was indeed found that converging $\delta^*$ and $u_e$ at each iteration yielded poor results within the current framework. This can be explained by two main reasons.

- By feeding the inviscid solver with the viscous solution at the same time step, the method is no longer consistent with time stepping. Indeed, the inviscid solver's boundary condition is no longer the one at the end of the previous step, but rather the one at the end of the current step. This inconsistency can lead to issues in the convergence of the method.
- At the start of the coupling iterations, the assumed solution is far away from the final steady flow. In order to attain this solution, both solvers have to pass unphysical transient states. These states can be quite disadvantageous, and see disturbances appear. These disturbances should be dissipated in time, but by having a feedback loop through the step they can be amplified, leading to divergence.

Overall, this specific approach did not bring any benefit in either stability or speed of the coupling. From this point, the $\mathcal{U}$ coupling thus refers to this method without the inner feedback

loop. It was represented in a simplified way in Figure 1.2.

### 4.4.1 Optimal time step determination

To leverage the $\mathcal{U}$ coupling as much as possible, some thought has to be put into choosing an appropriate time step. It should not be too small, as not to slow down the convergence of the method, requiring more iterations to reach the steady state. On the opposite side of the spectrum, for large time steps, the $\mathcal{U}$ method essentially becomes a slower version of the $\mathcal{S}$ method due to the increased number of operation for the UPM solver as opposed to the HSPM solver.

Unfortunately, there is currently no clear answer to this question. The optimal time step depends on the specific flow case and solver's settings, and is found through trial and error.
Interestingly, choosing different time steps for the inviscid and viscous solvers can lead to better convergence in most cases, which further complicates the decision.

At the first iteration, the inviscid solver initially runs alone. In order to stabilize the method, this iteration is run until convergence to the steady inviscid solution. Otherwise, the viscous solver would initially be fed with bad information in its initial conditions. This could lead to slow convergence or divergence.

### 4.4.2 Wake treatment

Ideally, the wake should be treated in the same manner as the airfoil surface, with viscous and inviscid solvers exchanging information. This is however not trivially done within the UPM method as the wake is made of free vortices rather than panels. Therefore, the interaction in the wake is unilateral; the viscous solver is given the inviscid solution, but the inviscid solver is not directly influenced by the blowing velocity in this region. The viscous wake geometry is given by a straight line inclined at the angle of attack going from to trailing edge to 5 chord lengths downstream, as was shown in Figure 3.2.

This simplification in the interaction is likely to cause disagreements between the present method and other VII solvers. Indeed, Cebeci and Jang [11] showed a significant influence of the viscous wake on the lift coefficient at least for quasi-steady cases.

### 4.4.3 Convergence criterion

In order to assess the convergence of the VII coupling, Dechamps [18] studied the evolution of the drag coefficient, computed at the last wake point. This criterion was a good indicator of convergence due to the downstream marching and the fact that the whole boundary layer was recomputed at each iteration.

In the present work, as points keep their solution through coupling iterations, it is no longer pertinent to use a locally computed quantity. Rather, the evolution of the displacement thickness

along the whole airfoil is monitored, and the error is computed as

$$\text{Error}^n = \frac{||\boldsymbol{\delta^*}^n|| - ||\boldsymbol{\delta^*}^{n-1}||}{||\boldsymbol{\delta^*}^n||}. \tag{4.22}$$

## 4.5 Coupling for unsteady motion

### 4.5.1 Fundamental changes

The topic of coupling for unsteady boundary layers is more complex than its steady counterpart. The first difference, as already mentioned, concerns the definition of the blowing velocity

$$V^{bl} = \frac{1}{\rho_e}\frac{\partial}{\partial \xi}\left(\rho_e u_e \delta^*\right) + \frac{1}{\rho_e}\frac{\partial}{\partial t}\left(\rho_e \delta^R\right). \tag{4.23}$$

This change is not really problematic as it only requires the addition of a term in the blowing velocity calculation.

A more serious issue involves the interaction law that is used. It was said above that it can be used because it does vanish at steady state, since ${\delta^*}^n = {\delta^*}^{n-1}$. This is however no longer true for unsteady cases, as the boundary layer constantly evolves. As pointed out by Haciahmetoglu [29], the interaction law pollutes the solution, including its approximated physics in the calculated flow. There are two solutions to this issue.

The first solution is to refrain from using the quasi-simultaneous method and rather consider other interaction methods which avoid the use of the interaction law.

The second option is to perform *sufficiently small* time steps, such that the solution does not vary much between each iteration. This way, the interaction law which is a linearized version of the inviscid equations does numerically make sense. To the author's knowledge, this approach has not yet been taken to simulate unsteady motion.

### 4.5.2 Stagnation point movement

For steady coupling problems, Dechamps [18] discussed the issue of stagnation point movement. Indeed, the stagnation point of the inviscid solution does not necessarily align with the one of the viscous solution especially at high angles of attack. This lead to a small discontinuity in the solution at the stagnation point if not taken into account. However, this issue was not considered to be critical as the inviscid and viscous stagnation locations only varied by at most a few cells, and the alternative of allowing for stagnation point movement in the viscous solver caused oscillations that prevented convergence.

When considering airfoil pitching however, the stagnation point movement can become significant and introduce large discontinuities if not taken into account. An attempt was made to allow for stagnation point movement in the viscous solver. However, all the points between the previous and current stagnation points became badly conditioned and the only solution to reach convergence was to impose initial conditions to these points. This is not a satisfactory solution

as it breaks the time consistency of the method. It was thus chosen to keep the stagnation point fixed in the viscous solver, and to accept the discontinuity in the solution.

# 5 Applications

This section presents a few applications of the methods discussed in the previous sections.

First, steady flows are considered. The panel methods are validated on inviscid flows in section 5.1, and then coupled with the viscous solver to study the steady ($\mathcal{S}$) and unsteady ($\mathcal{U}$) coupling strategies in details in section 5.2.

Unsteady flows are then considered. The UPM method is validated in section 5.3 for a starting flow and a pitching airfoil at different frequencies. The viscous coupling is then applied to simple pitching cases in section 5.4.

## 5.1 Inviscid steady flow

The HSPM and UPM methods are compared to XFOIL for the inviscid flow around an airfoil at different angles of attack. The meshing process is first described, followed by the results for the NACA0012 airfoil.

### 5.1.1 Mesh

Generating meshes for the panel methods without viscous interaction is a straightforward process; the method has little chance of diverging if one region is too fine or too coarse. In order to obtain a mesh independent solution with minimal cost, the grid is finer near the trailing and leading edges of the airfoil, whereas it is coarser in the middle, where velocity gradients are smaller. To obtain this mesh, a distribution of $N+1$ angles $\kappa_i$ from 0 to $2\pi$ is generated. The $x$ coordinates of the mesh points are then given by

$$x_i = \frac{c}{2}\left(1 + \cos\left(\kappa_i\right)\right). \tag{5.1}$$

This results in meshes such as the one pictured in Figure 5.1.

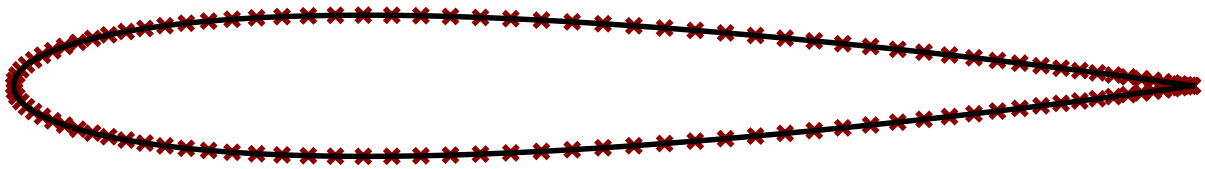

Figure 5.1: Point distribution on a cosine mesh.

A typical convergence analysis on the cosine mesh is shown in Figure 5.2.

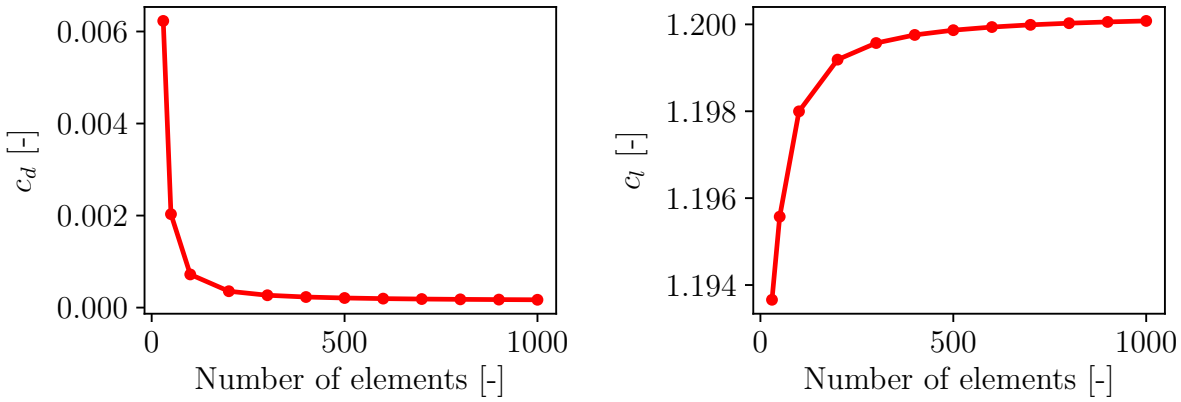


(a) Drag coefficient.

(b) Lift coefficient.

Figure 5.2: Convergence analysis of the UPM method for a cosine mesh (NACA0012 at 10° angle of attack).

As expected, Figure 5.2a shows the d'Alembert paradox: the drag coefficient tends to zero as the mesh is refined. The lift coefficient, on the other hand, converges to a finite value, as shown in Figure 5.2b.

### 5.1.2 NACA0012

The NACA0012 airfoil is simulated at three angles of attack of 2, 6 and 10°. The HSPM and UPM methods are run on the same mesh, which has been sufficiently refined to ensure that the mesh independent solution is obtained ($N = 1000$ points). The XFOIL results are obtained on a mesh with $N = 364$ points being the software's hard limit.

The pressure coefficient ($C_p$) distribution on the airfoil is shown in Figure 5.3 for the present methods and XFOIL. Data from viscous experiments of Gregory and O'Reilly [28] on the top surface of the airfoil are also shown ($M_\infty = 0.16$, $\mathrm{Re} = 2.88 \times 10^6$, free transition) for reference. The three codes are in good agreement, even near the leading edge at the stagnation point and the point of minimal pressure. As can be seen in Figures 5.3b and 5.3c, the inviscid panel methods tend to overestimate the suction peak near the leading edge compared to experiments, especially at high angles of attack.

The lift coefficient results of the three codes are summarized in Table 5.1.

| | 2° | 6° | 10° |
|---|---|---|---|
| UPM | 0.2410 | 0.7222 | 1.200 |
| HSPM | 0.2413 | 0.7229 | 1.201 |
| XFOIL | 0.2417 | 0.7239 | 1.203 |

Table 5.1: Inviscid lift coefficient for a NACA0012 airfoil at different angles of attack for the UPM, HSPM and XFOIL codes.

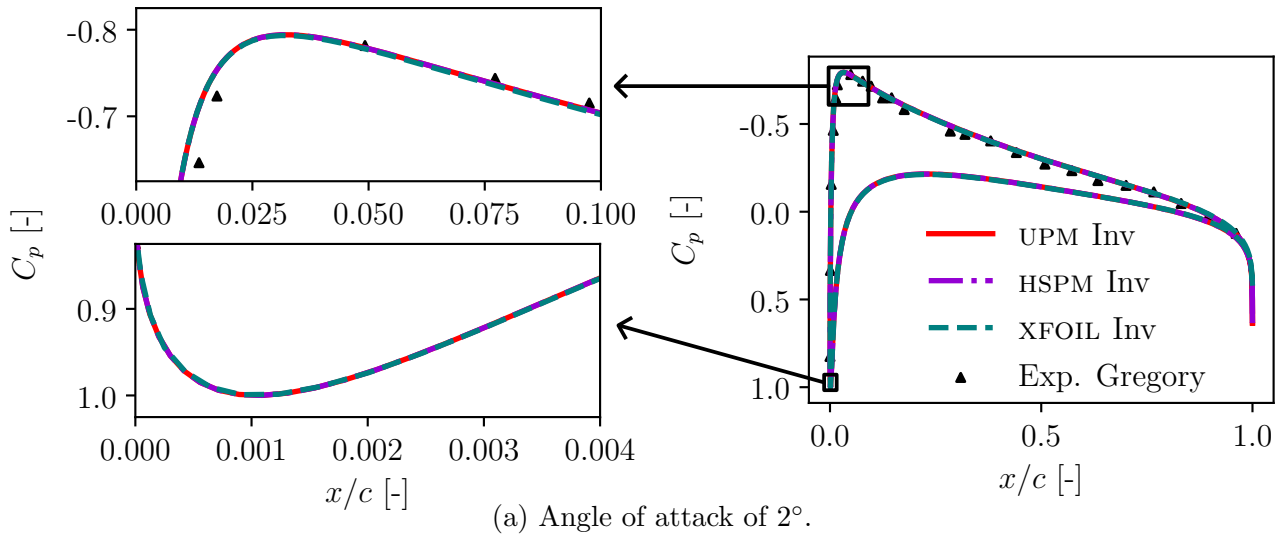


(a) Angle of attack of 2°.

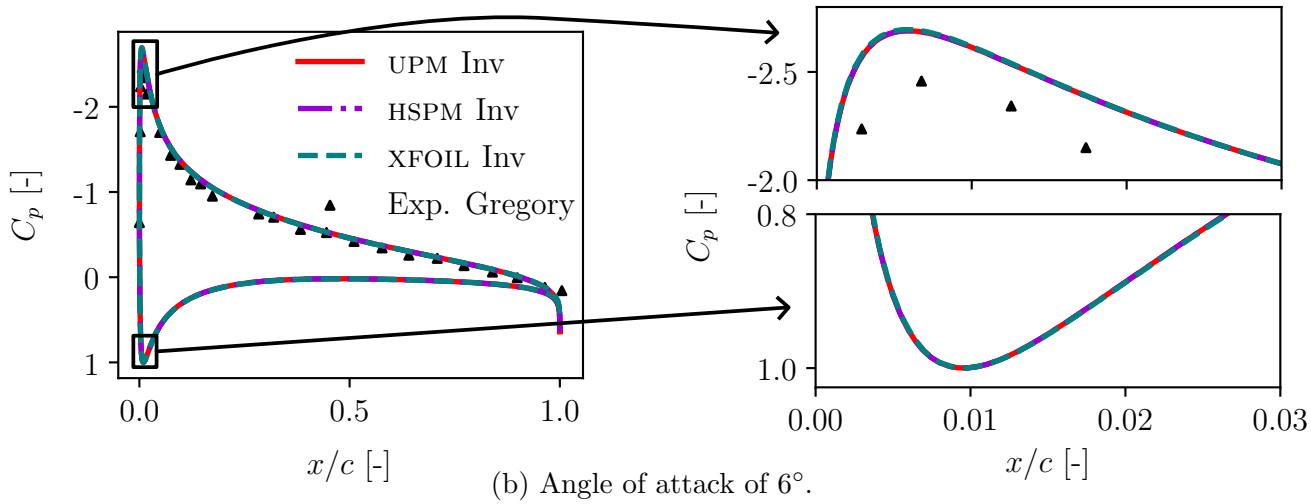


(b) Angle of attack of 6°.

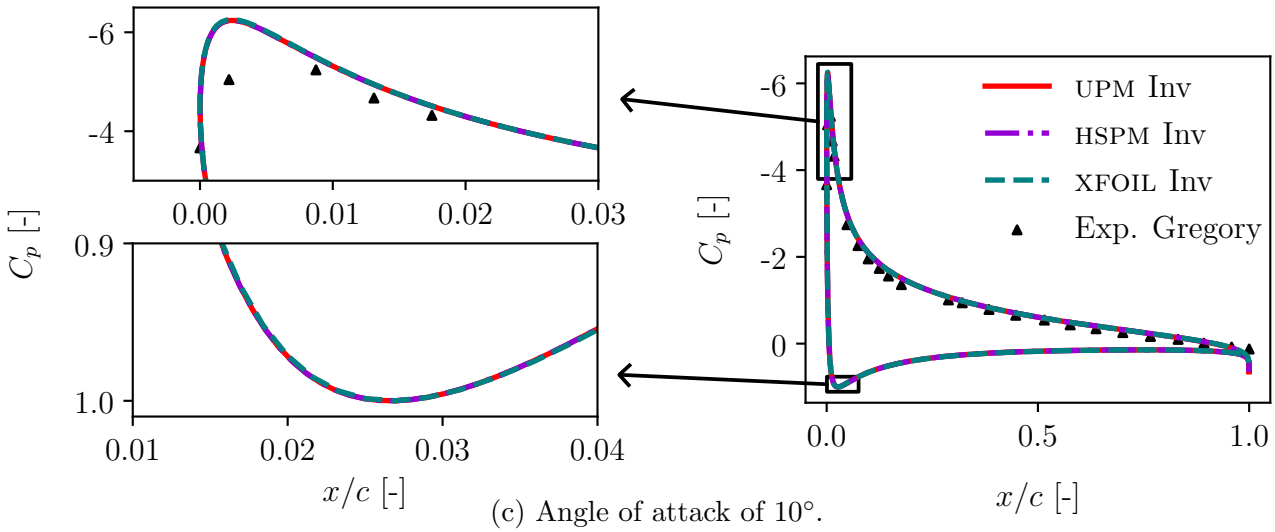


(c) Angle of attack of 10°.

Figure 5.3: Inviscid pressure coefficient for a NACA0012 airfoil at 2, 6 and 10° angle of attack. XFOIL, HSPM and UPM results, zoom near the leading edge. Gregory's [28] viscous experimental data for comparison ($M_\infty = 0.16$, $\mathrm{Re} = 2.88 \times 10^6$, free transition).

The only noticeable difference between the present codes and XFOIL is the point of stagnation at the trailing edge. This discrepancy is not due to a difference between the methods, but rather to the fact that the refinement of the mesh is not the same. For infinitely small cells near the trailing edge, the Kutta condition results in zero velocity *i.e.* a pressure coefficient of one. This result may appear as insignificant for inviscid flows, but it can have great ramifications when viscous interaction is taken into account. Indeed, this drop in velocity can cause numerical issues in the coupling and put a lower bound on the allowable cell size in the near the trailing edge for convergence.

The lift coefficient results of the different codes are in excellent agreement.

## 5.2 Viscous steady flow

In this section, the "steady" ($\mathcal{S}$) and "unsteady" ($\mathcal{U}$) coupling strategies are compared for steady applications. They are compared based on their speed and stability, as well as their accuracy.

This section first presents the mesh used for viscous applications. Then, various test cases are considered to understand the differences between the two coupling strategies in multiple flow conditions.

All results are compared to XFOIL simulations as well as experimental data when it is available.

### 5.2.1 Mesh

As discussed previously in section 5.1, reusing the same mesh as inviscid simulations for coupled VII simulations is not the best choice. Indeed, the large pressure gradient predicted at the trailing edge causes divergence in the viscous solver. Meshes for viscous cases are thus varied slightly.

The classical cosine mesh is first generated, like before. Rather than refining the mesh near the trailing edge, the element size is kept constant from $x/c = 0.8$ to $x/c = 1$. This kind of mesh is shown in Figure 5.4.

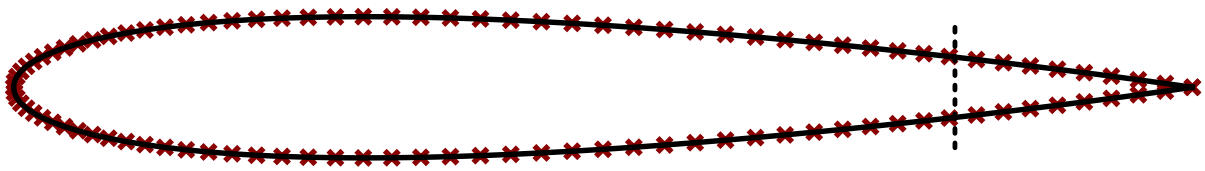

Figure 5.4: Point distribution on the modified cosine mesh. The dashed line shows the location where the cell size is fixed.

The convergence of the coupled VII solver on the modified cosine mesh is shown in Figure 5.5 for a simple attached flow at low incidence.

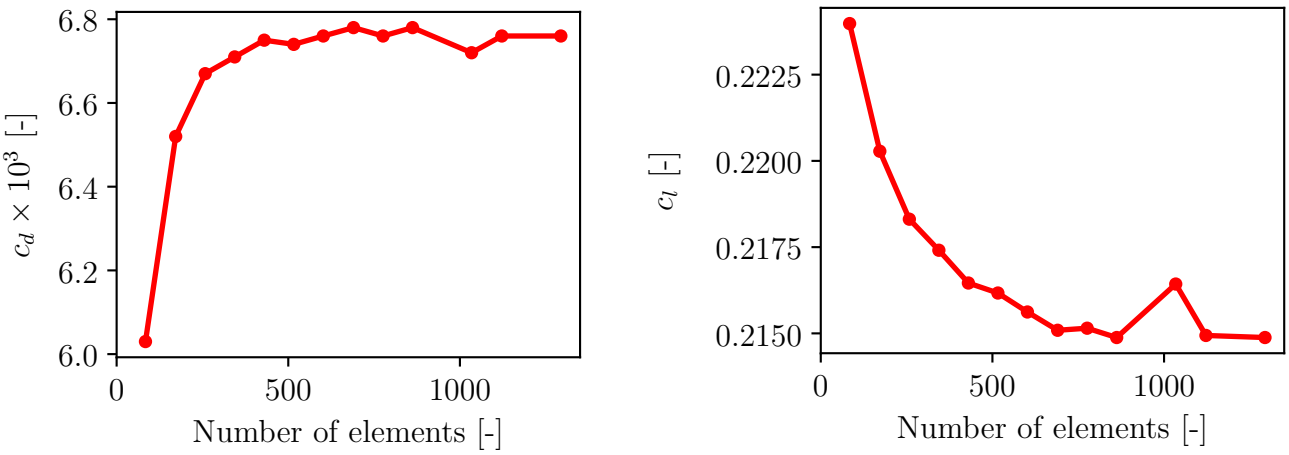


(a) Drag coefficient.

(b) Lift coefficient.

Figure 5.5: Convergence analysis of the UPM method with VII for a modified cosine mesh (NACA0012 at 2° angle of attack, $\mathrm{Re} = 10^7$, $\mathcal{S}$ coupling).

Figure 5.5 shows that the convergence of the coupled method is not as good as for the inviscid case. It is slower and not monotone anymore. In the following applications, a modified cosine mesh with initially 600 points is used. This results in a mesh with $N = 516$ elements.

### 5.2.2 Attached flow at low angle of attack

The first test case is the one of a NACA0012 airfoil at an angle of attack of 2°. The Reynolds number is set to $10^7$. At these conditions, the flow remains attached throughout the chord, allowing to avoid most numerical difficulties.

For the $\mathcal{U}$ strategy, this case runs best with the same time step for the inviscid and viscous solvers; $\Delta t = 2$ seconds.

The coupling iterations are run until the error (4.22) drops below $10^{-4}$ for the two strategies. The convergence of the drag and lift coefficients for both methods is shown in Figure 5.6.

Different observations can be made based on Figure 5.6. In this case, the evolution of lift and drag coefficient through iterations is monotone and quite smooth for both coupling strategies. Both coupling strategies eventually converge to the same solution. However, the $\mathcal{U}$ coupling strategy attains convergence with slightly fewer iterations (27 compared to 31).

In simple cases such as this one, both coupling strategies essentially perform the same. For slightly different conditions, the $\mathcal{S}$ coupling strategy could have been more advantageous.

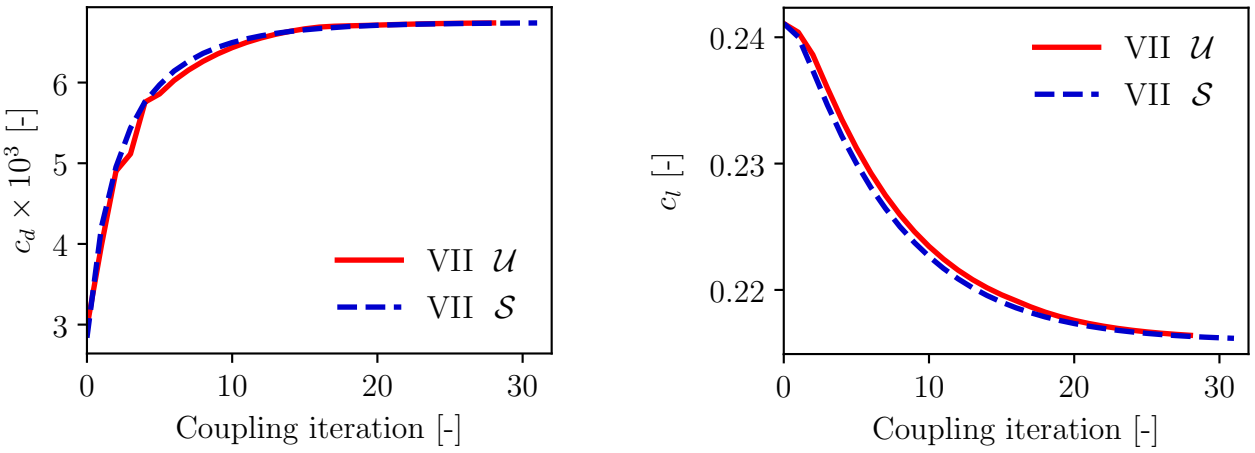


(a) Drag coefficient.

(b) Lift coefficient.

Figure 5.6: Comparison of the $\mathcal{S}$ and $\mathcal{U}$ coupling strategies for the lift and drag coefficients evolution through coupling iterations of a NACA0012 airfoil at 2° angle of attack and $\mathrm{Re} = 10^7$.

Since the iteration cost of the $\mathcal{U}$ coupling is higher than the one of the $\mathcal{S}$ coupling due to the nonlinearity of the UPM method, the slight iteration gain is just enough to break even. Both methods required 1.3 seconds to converge.

The pressure coefficient $C_p$, skin friction coefficient $c_f$, shape factor $H$ and displacement thickness $\delta^*$ resulting from the VII coupling are shown in Figure 5.7. Note that the $\mathcal{U}$ and $\mathcal{S}$ coupling strategies results are extremely close and indistinguishable. All the quantities are compared to XFOIL, and the inviscid pressure coefficient is also shown. The different results are in good agreement, with a slight discrepancy at the trailing edge for the pressure coefficient and lower peaks in the skin friction. The results of the different codes are summarized in Table 5.2.

| | $c_l$ [-] | $c_d \times 10^3$ [-] | $x_{tr_{top}}/c$ [-] | $x_{tr_{bottom}}/c$ [-] | $N_{it}$ [-] | Execution time [s] |
|---|---|---|---|---|---|---|
| UPM Inviscid | 0.2411 | - | - | - | - | - |
| VII $\mathcal{U}$ | 0.2165 | 6.74 | 0.1934 | 0.4986 | 27 | 1.3 |
| VII $\mathcal{S}$ | 0.2161 | 6.74 | 0.1935 | 0.4985 | 31 | 1.3 |
| VII XFOIL | 0.2272 | 5.33 | 0.1906 | 0.5018 | - | - |

Table 5.2: Summary of the results for the NACA0012 at 2° angle of attack, $\mathrm{Re} = 10^7$.

The differences in lift coefficient between the present methods and XFOIL are mostly due to small disagreements in the pressure coefficient at the trailing edge. The application of the Kutta condition is likely to be the cause of these discrepancies.

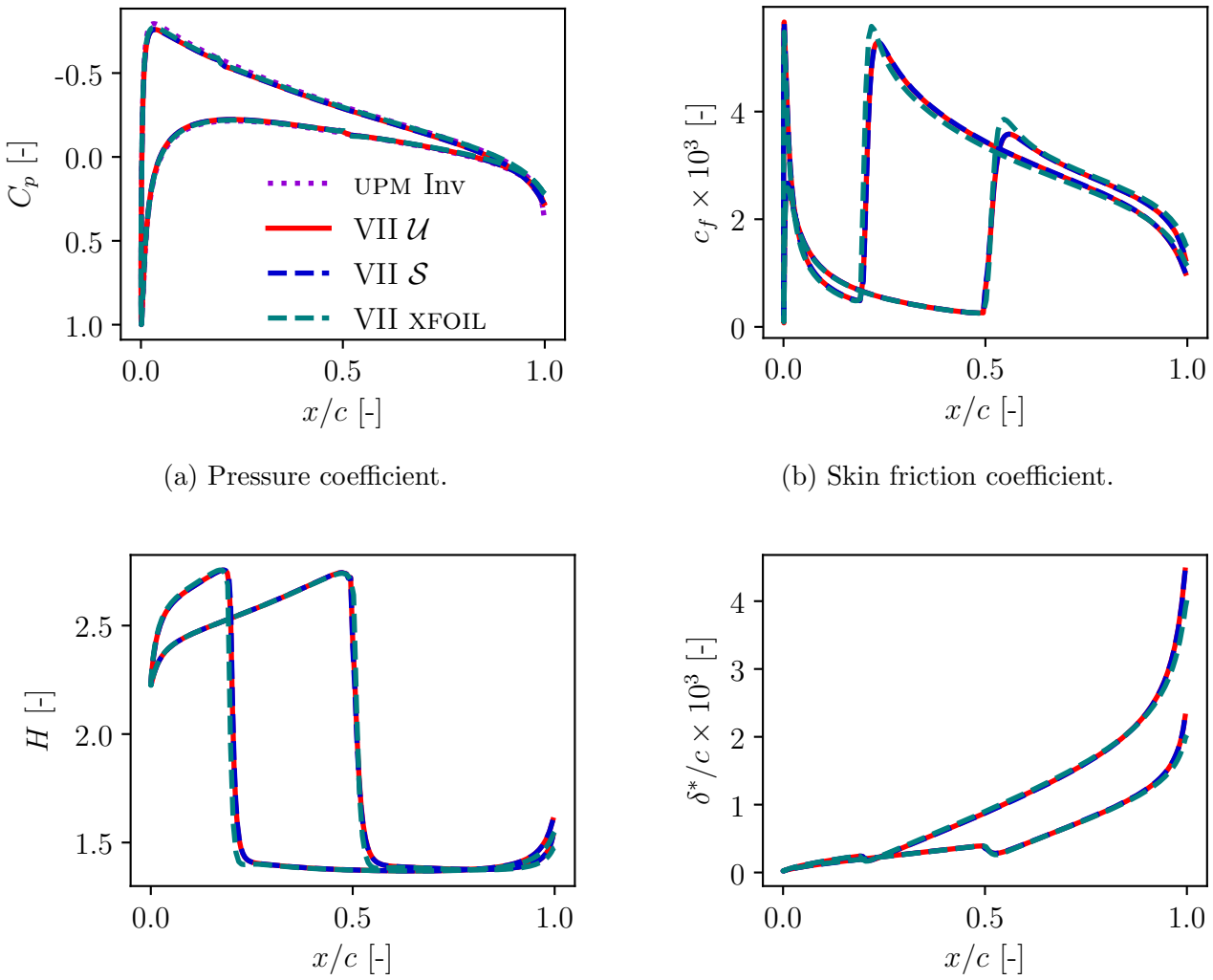


(a) Pressure coefficient.

(b) Skin friction coefficient.

(c) Boundary layer shape factor.

(d) Displacement thickness.

Figure 5.7: Comparison of pressure coefficient, skin friction coefficient, boundary layer shape factor and displacement thickness between the $\mathcal{U}$ and $\mathcal{S}$ coupling strategies and XFOIL for the NACA0012 airfoil at 2° angle of attack and $\mathrm{Re} = 10^7$.

### 5.2.3 Mildly separated flow with forced transition

The second test case is the one of a NACA0012 airfoil at a Reynolds number of $3 \times 10^6$. Two different angles of attack of 10° and 15° are considered. At these conditions, a separation bubble forms on the upper surface of the airfoil. The flow only stays detached on a small portion of the upper surface and does not cause a full stall. This is a good test case to evaluate the capabilities of the coupling strategies to handle separation, which is known to be a difficult task.
The transition is tripped at $x/c = 0.05$ on the lower surface of the airfoil.
For both angles of attack, the $\mathcal{U}$ coupling benefits from the usage of different time steps for the inviscid and viscous solvers. The chosen steps are $\Delta t_{inv} = 2$ seconds and $\Delta t_{visc} = 1$ second.
The experimental pressure coefficient data from Gregory and O'Reilly [28] is used for comparison

with the VII results. The experimental setup is not exactly the same as the one used in the present work; the transition is free and the Reynolds number is slightly different at $2.88 \times 10^6$. The flow is also not totally incompressible, with a Mach number of 0.16.

#### 5.2.3.1 10° angle of attack

The convergence of the drag and lift coefficients for both coupling strategies is shown in Figure 5.8. Both solvers are run for 300 coupling iterations. The iterations where the error gets smaller than $10^{-4}$ are marked by crosses.

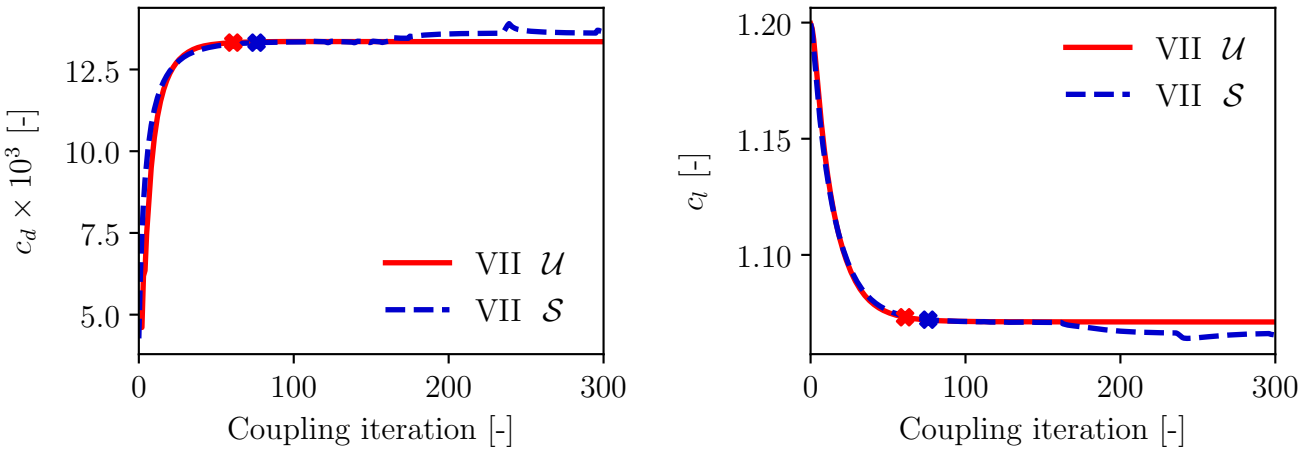


(a) Drag coefficient.

(b) Lift coefficient.

Figure 5.8: Comparison of the $\mathcal{S}$ and $\mathcal{U}$ coupling strategies for the lift and drag coefficients evolution through coupling iterations (NACA0012 at 10° angle of attack, $\mathrm{Re} = 3 \times 10^6$, tripped transition at $x/c = 0.05$). Crosses mark $10^{-4}$ error reached.

One advantage of the $\mathcal{U}$ coupling is observable in Figure 5.8. Even though convergence is initially similar for both coupling strategies, the $\mathcal{U}$ coupling shows a more stable convergence. When run further than $10^{-4}$ error, the $\mathcal{S}$ coupling starts experiencing instabilities in its solution, eventually oscillating around a different equilibrium solution than the initial one.

In order to understand the difference between the two coupling strategies, the pressure coefficient, skin friction coefficient, boundary layer shape factor and displacement thickness are shown in figures 5.9 to 5.12. The "VII $\mathcal{S}$ *alt*" results correspond to the second equilibrium solution reached by the $\mathcal{S}$ coupling strategy (at 230 iterations, with an error of $10^{-5}$). All results are zoomed in near the separation region, where the differences are the most significant.

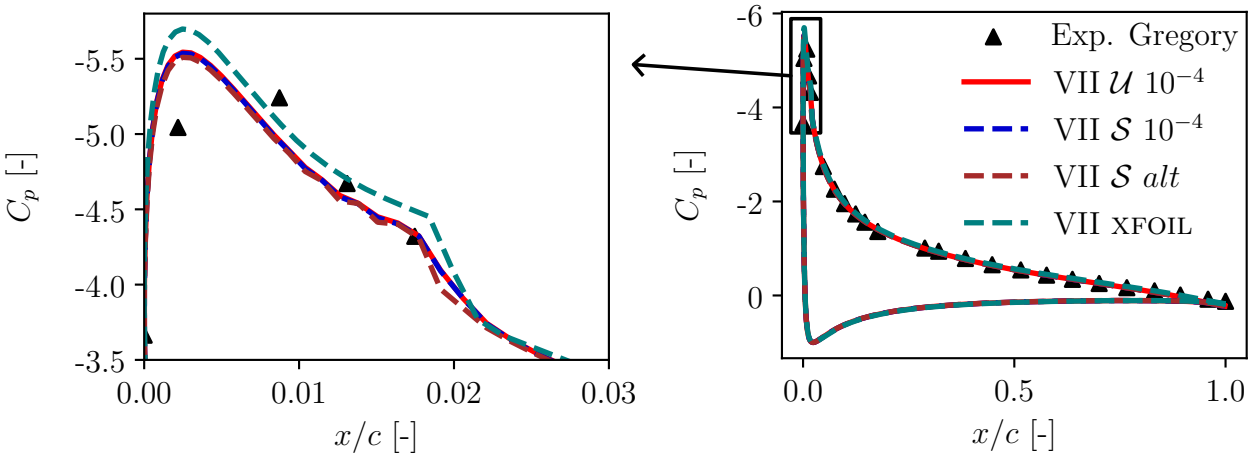


Figure 5.9: Pressure coefficient for the NACA0012 at 10° angle of attack and Re $= 3 \times 10^6$ on the whole surface and near separation for the $\mathcal{U}$ and $\mathcal{S}$ coupling (first and second equilibrium positions). Comparison with XFOIL results and experimental data from Gregory and O'Reilly [28] ($M_\infty = 0.16, \text{Re} = 2.88 \times 10^6$, free transition).

Figure 5.9 shows an overall good agreement between all VII results and the experimental data. When zooming in near the separation region, discrepancies appear visible between the present results and XFOIL as well as the experimental data. The $\mathcal{U}$ and $\mathcal{S}$ coupling strategies at an error of $10^{-4}$ are almost indistinguishable. The second equilibrium solution of the $\mathcal{S}$ coupling strategy, however, shows a slightly different, more oscillatory solution. These trends are also visible in the skin friction coefficient, boundary layer shape factor and displacement thickness, where the oscillations are more pronounced.
The shift in solution for the $\mathcal{S}$ coupling strategy is caused by an instability in the separation region. The usage of an unsteady interaction allows the $\mathcal{U}$ method to dampen these instabilities and keep the solution stable.

The different solutions are summarized in Table 5.3. It can be seen that the second equilibrium position of the $\mathcal{S}$ coupling still gives a reasonable solution for lift and drag. The issue at this flow condition is really the loss of smoothness in the convergence rather than the different solution.

| | $c_l$ [-] | $c_d \times 10^3$ [-] | $x_{tr_{top}}/c$ [-] | $N_{it}$ [-] | Execution time [s] |
|---|---|---|---|---|---|
| UPM Inviscid | 1.1996 | - | - | - | - |
| VII $\mathcal{U}$ $10^{-4}$ | 1.0731 | 13.32 | 0.017 | 61 | 2.8 |
| VII $\mathcal{S}$ $10^{-4}$ | 1.0721 | 13.32 | 0.017 | 76 | 3.1 |
| VII $\mathcal{S}$ *alt* | 1.0664 | 13.61 | 0.0176 | - | - |
| VII XFOIL | 1.1044 | 12.94 | 0.019 | - | - |
| Exp Gregory & O'Reilly[1] [28] | 1.09 | 13.5 | 0.0175 | - | - |

Table 5.3: Summary of the results for the NACA0012 at 10° angle of attack, Re $= 3 \times 10^6$, tripped transition at $x/c = 0.05$. Experimental data of Gregory and O'Reilly [28] at Re $= 2.88 \times 10^6$, $M_\infty = 0.16$ and free transition.

[1]The experimental data has been digitized and may be inaccurate.

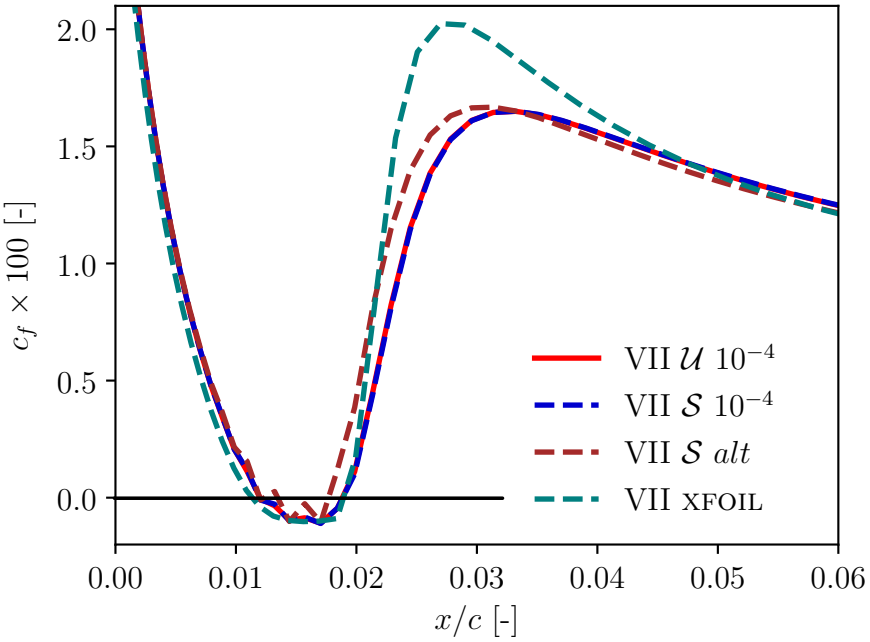


Figure 5.10: Skin friction coefficient near separation for the $\mathcal{U}$ and $\mathcal{S}$ coupling (first and second equilibrium positions). Comparison with XFOIL results. (NACA0012 at 10° angle of attack, $\mathrm{Re} = 3 \times 10^6$). Line at vanishing skin friction to show separation.

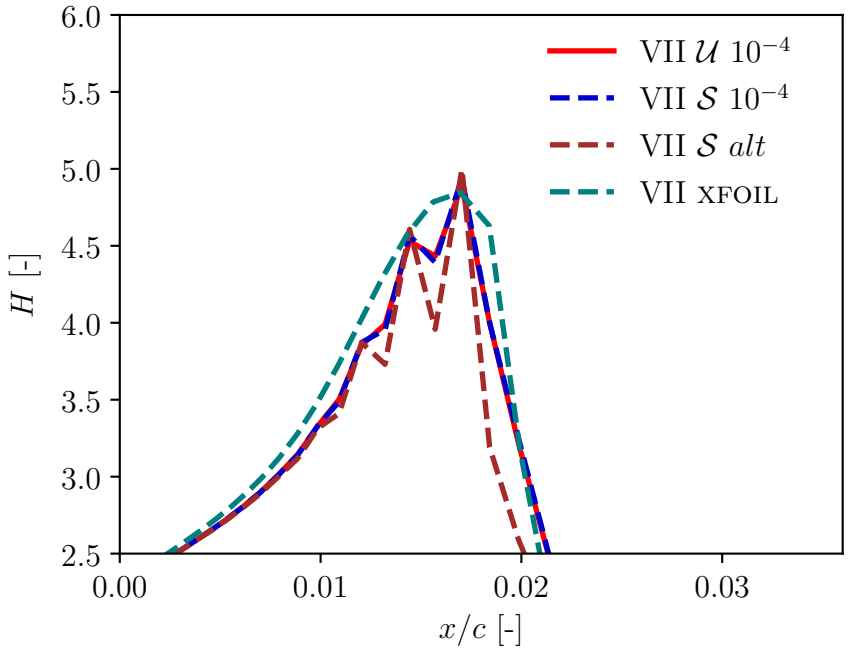


Figure 5.11: Boundary layer shape factor near separation for the $\mathcal{U}$ and $\mathcal{S}$ coupling (first and second equilibrium positions). Comparison with XFOIL results. (NACA0012 at 10° angle of attack, $\mathrm{Re} = 3 \times 10^6$).

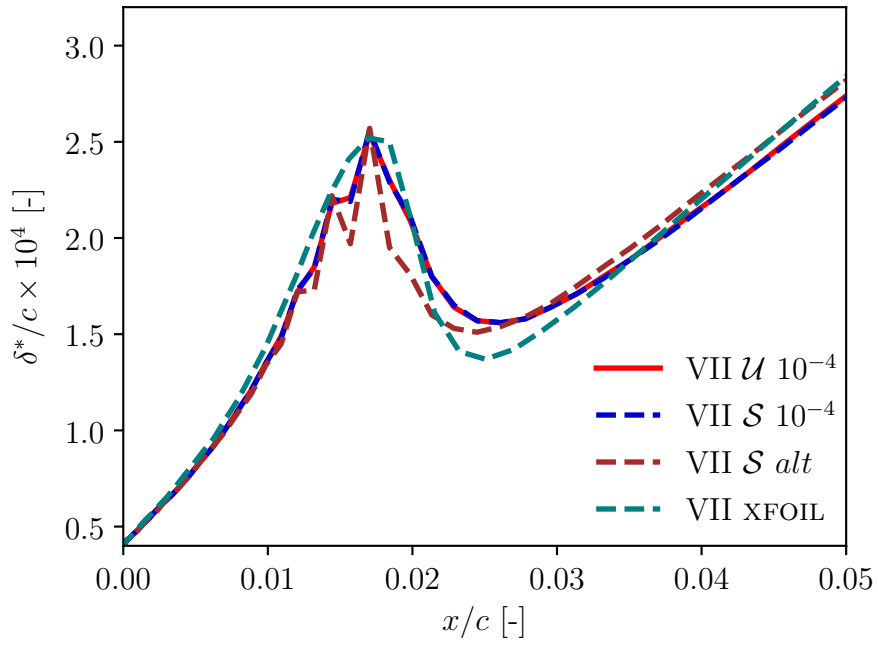


Figure 5.12: Displacement thickness near separation for the $\mathcal{U}$ and $\mathcal{S}$ coupling (first and second equilibrium positions). Comparison with XFOIL results. (NACA0012 at 10° angle of attack, $\mathrm{Re} = 3 \times 10^6$).

#### 5.2.3.2 15° angle of attack

At a higher angle of attack of 15°, the separation region gets even less stable than at 10°. The "convergence" of the drag and lift coefficients for both coupling strategies is shown in Figure 5.13.

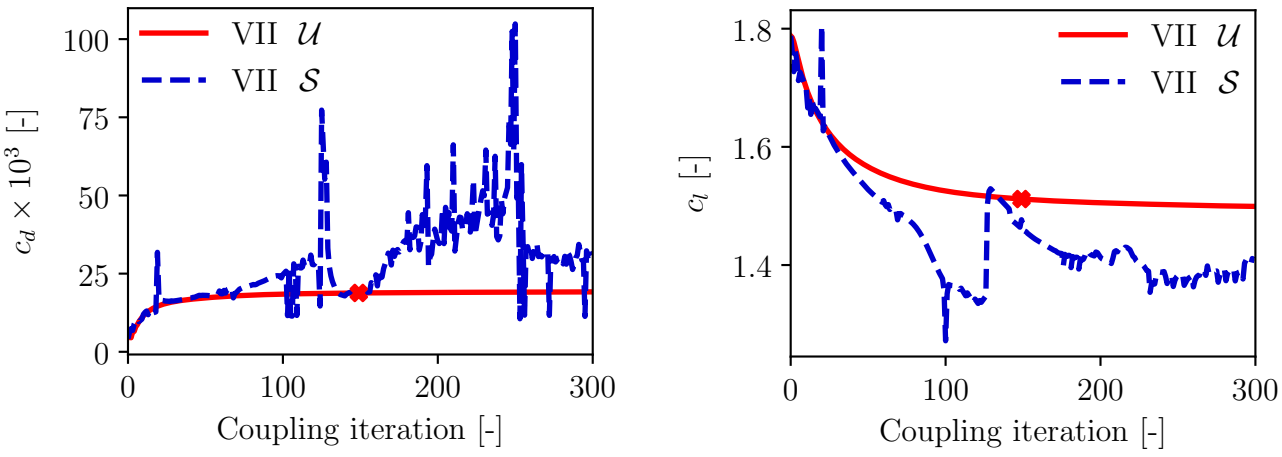


(a) Drag coefficient.

(b) Lift coefficient.

Figure 5.13: Comparison of the $\mathcal{S}$ and $\mathcal{U}$ coupling strategies for the lift and drag coefficients evolution through coupling iterations (NACA0012 at 15° angle of attack, $\mathrm{Re} = 6 \times 10^6$, tripped transition at $x/c = 0.05$). The crosses mark $10^{-4}$ error reached for the $\mathcal{U}$ method.

While the $\mathcal{U}$ coupling strategy converges smoothly and monotonically, the $\mathcal{S}$ coupling strategy shows no converging trend. The oscillations are large and the solution never stabilizes. The issue has again been observed at the separation region, where all quantities oscillate heavily. Note that this diverging behavior observed for the $\mathcal{S}$ coupling does not seem to be mesh dependent (at least for cosine meshes) and is observed for any mesh refinement. Various meshes were tested, ranging from 338 up to 646 elements on the airfoil surface; the behavior was consistent and could be solved by the $\mathcal{U}$ coupling strategy with appropriate time steps. The problem is also not caused by the exact flow conditions either, as slightly modifying the angle of attack (down to 14.5°) shows the same issue.

It might be possible that other numerical parameters could be adjusted to stabilize the $\mathcal{S}$ coupling strategy for this flow condition. For example, the initial CFL number or the tolerance of the time marching procedure could be adjusted. This was not investigated further in the present work.

The results of the $\mathcal{U}$ coupling strategy and XFOIL are summarized in Table 5.4 with the experimental data.

| | $c_l$ [-] | $c_d \times 10^3$ [-] | $x_{tr_{top}}/c$ [-] | $N_{it}$ [-] | Execution time [s] |
|---|---|---|---|---|---|
| UPM Inviscid | 1.7879 | - | - | - | - |
| VII $\mathcal{U}$ $10^{-4}$ | 1.5117 | 18.82 | 0.0088 | 149 | 7.5 |
| VII XFOIL | 1.5489 | 19.45 | 0.0106 | - | - |
| Exp Gregory & O'Reilly[2] [28] | 1.53 | 29.5 | 0.0099 | - | - |

Table 5.4: Summary of the results for the NACA0012 at 15° angle of attack, $\mathrm{Re} = 3 \times 10^6$, tripped transition at $x/c = 0.05$. Experimental data of Gregory and O'Reilly [28] at $\mathrm{Re} = 2.88 \times 10^6$, $M_\infty = 0.16$ and free transition.

While both the $\mathcal{U}$ method and XFOIL predict the lift coefficient and transition location well, they severely underpredict the drag coefficient. They agree well with each other, indicating that this is not caused by the present implementation; this can be caused by the mathematical model (closure set, assumptions, ...) or by the differences between the experimental and numerical setup.

### 5.2.4 Airfoil polar

In order to understand the differences between the $\mathcal{S}$ and $\mathcal{U}$ coupling strategies in a more general way, the lift and drag polars of the NACA2412 airfoil are considered. XFOIL is again considered as a reference with the same assumptions and a similar level of accuracy as the present methods. The experimental data of Abbott *et al.* [1] is used for comparison.

Angles ranging from −8° to 13° are considered at a Reynolds number of $3.1 \times 10^6$ and transition is free. The experimental Mach number is not given, but can be approximated based on the chord of the airfoil (24 in.) and assuming air at a standard temperature of 15°C. The Mach number is then estimated to be around 0.2.

[2]The experimental data has been digitized and may be inaccurate.

The $\mathcal{S}$ and $\mathcal{U}$ simulations are run until the errors drops under $10^{-5}$. The experimental and numerical lift and drag evolutions with angle of attack are shown respectively in figures 5.14 and 5.15.

The different codes are in good agreement with each other for the lift coefficient. At high angles of attack, they all show a slight drop in the slope of the lift curve, but not as pronounced as the experimental data. Better estimations of stall can be obtained by higher-fidelity methods such as Euler or full-potential codes, but the simple panel methods considered in this work and in XFOIL cannot accurately represent it.

For the drag coefficient, XFOIL gives different results than the present implementations. At low incidence, drag is well predicted by the $\mathcal{U}$ and $\mathcal{S}$ coupling strategies but underpredicted by XFOIL. At higher angles of attack, all VII results tend to underestimate the drag coefficient.

Overall, the $\mathcal{U}$ and $\mathcal{S}$ strategies yield nearly identical results through all considered angles of attack.

A small separation bubble is observed by the VII codes near the leading edge starting from 9° angle of attack.

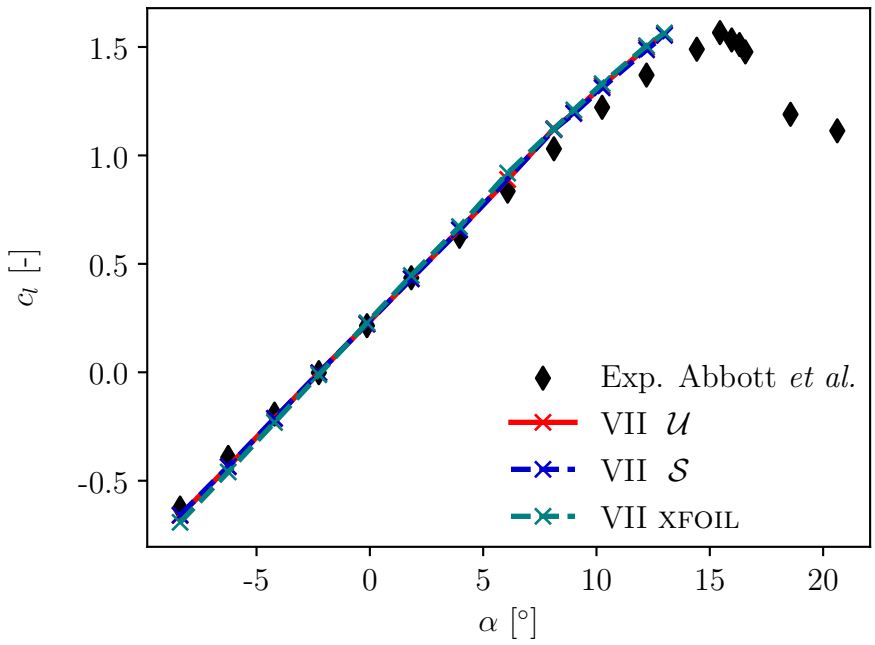


Figure 5.14: Evolution of the lift coefficient with angle of attack of the NACA2412 airfoil at $\mathrm{Re} = 3.1 \times 10^6$ with the $\mathcal{U}$ and $\mathcal{S}$ coupling. Comparison with XFOIL results and experimental data from Abbott *et al.* [1] ($M_\infty^{est} = 0.2$).

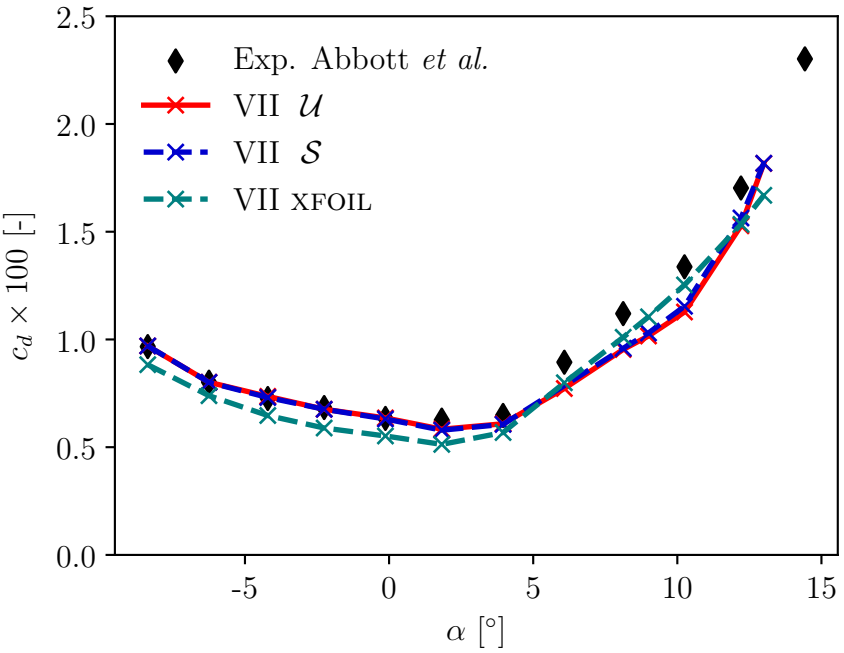


Figure 5.15: Evolution of the drag coefficient with angle of attack of the NACA2412 airfoil at $\mathrm{Re} = 3.1 \times 10^6$ with the $\mathcal{U}$ and $\mathcal{S}$ coupling. Comparison with XFOIL results and experimental data from Abbott *et al.* [1] ($M_\infty^{est} = 0.2$).

The execution times of the $\mathcal{U}$ and $\mathcal{S}$ coupling strategies for all angles of attack are shown in Figure 5.16.

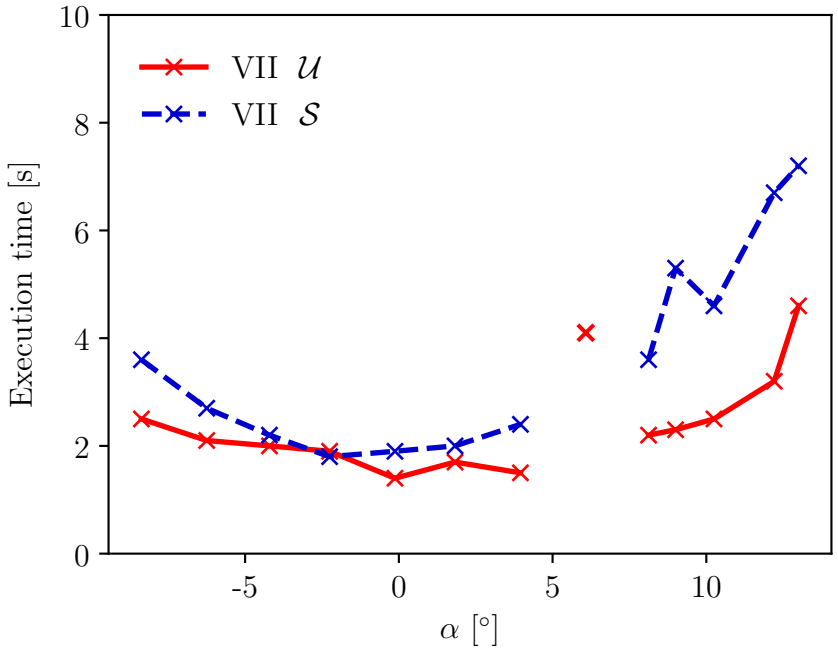


Figure 5.16: Evolution of the execution time of the $\mathcal{U}$ and $\mathcal{S}$ coupling with angle of attack of the NACA2412 airfoil at $\mathrm{Re} = 3.1 \times 10^6$.

Near zero-lift, the $\mathcal{S}$ coupling strategy is slightly faster than the $\mathcal{U}$ coupling strategy due to the relatively simple flow conditions. With increased and decreased incidence, the $\mathcal{U}$ strategy becomes faster for all cases.

At 6° angle of attack, an unphysical transition appear on the lower side near the trailing edge. This purely numerical issue causes large oscillations in the solution and prevents convergence. The $\mathcal{U}$ manages to dampen these oscillations enough to reach a converged solution. At 9° angle of attack, separation starts to develop on the upper surface. The $\mathcal{S}$ strategy shows relative difficulty to reach a solution compared to adjacent angles of attack. The $\mathcal{U}$ strategy, however, does not show any particular issue.

It is important to remember that even if the $\mathcal{U}$ coupling proves to be faster in most presented cases, it does require finding good values of the inviscid and viscous time steps for this to happen. In the future, it would be beneficial to develop a time step adaptation strategy within the solver to perform this task automatically.

### 5.2.5 Low-Reynolds flow with trailing edge separation

The prediction of low-Reynolds number flows is a difficult task for VII methods. One of the assumptions of the model is that the boundary layer is thin, which is less and less valid as the Reynolds number decreases. The quasi-simultaneous method eventually encounters a singularity and becomes unstable. Drela [21] manages to extend the range of the XFOIL solver by relying on an inverse coupling strategy when the solver fails. Within BLASTER, Dechamps [18] showed an example flow of a NACA0012 airfoil at 5° angle of attack and $\mathrm{Re} = 5 \times 10^5$, where the flow separates near the trailing edge. The solver struggled and never really reached a converged solution.

The present methods were tested on the same flow conditions to determine whether the $\mathcal{U}$ coupling can allow the solver to reach a converged solution. Many combinations of mesh density and time steps were tested, but none of them allowed the $\mathcal{U}$ method to stabilize the solution. A typical evolution of the lift and drag coefficients through coupling iterations is shown in Figure 5.17.

The issues are again visible in the separation region. Figure 5.18 shows the displacement thickness of the two coupling methods after 300 coupling iterations. They both show oscillations in the separation region, near the trailing edge. Since this issue happens at the trailing edge, it impacts the Kutta condition, which is likely to be the cause of the divergence.

The displacement thickness of the present methods significantly deviates from the XFOIL results starting at around 75% of the chord.

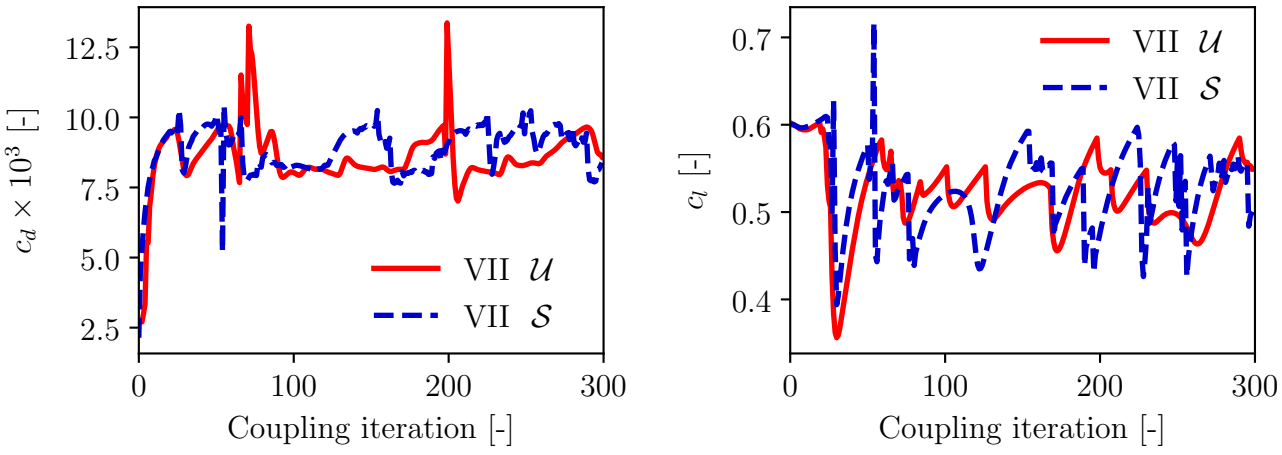


(a) Drag coefficient.

(b) Lift coefficient.

Figure 5.17: Comparison of the $\mathcal{S}$ and $\mathcal{U}$ coupling strategies for the lift and drag coefficients evolution through coupling iterations (NACA0012 at 5° angle of attack, $\mathrm{Re} = 5 \times 10^5$).

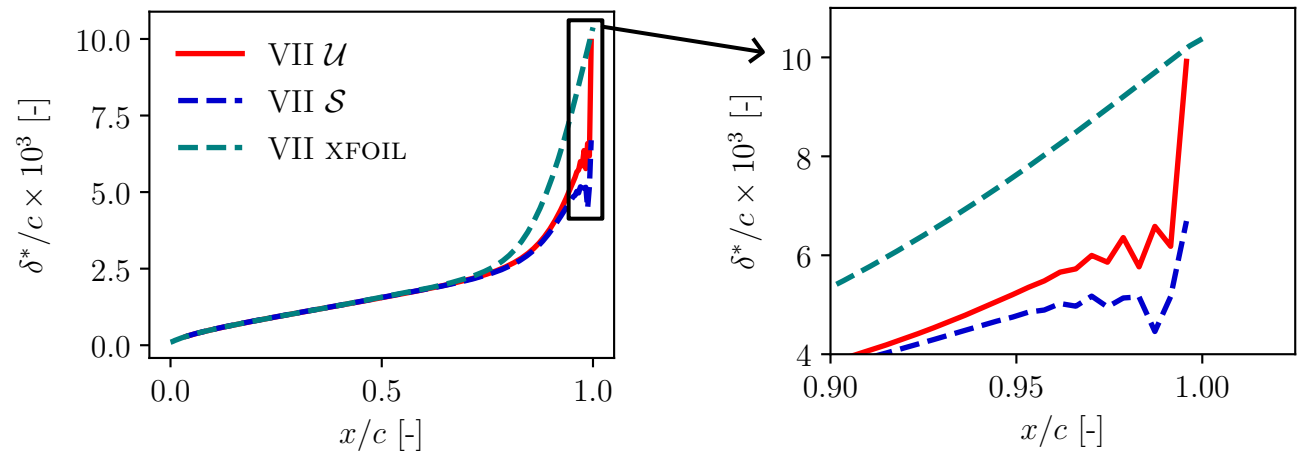


Figure 5.18: Displacement thickness along the chord of the NACA0012 airfoil at 5° angle of attack and $\mathrm{Re} = 5 \times 10^5$ after 300 coupling iterations of the $\mathcal{S}$ and $\mathcal{U}$ VII coupling. Comparison with XFOIL.

### 5.2.6 Summary

In most presented cases, the $\mathcal{U}$ coupling strategy proved to be more stable and faster than the $\mathcal{S}$ coupling strategy, given the right time step choice. The $\mathcal{S}$ coupling strategy showed more oscillatory behavior in the separation region, which could be dampened by the $\mathcal{U}$ coupling.

At low incidence, both methods showed a similar convergence; the $\mathcal{S}$ coupling, with its low iteration cost and lack of time step tuning, could be more advantageous for general study of such flows.

For the tested low-Reynolds number flow, the $\mathcal{U}$ coupling strategy was not able to stabilize the solution.

## 5.3 Inviscid unsteady flow

This section presents the results of the UPM method for unsteady inviscid flows. The sudden change in angle of attack as well as the sinusoidal pitching motion of a flat plate are considered and compared to theoretical tools. The results of the UPM method are also compared to Euler results for the pitching of an airfoil with thickness.

### 5.3.1 Starting flow

The first considered unsteady case is the one of the sudden change of angle of attack. The airfoil initially sits at zero incidence, and at $t = 0$, it is set to a non-zero angle of attack. Due to unsteady effects, the lift does not instantaneously grow to its steady value but does it progressively over time. For a flat plate in inviscid flow, Wagner's theory predicts the lift coefficient evolution as

$$c_l(t) = 2\pi\alpha\Phi(t), \tag{5.2}$$

where $\Phi(t)$ is known as Wagner's function, which can be approximated by

$$\Phi(t) = 1 - 0.165\exp\left(-0.0455\frac{V_\infty t}{b}\right) - 0.335\exp\left(-0.3\frac{V_\infty t}{b}\right), \tag{5.3}$$

with $b$ being the half-chord of the airfoil.

Using an extremely thin NACA0001 airfoil, the UPM method can essentially approximate a flat plate and be compared with Wagner's theory. The ratio between the lift coefficient at a given time and the steady lift coefficient is plotted in Figure 5.19.

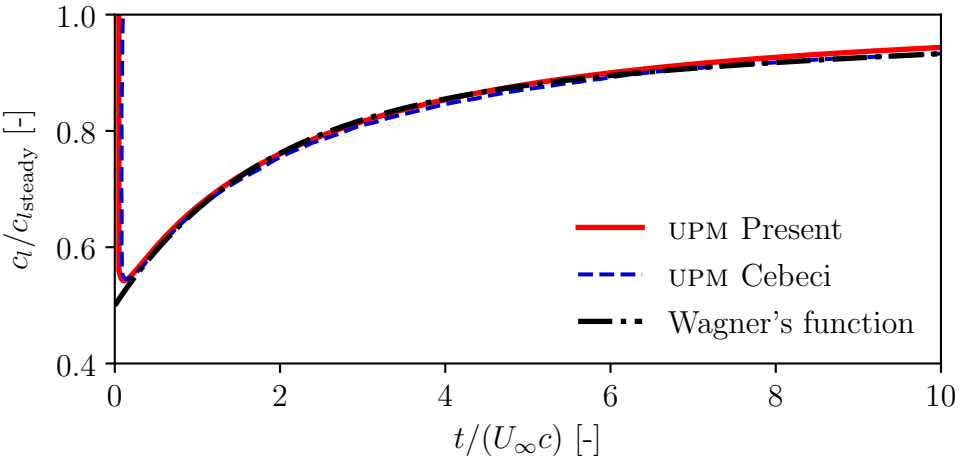


Figure 5.19: Comparison of Wagner's theory with the UPM method (present implementation and results of Cebeci [12]) for the unsteady lift coefficient of a flat plate undergoing a sudden change in incidence at $t = 0$.

The results of the panel method are in good agreement with Wagner's theory, except at the start of the simulation where the UPM method initially predicts a high lift coefficient (even higher than its steady value). This spike has also been observed by Cebeci [12] using the same method. For a short time at the beginning of the simulation, some unphysical transience is present, but it quickly dies out.

By plotting the locations of the core vortices, the UPM method also allows to visualize the shape of the wake *i.e.* the starting vortex in this case, as shown in Figure 5.20.

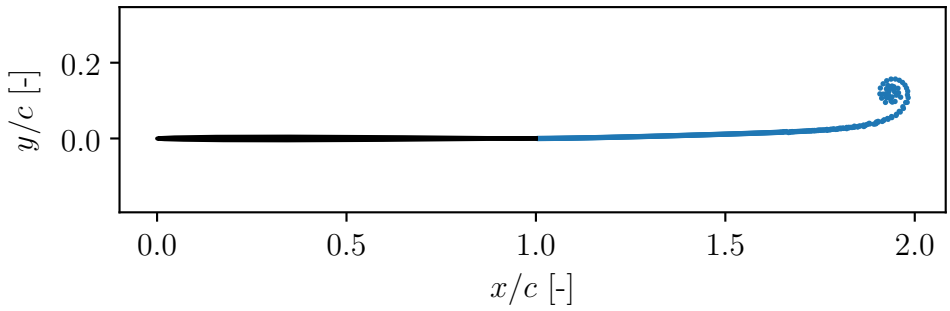


Figure 5.20: Visualization of the starting vortex calculated with the UPM method.

### 5.3.2 Pitching

The case of a sinusoidally pitching flat plate is considered for comparison with Theodorsen's theory. The pitching motion of amplitude $\alpha_a$ around a mean angle of attack $\alpha_m$ and angular frequency $\omega$ is described by the following law of motion

$$\alpha(t) = \alpha_m + \alpha_a \sin(\omega t). \tag{5.4}$$

Theodorsen's theory allows to predict the evolution of lift coefficient for this pitching motion based on its reduced frequency

$$k = \frac{\omega c}{2V_\infty}. \tag{5.5}$$

The lift coefficient is given by

$$c_l(t) = 2\pi\alpha_m + \frac{1}{V_\infty^2}\left(\pi b V_\infty j\omega\alpha_a + 2\pi C(k)\left[V_\infty\alpha_a + \left(\frac{3}{4}c - x_f\right)j\omega\alpha_a\right] + \pi b\left[x_f - \frac{c}{2}\omega^2\alpha_a\right]\right)e^{j\omega t}, \tag{5.6}$$

where $x_f$ is the pivot point of the airfoil, $b$ is the half-chord, $j$ is the imaginary unit and $C(k)$ is Theodorsen's function, which can be approximated by

$$C(k) = 1 - \frac{0.165}{1 - \frac{0.0455}{k}j} - \frac{0.335}{1 - \frac{0.3}{k}j}. \tag{5.7}$$

This theory is compared to the results of the UPM method for a NACA0001 airfoil undergoing sinusoidal pitching motion of amplitude $\alpha_a = 1°$ around its quarter chord for different reduced frequencies.

The UPM mesh for this case is a cosine mesh (see Figure 5.1) with 1000 panels. In order to choose an appropriate time step for the simulation, a convergence analysis has been performed on the highest value of the lift coefficient, and its corresponding angle of attack (for the reduced frequency $k = 0.5$). The results of this analysis are shown in Figure 5.21.

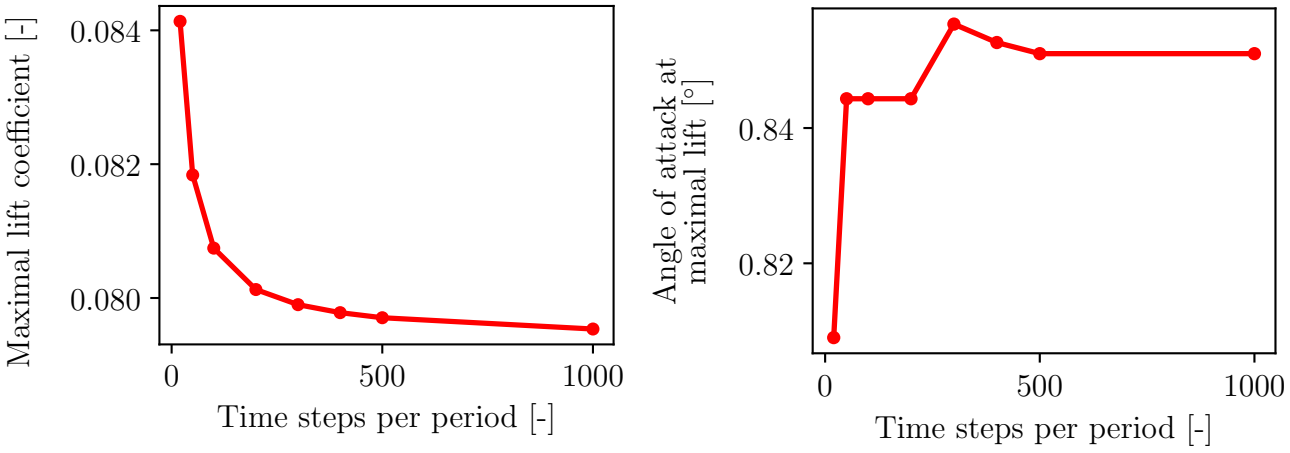


(a) Maximal value of the lift coefficient.

(b) Angle of attack at maximal lift.

Figure 5.21: Time step convergence analysis of the UPM method for inviscid pitching motion (NACA0001, $\alpha_a = 1°$, $\alpha_m = 0°$, $k = 0.5$, $x_f = c/4$, cosine mesh with 1000 panels).

Even with a low number of 100 time steps per period, the maximal lift coefficient and its corresponding angle of attack are already within 2% of the converged value. A number of time steps of 500 is chosen per period of the pitching motion for the inviscid simulations to maximize precision. Three periods are simulated to ensure that the initial transience has died out. The lift hysteresis results of the UPM method and Theodorsen's theory are shown in Figure 5.22.

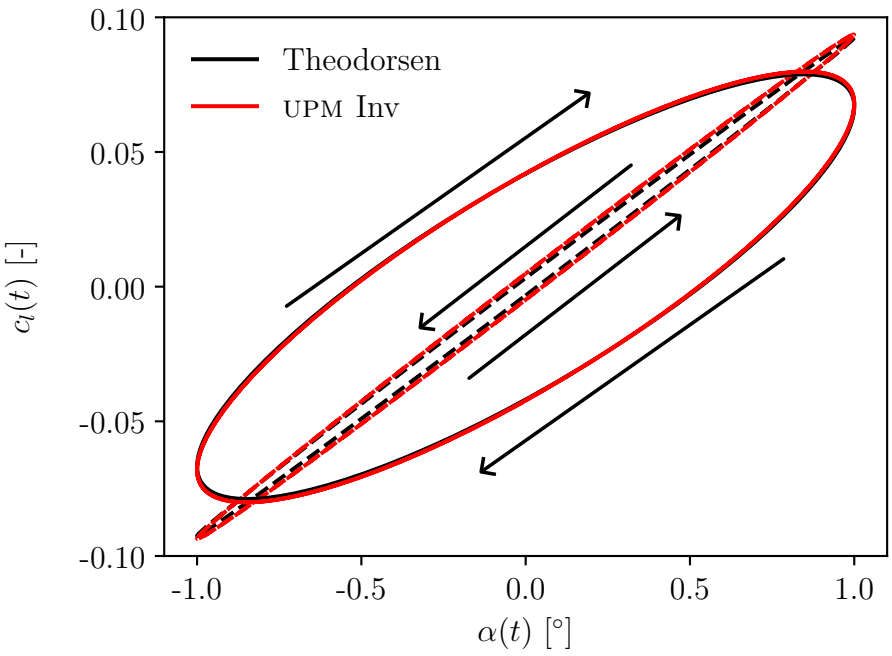


Figure 5.22: Comparison of Theodorsen's theory with UPM for the unsteady lift coefficient of a flat plate (NACA0001) undergoing an inviscid sinusoidal pitching motion ($\alpha_a = 1°$, $\alpha_m = 0°$, $x_f = c/4$, $k = 0.1$ (dashed) and $k = 0.5$ (solid)). Highlight of the direction of the lift coefficient evolution.

The results of the panel method are in good agreement with Theodorsen's theory for both considered reduced frequencies. As pointed out by Motta *et al.* [40], Theodorsen's theory predicts a phase inversion of the lift coefficient at $k = 0.144$. This inversion is also observed in the results of the panel method.

While Theodorsen's theory is a good validation tool for the panel method, it is unable to take the impact of thickness, which can be significant, into account. Therefore, the UPM method is also compared to the Euler results of Motta *et al.* [40] for the same motion, but with a thicker airfoil (NACA0024). This is shown in Figure 5.23.

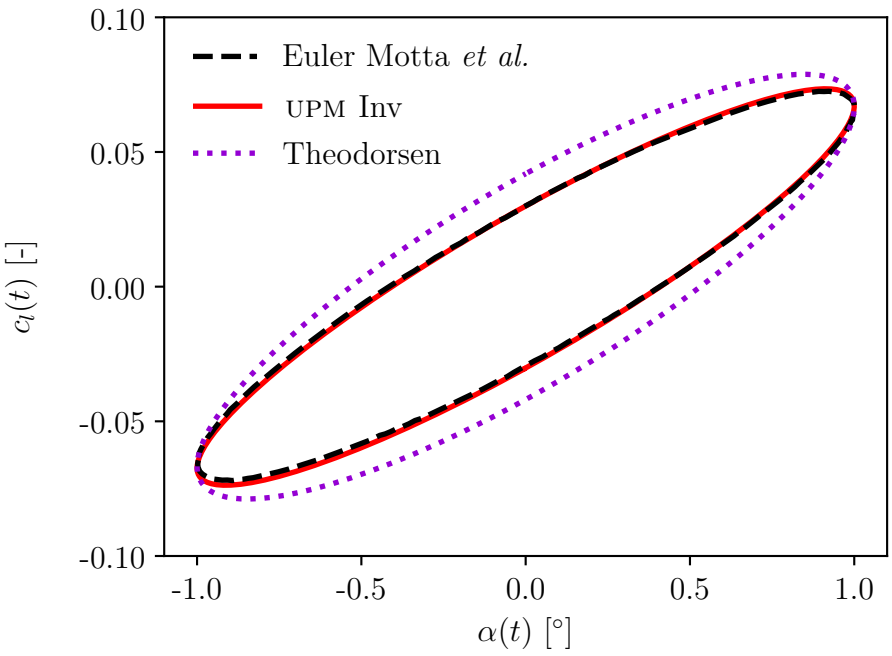


Figure 5.23: Comparison of UPM with the Euler results of Motta *et al.* [40] ($M_\infty = 0.117$) for the unsteady lift coefficient of a NACA0024 airfoil undergoing an inviscid sinusoidal pitching motion ($\alpha_a = 1°$, $x_f = c/4$, $k = 0.5$). Theodorsen's results for a flat plate for reference.

The UPM results match the Euler results well, showing that the method correctly captures the impact of thickness on the lift hysteresis.

## 5.4 Viscous unsteady flow

Knowing all the different simplifications in the present model, the space of possible viscous unsteady applications is limited.

The ideal case would be a movement with a low amplitude to avoid the displacement of the stagnation point and a low reduced frequency to avoid large unsteady effects in the closure model. Additionally, forced transition would allow avoiding effects of unsteady natural transition.

### 5.4.1 Low amplitude pitching

This case is the viscous extension of the previous inviscid pitching case. The airfoil is a NACA0012 pitching around its quarter chord with an amplitude of 1° and a reduced frequency of $k = 0.1$. The Reynolds number is set to $\mathrm{Re} = 10^6$. Transition is tripped at the leading edge. As for other viscous applications, a modified cosine mesh with fixed element size starting at 80% of the chord is used. The number of elements is set to $N = 690$.

As discussed in section 4.5, the time step should be chosen small enough to eliminate the effect of the interaction law on the viscous results. It was however found that refining the time step too much did cause odd behaviors in the lift hysteresis loop. This is shown in Figure 5.24.

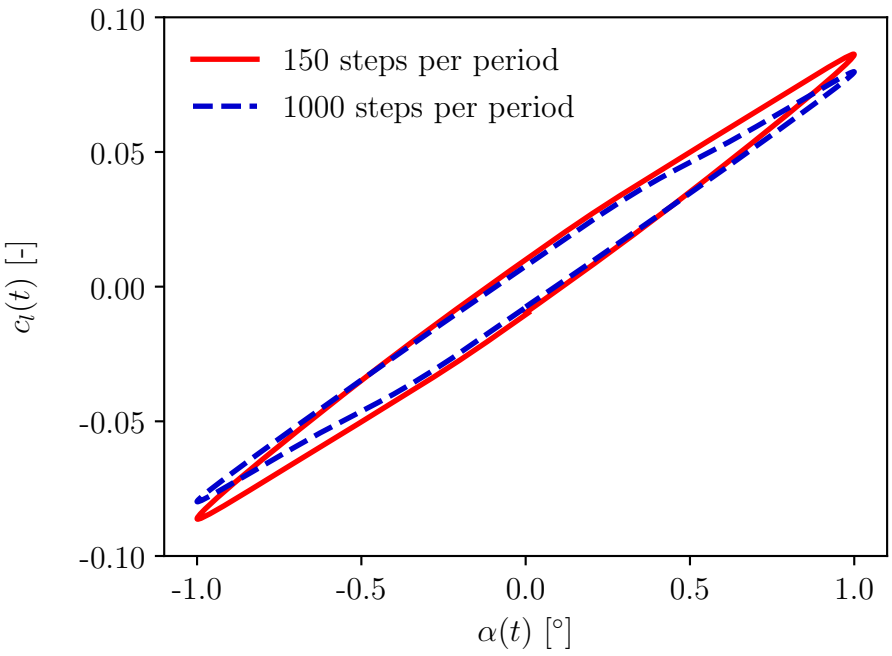


Figure 5.24: Comparison of the lift hysteresis curve for two different number of time steps per period for the viscous pitching of a NACA0012 airfoil with the present VII coupling ($\alpha_a = 1°$, $\alpha_m = 0°$, $x_f = c/4$, $k = 0.1$, $\mathrm{Re} = 10^6$).

For a high number of time steps, the model seems to lack inertia after reaching the top/bottom of the stroke as the lift coefficient drops faster than for lower time step count. The reason for this behavior is unknown and would require further investigation.

A lower number of 150 time steps per period is used for comparison with higher fidelity data, and five periods are simulated to eliminate the effect of initial conditions.

The results of the present VII method are compared to the inviscid results of the UPM method, as well as a RANS simulation performed by Motta and Quaranta [41] using the Spalart-Allmaras turbulence model (at a Mach number of 0.117). The results are shown in Figure 5.25.

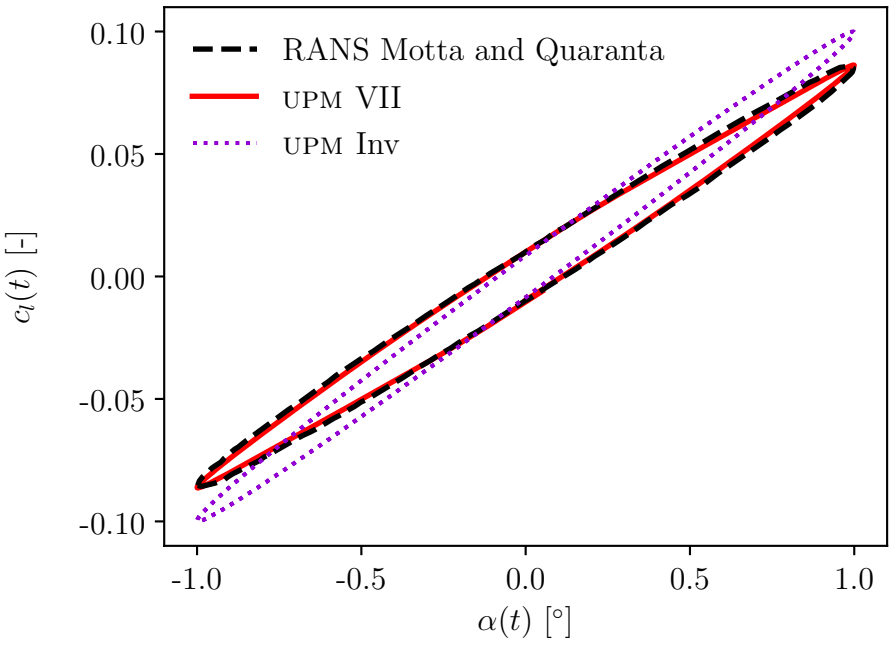


Figure 5.25: Comparison of the present VII model with the RANS results of Motta and Quaranta [41] ($M_\infty = 0.117$) for the unsteady lift coefficient of a NACA0012 airfoil undergoing a viscous sinusoidal pitching motion ($\alpha_a = 1°$, $\alpha_m = 0$, $x_f = c/4$, $k = 0.1$, Re $= 10^6$). UPM inviscid results for reference.

The present results show a good agreement with the RANS results indicating that viscous effects are well captured. The VII curve is still slightly flatter than the RANS one near the top and bottom of the movement.

The same test case was also run at a higher reduced frequency of $k = 0.4$ to study the effect of the reduced frequency on the solution. The results are shown in Figure 5.26.

The results for this higher reduced frequency show that the present model completely fails to capture the viscous effects. Instead of predicting a decrease in lift compared to the inviscid case, the lift coefficient is increased. This highlights the importance of unsteady effects in the closure set, which are not taken into account in the present model.

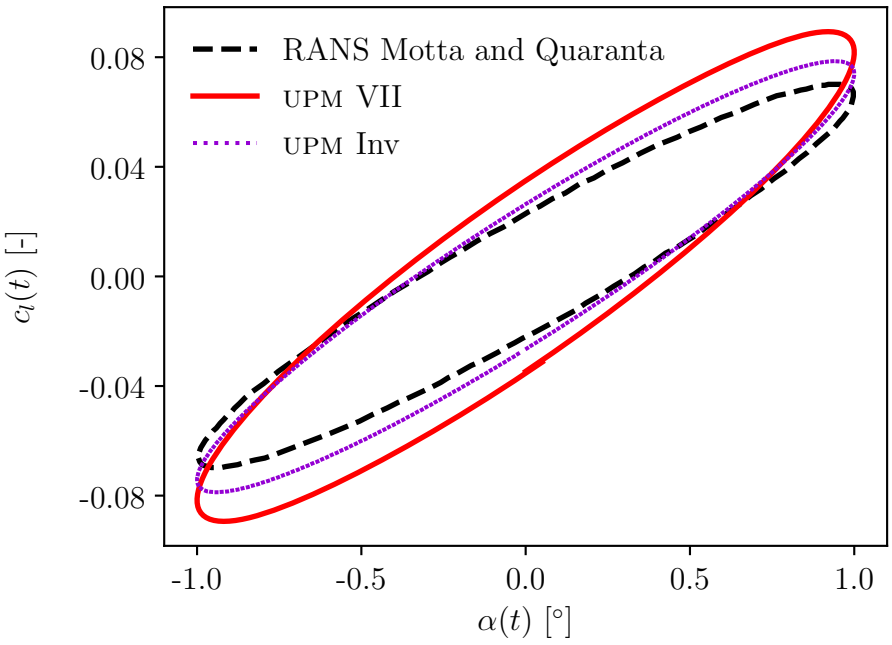


Figure 5.26: Comparison of the present VII model with RANS results of Motta and Quaranta [41] ($M_\infty = 0.117$) for the unsteady lift coefficient of a NACA0012 airfoil undergoing a viscous sinusoidal pitching motion ($\alpha_a = 1°$, $\alpha_m = 0$, $x_f = c/4$, $k = 0.4$, $\mathrm{Re} = 10^6$). UPM inviscid results for reference.

### 5.4.2 Moderate amplitude pitching

The second case is a NACA0012 airfoil pitching around a mean angle of attack $\alpha_m = 4°$ with an amplitude of $\alpha_a = 6°$ and a reduced frequency of $k = 0.021$ around the quarter chord. The Reynolds number is $1.63 \times 10^6$. The results of the present VII model are compared to VII results of Garcia [25]. A modified cosine mesh with $N = 690$ elements is used.

The transition is forced at $x/c = 0.05$, but was observed by Garcia to occur naturally earlier than this location at the top of the stroke. The $e^N$ transition model is thus activated as well, with the naive, unaveraged transition model (see section 3.2.4).

Again, using small time steps leads to a flattening of the lift hysteresis curve. A number of 75 time steps per period is chosen for this case and five periods are simulated. The results are shown in Figure 5.27.

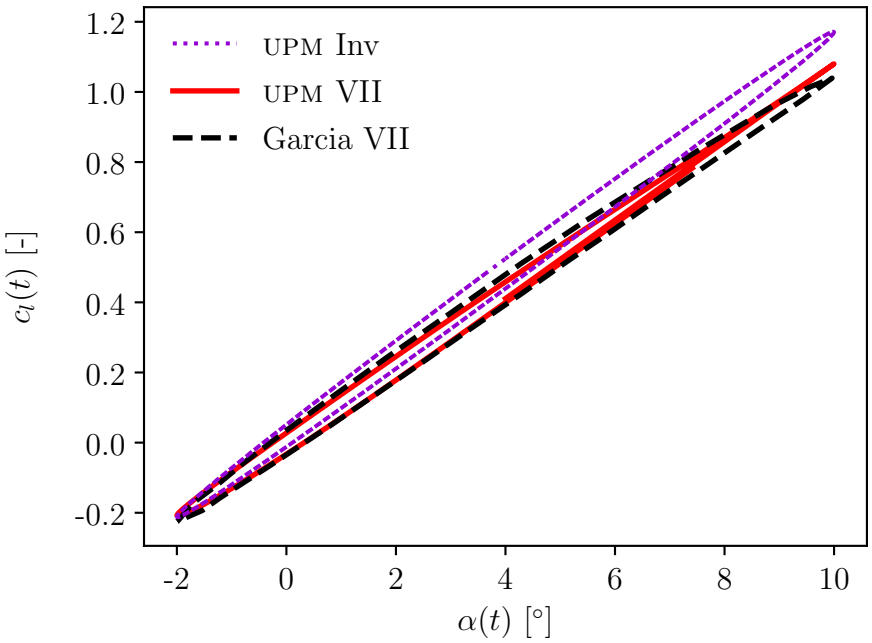


Figure 5.27: Comparison of the present VII model with VII results of Garcia [25] for the unsteady lift coefficient of a NACA0012 airfoil undergoing a viscous sinusoidal pitching motion ($\alpha_a = 6°$, $\alpha_m = 4$, $x_f = c/4$, $k = 0.021$, $\mathrm{Re} = 1.63 \times 10^6$). UPM inviscid results for reference.

For low incidences, both models show a good agreement. However, the present model gets flatter for higher angles of attack and does not properly capture the maximal lift diminution. The present model also predicts separation starting from around 7.6 degrees, whereas Garcia [25] observed a fully attached boundary layer. These differences are likely due to the same problem. The model misses unsteadiness at the top of the stroke and acts "more steady" than it should. The retardation of the separation point, which is an unsteady effect, is thus missed.

# 6 Conclusion

## 6.1 Summary and conclusion

The objective of this thesis was to implement a new unsteady coupling strategy ($\mathcal{U}$ coupling) within the BLASTER solver [18], and compare it with the existing steady coupling strategy ($\mathcal{S}$ coupling). For this purpose, the existing inviscid solver DARTFLO [16] was replaced with an incompressible panel method, in its steady (HSPM) and unsteady (UPM) forms.

The two considered strategies were tested on different steady test cases, including low incidence attached flow, mildly separated flows and low-Reynolds flow. The $\mathcal{U}$ coupling strategy was found to be more robust than the $\mathcal{S}$ method for challenging flows at high angles of attacks. At low incidence, the methods were almost equivalent in stability and execution time. Both strategies yielded extremely similar results for all tested cases. Unfortunately, the solver's divergence for the low-Reynolds flow was not resolved by the $\mathcal{U}$ coupling strategy.

The present work also included the investigation of unsteady flows simulations. The different missing elements in the model were identified and discussed. The closure model and transition handling were found to be the most critical elements to be improved. Nonetheless, the solver was able to predict the unsteady low-amplitude pitching lift coefficient of a NACA0012 airfoil with good agreement to RANS simulations. Issues were observed when refining the time step, which should be addressed in future work.

## 6.2 Suggestions for future work

Through the course of this work, several areas have been identified for further research. These include:

- **Automatic time step adaptation:** the current implementation of the $\mathcal{U}$ coupling strategy requires manual tuning of the inviscid and viscous time steps. It would greatly benefit from an automatic time step adaptation algorithm. Some criterion should be derived to increase or decrease the time step based on the convergence of the solution.
- **Extension to higher fidelity inviscid models:** the current panel method is limited to simple incompressible flows. The implementation of a higher fidelity unsteady inviscid model, coupled with the viscous model through the $\mathcal{U}$ strategy, would allow for the simulation of more complex flows. Through more complex test cases, more insight could be gained on the advantages and limitations of the $\mathcal{U}$ strategy.
- **Improvement of the viscous unsteady model:** the present implementation of the viscous unsteady model lacks several important features. The closure and transition models need unsteady corrections to be able to predict the unsteady flow accurately. The stagnation point movement should also be tackled if large amplitude motions are to be considered. The model also showed issues when refining the time step, where the lift hysteresis curve would flatten. The origin of this issue should be identified and resolved.

  Ultimately, the model could be able to predict dynamic stall, which is a challenging problem.

# References


[1] I.H. Abbott, A.E. Von Doenhoff, and Stivers L.Jr. *Summary of airfoil data*. Tech. rep. 1945.

[2] J.D. Anderson. *Fundamentals of Aerodynamics*. McGraw-Hill Education, 2010. ISBN: 978007-3398105.

[3] R.E. Bartels. *On an Asymptotically Consistent Unsteady Interacting Boundary Layer*. Tech. rep. 2007.

[4] B.C. Basu and G.J. Hancock. "The unsteady motion of a two-dimensional aerofoil in incompressible inviscid flow". In: *Journal of Fluid Mechanics* 87.1 (1978), pp. 159–178.

[5] M.B. Bieterman et al. "Boundary layer coupling in a general configuration full potential code". In: *2nd European CFD Conference, Stuttgart, Germany*. 1994.

[6] A. Bilocq. "Implementation of a viscous-inviscid interaction scheme in a finite element full potential solver". MA thesis. University of Liège, 2020.

[7] G.W. Brune, P.E. Rubbert, and T.C. Nark Jr. "New Approach to Inviscid Flow/Boundary-Layer Matching". In: *AIAA Journal* 13.7 (1975), pp. 936–938.

[8] J. Carter. "A new boundary-layer inviscid iteration technique for separated flow". In: *4th Computational Fluid Dynamics Conference*. 1979, p. 1450.

[9] D. Catherall and K.W. Mangler. "The integration of the two-dimensional laminar boundary-layer equations past the point of vanishing skin friction". In: *Journal of Fluid Mechanics* 26.1 (1966), pp. 163–182.

[10] T. Cebeci and P. Bradshaw. *Momentum transfer in boundary layers*. Hemisphere Publishing Corporation, 1977. ISBN: 9780070103009.

[11] T. Cebeci and H.M. Jang. "Interactive boundary-layer method for unsteady airfoil flows-quasisteady model". In: *Journal of aircraft* 27.8 (1990), pp. 673–678.

[12] T. Cebeci et al. *Analysis of low-speed unsteady airfoil flows*. Springer Berlin Heidelberg, 2005. ISBN: 978-3-540-22932-2.

[13] T. Cebeci et al. "Prediction of post-stall flows on airfoils". In: *Numerical and Physical Aspects of Aerodynamic Flows IV*. Springer, 1990, pp. 97–109.

[14] E.G.M. Coenen. "Computational techniques for viscous-inviscid boundary layer interaction". MA thesis. University of Groningen, 1996.

[15] J. Cousteix and T. Cebeci. *Modeling and computation of boundary-layer flows*. 2nd ed. Springer Berlin Heidelberg, 2005. ISBN: 3-540-65010-5.

[16] A. Crovato et al. "A discrete adjoint full potential formulation for fast aerostructural optimization in preliminary aircraft design". In: *Aerospace Science and Technology* 138 (2023), p. 108332.

[17] J.L.R. d'Alembert. *Essai d'une nouvelle théorie de la résistance des fluides*. David l'aîné, 1752.

[18] P. Dechamps. "Improvement of the viscous-inviscid interaction method implemented in DARTFlo". MA thesis. University of Liège, 2022.

[19] M. Drela. "Three-dimensional integral boundary layer formulation for general configurations". In: *21st AIAA computational fluid dynamics conference*. 2013, p. 2437.

[20] M. Drela. "Two-dimensional transonic aerodynamic design and analysis using the Euler equations". PhD thesis. Massachusetts Institute of Technology, 1986.

[21] M. Drela. "XFOIL: An analysis and design system for low Reynolds number airfoils". In: *Low Reynolds Number Aerodynamics: Proceedings of the Conference Notre Dame, Indiana, USA, 5–7 June 1989*. Springer. 1989, pp. 1–12.

[22] M. Drela and M.B. Giles. "Viscous-inviscid analysis of transonic and low Reynolds number airfoils". In: *AIAA journal* 25.10 (1987), pp. 1347–1355.

[23] B.I. Epureanu, K.C. Hall, and E.H. Dowell. "Reduced-order models of unsteady viscous flows in turbomachinery using viscous–inviscid coupling". In: *Journal of Fluids and Structures* 15.2 (2001), pp. 255–273.

[24] V.M. Falkner and S.W. Skan. "Solutions of the boundary-layer equations". In: *The London, Edinburgh, and Dublin Philosophical Magazine and Journal of Science* 12.80 (1931), pp. 865–896.

[25] N.R. Garcia. "Unsteady viscous-inviscid interaction technique for wind turbine airfoils". PhD thesis. Technical University of Denmark, 2011.

[26] S. Goldstein. "On laminar boundary-layer flow near a position of separation". In: *The Quarterly Journal of Mechanics and Applied Mathematics* 1.1 (1948), pp. 43–69.

[27] J.E. Green, D.J. Weeks, and J.W.F. Brooman. *Prediction of turbulent boundary layers and wakes in compressible flow by a lag-entrainment method*. 1973.

[28] N. Gregory and C.L. O'reilly. *Low-speed aerodynamic characteristics of NACA 0012 aerofoil section, including the effects of upper-surface roughness simulating hoar frost*. Tech. rep. 1970.

[29] F. Haciahmetoglu. "Investigation of unsteady viscous-inviscid interaction schemes". MA thesis. Delft University of Technology and Energy Research Centre of the Netherlands, 2013.

[30] J.L. Hess and A.M.O. Smith. "Calculation of potential flow about arbitrary bodies". In: *Progress in Aerospace Sciences* 8 (1967), pp. 1–138.

[31] F.T. Johnson et al. *TranAir: A full-potential, solution-adaptive, rectangular grid code for predicting subsonic, transonic, and supersonic flows about arbitrary configurations. User's manual*. Tech. rep. 1992.

[32] J. Katz and A. Plotkin. *Low-speed aerodynamics*. 2nd ed. Vol. 13. Cambridge university press, 2001. ISBN: 0521665523.

[33] A. Krumbein, C. Seyfert, and N. Krimmelbein. "Automatic transition prediction in unsteady airfoil flows using an unstructured CFD code". In: *29th AIAA Applied Aerodynamics Conference*. 2011, p. 3365.

[34] W. Kutta. "Lift forces in flowing fluids". In: *Illustrated Aeronaut. Commun* 3 (1902), pp. 133–135.

[35] O.K. Kwon and R.H. Pletcher. "Prediction of incompressible separated boundary layers including viscous-inviscid interaction". In: *Journal of Fluids Engineering* 101.4 (Dec. 1979), pp. 466–472.

[36] J.C. Le Balleur. "Viscous-inviscid interaction solvers and computation of highly separated flows". In: *Studies of Vortex Dominated Flows: Proceedings of the Symposium on Vortex Dominated Flows Held July 9–11, 1985, at NASA Langley Research Center, Hampton, Virginia*. Springer. 1987, pp. 159–192.

[37] M.J. Lighthill. "On displacement thickness". In: *Journal of Fluid Mechanics* 4.4 (1958), pp. 383–392.

[38] A.F. Messiter. "Boundary-layer flow near the trailing edge of a flat plate". In: *SIAM Journal on Applied Mathematics* 18.1 (1970), pp. 241–257.

[39] D. Moro et al. "Advances in the development of a high order, viscous-inviscid interaction solver". In: *21st AIAA Computational Fluid Dynamics Conference*. 2013, p. 2943.

[40] V. Motta, A. Guardone, and G. Quaranta. "Influence of airfoil thickness on unsteady aerodynamic loads on pitching airfoils". In: *Journal of Fluid Mechanics* 774 (2015), pp. 460–487.

[41] V. Motta and G. Quaranta. "Linear reduced-order model for unsteady aerodynamics of an L-shaped Gurney flap". In: *Journal of Aircraft* 52.6 (2015), pp. 1887–1904.

[42] B.A. Nishida. "Fully simultaneous coupling of the full potential equation and the integral boundary layer equations in three dimensions". PhD thesis. Massachusetts Institute of Technology, 1996.

[43] H. Ozdemir et al. "Unsteady interacting boundary layer method". In: *35th Wind Energy Symposium*. 2017, p. 2003.

[44] L. Prandtl. "Über Flüssigkeitsbewegung bei sehr kleiner Reibung". In: *Verhandl. 3rd Int. Math. Kongr. Heidelberg (1904), Leipzig* (1905).

[45] M. Qi, W. Zhu, and S. Li. "Calculation and Selection of Airfoil for Flapping-Wing Aircraft Based on Integral Boundary Layer Equations". In: *Aerospace* 11.1 (2023), p. 46.

[46] N. Ramos-García, J.N. Sørensen, and W.Z. Shen. "Three-dimensional viscous-inviscid coupling method for wind turbine computations". In: *Wind Energy* 19.1 (2016), pp. 67–93.

[47] V. A Riziotis and S.G. Voutsinas. "Dynamic stall modelling on airfoils based on strong viscous-inviscid interaction coupling". In: *International journal for numerical methods in fluids* 56.2 (2008), pp. 185–208.

[48] H. Schlichting and K. Gersten. *Boundary-layer theory*. Springer, 2016.

[49] A.M.O. Smith. "Transition, pressure gradient and stability theory". In: *Douglas Aircraft Co., Report ES 26388* (1956).

[50] H.B. Squire and A.D. Young. *The calculation of the profile drag of aerofoils*. Tech. rep. HM Stationery Office, 1937.

[51] K. Stewartson and P.G. Williams. "Self-induced separation". In: *Proceedings of the Royal Society of London. A. Mathematical and Physical Sciences* 312.1509 (1969), pp. 181–206.

[52] N.H. Teng. "The development of a computer code (U2DIIF) for the numerical solution of unsteady, inviscid and incompressible flow over an airfoil". PhD thesis. Naval Postgraduate School Monterey, CA, 1987.

[53] J. Thomas. "Integral boundary-layer models for turbulent separated flows". In: *17th Fluid Dynamics, Plasma Dynamics, and Lasers Conference*. 1984, p. 1615.

[54] R. Vaithiyanathasamy et al. "A double wake model for interacting boundary layer methods". In: *2018 Wind Energy Symposium*. 2018, p. 0516.

[55] B. Van Es. "Comparison and Application of Unsteady Integral Boundary Layer Methods using various numerical schemes". MA thesis. Delft University of Technology, 2009.

[56] J.L. Van Ingen. "A suggested semi-empirical method for the calculation of the boundary layer transition region". In: *University of Techn., Dept. of Aerospace Eng., Report UTH-74* (1956).

[57] A.E.P. Veldman. "A simple interaction law for viscous–inviscid interaction". In: *Journal of Engineering Mathematics* 65.4 (2009), pp. 367–383.

[58] A.E.P. Veldman. "New, quasi-simultaneous method to calculate interacting boundary layers". In: *AIAA journal* 19.1 (1981), pp. 79–85.

[59] A.E.P. Veldman. "Quasi-simultaneous viscous-inviscid interaction for transonic airfoil flow". In: *4th AIAA Theoretical Fluid Mechanics Meeting*. 2005, p. 4801.

[60] T. Von Kármán. "Über laminare und turbulente Reibung". In: *ZAMM-Journal of Applied Mathematics and Mechanics/Zeitschrift für Angewandte Mathematik und Mechanik* 1.4 (1921), pp. 233–252.

[61] D.L. Whitfield. *Integral solution of compressible turbulent boundary layers using improved velocity profiles*. Vol. 78. 42. Arnold Engineering Development Center, Propulsion Wind Tunnel Facility, Air Force Systems Command, 1978.

[62] D.L. Whitfield, T.W. Swafford, and J.L. Jacocks. "Calculation of turbulent boundary layers with separation and viscous-inviscid interaction". In: *AIAA Journal* 19.10 (1981), pp. 1315–1322.

[63] D.L. Whitfield et al. "Computation of transonic viscous-inviscid interacting flow". In: *Numerical and physical aspects of aerodynamic flows II*. Springer. 1984, pp. 285–295.

[64] B.R. Williams. "Viscous-inviscid interaction schemes for external aerodynamics". In: *Sadhana* 16.2 (1991), pp. 101–140.

[65] J. Windte et al. "RANS simulation of the transitional flow around airfoils at low Reynolds Numbers for steady and unsteady onset conditions". In: *Tech. Univ. Braunschweig report* (2004).

[66] *XFOIL's source code*. https://web.mit.edu/drela/Public/web/xfoil/. Accessed: 2024-05-22.

[67] B. Ye. "The Modeling of Laminar-to-turbulent Transition for Unsteady Integral Boundary Layer Equations with High-order Discontinuous Galerkin Method". MA thesis. Delft University of technology, 2015.

[68] J. Young. “Numerical simulation of the unsteady aerodynamics of flapping airfoils”. PhD thesis. UNSW Sydney, 2005.